POLITECNICO DI TORINO

ENERGY DEPARTMENT

MASTER'S DEGREE IN ENERGY AND NUCLEAR ENGINEERING

Master's Degree Thesis

Two-Dimensional Modelling and Performance Analysis of an Induction-Heated Packed-Bed Thermal Energy Storage System



Supervisor

Prof. Matteo Fasano

Co-supervisor
Rubén Abbas Cámara

Candidate

Lorenzo de Nitto

September 2026

Abstract

The increasing penetration of renewable electricity and the need to decarbonize industrial process heat are driving the development of flexible power-to-heat solutions coupled with thermal energy storage. In this context, Induction-Heated Packed-Bed Thermal Energy Storage (IH-PBTES) represents an innovative concept in which electrically conductive and ferromagnetic particles are directly heated by electromagnetic induction, combining power-to-heat conversion and sensible heat storage within the same system. This work develops a two-dimensional numerical model of a magnetite-based IH-PBTES, extending a previous lumped model based on a uniform magnetic field and a single packed-bed temperature. The storage domain is represented through an axisymmetric r–z formulation, allowing the spatial distribution of the magnetic field and the local heat generation due to magnetic hysteresis and eddy currents to be considered. The thermal model describes the transient temperature field within the packed bed, including heat conduction, temperature-dependent thermophysical and electromagnetic properties, and thermal losses to the surroundings. The thermal implementation was first validated against the reference lumped model under equivalent uniform-source conditions, showing a difference below 1 °C in the mean packed-bed temperature after three hours of charging. The model was then used to analyse separately hysteresis-dominated and eddy-current-dominated operating regimes in order to isolate the individual effects of the two heating mechanisms. These cases are not intended to represent alternative operating strategies, since hysteresis and eddy-current losses would occur simultaneously in a real induction-heated packed bed. Hysteresis heating showed a self-regulating behaviour, with induced power decreasing as temperature increased, whereas eddy-current heating exhibited the opposite trend, leading to stronger temperature non-uniformities and a greater tendency to develop hot spots. The influence of packed-bed aspect ratio was also investigated while maintaining the same volume-averaged magnetic field. The numerical framework was subsequently extended to the discharging phase by modelling air flow through the packed bed using a two-temperature approach and a cell-by-cell NTU formulation. The results highlighted a trade-off between outlet-air temperature and recovered thermal power as the air mass-flow rate changes. Finally, repeated charge-discharge cycles were simulated to investigate the evolution of the thermal state and system performance under cyclic operation. Overall, the developed framework provides a useful tool for analysing the charging, discharging and cyclic behaviour of IH-PBTES systems and for supporting their future design for industrial process-heat applications.

Table of Contents

1. Introduction *1*

1.1 Thermal energy storage **1**

1.2 Induction-heated packed-bed thermal energy storage **7**

1.3 Scope and objectives of the thesis **15**

2. Methodology *18*

2.1 Reference IH-PBTES Model **18**

2.2 Charging Model **27**

2.3 Two-Dimensional Magnetic Field **32**

2.4 Temperature-Dependent Material Properties **36**

2.5 Two-Dimensional Transient Heat-Conduction Model **41**

2.6 Heat Losses and Boundary Conditions **46**

2.7 Discharging Model **52**

2.8 Charge-Discharge Cycle Modelling **59**

3. Results *67*

3.1 Model Validation **67**

3.2 Hysteresis and Eddy-Current Heating Analysis **69**

3.3 Effect of Packed-Bed Aspect Ratio **76**

3.4 Discharging Analysis **81**

3.5 Charge-Discharge Cycles **87**

4. Discussion *98*

4.1 Comparison of Charging Mechanisms **98**

4.2 Implications for IH-PBTES Design and Operation **99**

4.3 Model Limitations and Future Developments **103**

5. Conclusions *111*

6. Appendix A – Software Implementation and Code Structure *114*

A.1 Software Environment and Computational Workflow 114

A.2 Code Organization and Main Modules 115

A.3 Selected Key Code Implementations 118

A.3.1 Two-dimensional magnetic-field evaluation 119

A.3.2 Local temperature-dependent induction sources 120

A.3.3 Two-dimensional transient charging solver 123

A.3.4 Cell-by-cell discharge implementation 125

A.3.5 Propagation of the thermal state between cycles 126

A.4 Complete Code Repository 127

References ***..... 129***

List of Figures

Figure 1.1– Conceptual arrangement and heat balance of an inductively heated pebble-bed system. Adapted from [32]..... 8

Figure 2.1-Schematic representation of the induction-heated packed-bed thermal energy storage system. Reproduced from [52]..... 19

Figure 2.2-Cross-sectional view of the reference IH-PBTES configuration and definition of the main geometrical parameters. Reproduced from [52] 20

Figure 2.3– Workflow of the charging model adopted in the present work. 27

Figure 2.4– Axisymmetric geometrical representation of the packed-bed domain and discretised induction coil used in the two-dimensional magnetic-field model. 33

Figure 2.5-Temperature-dependent thermophysical and electromagnetic properties of magnetite implemented in the numerical model: (a) specific heat capacity, (b) thermal conductivity, (c) electrical conductivity, and (d) effective relative magnetic permeability. Thermophysical data are based on [31], [53], electrical conductivity on [50], and magnetic scaling on [46]..... 36

Figure 2.6– Schematic representation of the discharge configuration and half-bed computational domain adopted in the numerical model. Air enters from both physical ends of the full packed bed and flows towards a common outlet at the central plane; only one half of the system is simulated by symmetry..... 53

Figure 2.7– Schematic representation of the cyclic charging–discharging framework adopted for the IH-PBTES system, showing the transfer of the final charging temperature map to the discharge model and the propagation of the residual temperature distribution to the subsequent cycle. 60

Figure 3.1– Comparison between the temperature results obtained with the reference lumped model and the two-dimensional thermal model under equivalent uniform-source validation conditions. 67

Figure 3.2– Temporal evolution of (a) mean and maximum packed-bed temperature, (b) mean and maximum induced volumetric heat-generation rate, and (c) total induced power during the hysteresis-only charging simulation at 80 Hz and approximately 2203 A..... 70

Figure 3.3– Final two-dimensional distributions of (a) packed-bed temperature and (b) hysteresis heat-generation rate after three hours of hysteresis-only charging. 71

Figure 3.4– Temporal evolution of (a) mean and maximum packed-bed temperature, (b) mean and maximum induced volumetric heat-generation rate, and (c) total induced power during the eddy-current-only charging simulation at 50 kHz and 100 A. 72

Figure 3.5– Final two-dimensional distributions of (a) packed-bed temperature and (b) eddy-current heat-generation rate after three hours of eddy-current-only charging. 73

Figure 3.6 – Comparison between the hysteresis-only and eddy-current-only charging simulations in terms of (a) total induced power and (b) maximum induced volumetric heat-generation rate. 74

Figure 3.7– Evolution of (a) induction efficiency ηind, (b) thermal charging efficiency ηth and (c) overall charging efficiency ηch for the hysteresis-only and eddy-current-only operating conditions. 75

Figure 3.8– Effect of packed-bed aspect ratio on (a) the corrected coil current required to maintain the prescribed average magnetic-field intensity and (b) the final volume-averaged induction heat-generation rate for the isolated hysteresis and eddy-current cases. 76

Figure 3.9– Effect of packed-bed aspect ratio on (a) final mean temperature, (b) temperature non-uniformity, (c) final maximum temperature and (d) overall charging efficiency for the isolated hysteresis and eddy-current charging simulations. 77

Figure 3.10– Final two-dimensional temperature distributions obtained for the investigated packed-bed aspect ratios. The upper row refers to the hysteresis-only simulations, while the lower row corresponds to the eddy-current-only cases. The geometrical proportions of the packed beds are preserved. 79

Figure 3.11– Final two-dimensional induction heat-generation distributions obtained for the investigated packed-bed aspect ratios. The upper row refers to the hysteresis contribution, while the lower row corresponds to the eddy-current contribution. 80

Figure 3.12– Outlet-air temperature evolution for different total air mass-flow rates using (a) the hysteresis-only and (b) the eddy-current-only final charging distributions as initial thermal states. 82

Figure 3.13– Recovered thermal-power evolution for different total air mass-flow rates using (a) the hysteresis-only and (b) the eddy-current-only final charging distributions as initial thermal states. 84

Figure 3.14– Trade-off between outlet-air temperature after 60 min of discharge and mean recovered thermal power during the first hour for the investigated total mass-flow rates. The 300 °C reference level identifies the operating conditions that maintain high-temperature thermal delivery after one hour. 86

Figure 3.15– Electrical-energy balance over three consecutive hysteresis-only cycles performed with a target electrical input of 300 kWh per charging phase. Useful recovered energy, coil electrical losses and unrecovered thermal energy are reported for each cycle. 89

Figure 3.16– Electrical-energy balance over three consecutive eddy-current-only cycles under the same-energy-input charging strategy. Cycles 2 and 3 are terminated by the 650 °C maximum-temperature safety limit before the nominal 300 kWh charging target is reached. 90

Figure 3.17– Evolution of the principal cyclic performance indicators under the same mean packed-bed temperature target: (a) electrical charging energy, (b) maximum packed-bed temperature at the end of charging, (c) useful recovered energy and (d) round-trip efficiency.... 91

Figure 3.18– Electrical-energy balance over three consecutive hysteresis-only cycles performed using a mean packed-bed charging-temperature target of 400 °C. 92

Figure 3.19 – Electrical-energy balance over three consecutive eddy-current-only cycles under the 400 °C mean-temperature charging strategy. Cycles 2 and 3 are terminated by the 650 °C local maximum-temperature limit before reaching the prescribed mean-temperature target.. 93

Figure 3.20– Final two-dimensional packed-bed temperature distributions at the end of charging over three consecutive cycles using the same mean-temperature strategy: (a–c) hysteresis-only Cycles 1–3 and (d–f) eddy-current-only Cycles 1–3. 94

Figure 3.21– Residual two-dimensional temperature distributions at the end of useful discharge over three consecutive cycles: (a–c) hysteresis-only Cycles 1–3 and (d–f) eddy-current-only Cycles 1–3. The maps represent the simulated discharge half-domain, extending along the axial coordinate $z$from the physical air inlet at $z = 0$to the central outlet plane at $z = HPB/2$. 95

Figure 3.22– Outlet-air temperature evolution during the discharge phase of three consecutive cycles for (a) the hysteresis-only and (b) the eddy-current-only cases under the same mean-temperature charging strategy. The dashed line represents the 300 °C useful-discharge threshold..... 96

List of Tables

Table 2.1-Main parameters of the reference IH-PBTES configuration adopted in [52]. .. 21

Table 2.2– Temperature-dependent magnetite properties implemented in the numerical model and corresponding literature sources..... 40

Table 2.3– Schematic representation of the thermal-loss model through the lateral surface of an axial-flow packed-bed thermal energy storage system. Adapted from [54]. 47

Table 2.4 Main operating conditions and stopping criteria adopted in the charge–discharge cycle simulations. 65

Table 3.1– Main operating conditions and final temperature comparison used for validation of the two-dimensional thermal model. 68

Table 3.2 – Operating conditions adopted to isolate the hysteresis and eddy-current contributions during the charging analysis. 69

Table 3.3– Initial thermal conditions and operating parameters adopted for the preliminary discharge mass-flow-rate analysis. 82

Table 3.4– Selected quantitative results from the preliminary discharge mass-flow-rate sweep, including outlet-air temperature, mean recovered thermal power and cumulative recovered energy over the two-hour simulation period. 84

Table 3.5– Main operating conditions adopted for the repeated charge–discharge cycle simulations. 87

Table 3.6– Main charging and energy-recovery results for the three consecutive cycles performed using the same electrical-energy-input strategy. 88

Table 3.7– Main charging and energy-recovery results for the three consecutive cycles performed using a 400 °C mean packed-bed temperature target. 92

1. Introduction

1.1 Thermal energy storage

The decarbonisation of industrial activities represents one of the major challenges of the ongoing energy transition [1]. Industrial processes require substantial amounts of energy in the form of heat, supplied over a wide range of temperature levels depending on the specific application. At present, a large share of this demand is still met through the direct combustion of fossil fuels in boilers, furnaces and other conventional heating equipment [2]. The progressive reduction of the carbon intensity of electricity generation, together with the increasing penetration of renewable energy sources, has therefore made the electrification of industrial heat an increasingly relevant pathway for reducing greenhouse-gas emissions. Technologies such as heat pumps, electric boilers and direct electrical heating can replace fossil-fuel-based heat production in several industrial applications [3]. Madeddu et al. showed that a substantial fraction of European industrial energy demand could technically be electrified using technologies already available today, with the potential increasing further when emerging electrical heating technologies are considered [4].

The increasing electrification of heat is, however, closely related to another fundamental challenge of low-carbon energy systems: the variability of renewable electricity generation [5]. Solar photovoltaic and wind power production are inherently dependent on weather conditions and do not necessarily coincide with the temporal profile of industrial thermal demand. Many industrial processes, on the contrary, require continuous or highly predictable heat supply. A temporal mismatch can therefore arise between the availability of low-carbon electricity and the demand for useful thermal energy. Energy storage provides a means of decoupling energy production from energy use, allowing energy to be accumulated when it is available or economically convenient and released at a later time when required [6]. In applications in which the final energy demand is thermal, the direct storage of heat represents a particularly attractive option, since the energy can be stored in the same form in which it will ultimately be used.

Thermal Energy Storage (TES) comprises the set of technologies that enable thermal energy to be accumulated and subsequently released by modifying the thermal or physicochemical state of a storage medium. TES can improve the flexibility and dispatchability of energy systems, facilitate the integration of intermittent renewable sources and enable energy production and consumption to be shifted in time [7]. Depending on the physical mechanism through which the energy is stored, TES technologies are conventionally divided into three main categories: sensible

heat storage, latent heat storage and thermochemical energy storage [7], [8]. These approaches differ in storage density, operating-temperature range, technological maturity, system complexity and cost, and their suitability therefore depends strongly on the characteristics of the specific application.

In sensible heat storage, energy is accumulated by increasing the temperature of a storage medium without inducing either a phase transition or a chemical reaction [9]. The stored thermal energy is therefore determined by the mass of the storage material, its specific heat capacity and the temperature interval over which the material operates. In its general form, the sensible energy stored between a cold temperature T_c and a hot temperature T_h can be expressed as

$$Q_{\text{sens}} = m \int_{T_c}^{T_h} c_p\,(T)\,dT \tag{1.1}$$

where m is the mass of the storage medium and $cp(T)$ its temperature-dependent specific heat capacity. When the variation of specific heat over the operating range is sufficiently small, the relationship can be approximated as

$$Q_{\text{sens}} \approx m c_p (T_h - T_c) \tag{1.2}$$

Consequently, materials characterised by high density and high specific heat capacity provide a high volumetric storage capacity, whereas a wide admissible temperature range further increases the amount of energy that can be stored. Sensible heat storage can employ both liquids and solids, including water, thermal oils, molten salts, concrete, ceramics and natural rocks. Its principal advantages are the simplicity of the storage mechanism, the availability of a broad range of materials and the possibility of using inexpensive and thermally stable media. These features make sensible TES one of the most mature storage approaches, particularly for medium- and high-temperature applications [8] , [10].

By contrast, latent heat storage exploits the enthalpy associated with a phase transition of the storage medium, most commonly the solid-liquid transition of a Phase Change Material (PCM). During charging, the PCM absorbs heat while undergoing the phase transition, whereas the reverse process releases the stored energy during discharge. Since a significant quantity of energy can be stored over a comparatively narrow temperature range, latent heat systems can provide higher effective energy densities than conventional sensible storage and can supply heat at an approximately constant temperature [11]. Nevertheless, their practical implementation involves additional challenges, including the selection and containment of the PCM, volume changes during phase transition, phase segregation, possible degradation under repeated cycling and the generally limited thermal conductivity of many candidate materials [11], [12]. These

aspects increase system complexity and can require additional heat-transfer enhancement measures [8].

A third possibility is thermochemical energy storage, in which thermal energy is converted into chemical potential through a reversible reaction. During the charging process, an endothermic reaction absorbs energy and produces reaction products that can subsequently be stored. During discharge, the reverse exothermic reaction releases the stored energy. Thermochemical storage can theoretically achieve high energy densities and is especially attractive for long-duration storage because, once the reaction products have been separated or stabilised, energy can be retained with very limited sensible thermal losses [13]. However, reaction kinetics, heat and mass transfer, material reversibility, reactor design and long-term chemical stability make thermochemical systems considerably more complex than conventional sensible heat storage [14]. Their technological maturity is consequently lower for many large-scale industrial applications [8].

Among these three approaches, sensible TES is particularly attractive for large-scale medium- and high-temperature storage when low cost, robustness, long lifetime and repeated thermal cycling are important requirements. Sensible storage systems can be further classified according to the nature of the storage medium and the way in which heat is exchanged with it. Liquid-based configurations are already well established. Water is widely employed at relatively low temperatures, while thermal oils and molten salts can be used at higher temperatures. Molten-salt storage has become especially relevant in Concentrating Solar Power (CSP) plants, where it enables solar heat collected during periods of high irradiation to be stored and subsequently dispatched after solar input decreases [15]. However, liquid media may introduce limitations associated with cost, chemical compatibility, corrosion, freezing temperature and maximum operating temperature. These considerations have stimulated substantial interest in solid sensible-storage materials, which can potentially offer wide operating-temperature ranges while using inexpensive and abundant materials [8], [15], [16].

One of the most extensively investigated solid sensible-storage concepts is Packed-Bed Thermal Energy Storage (PBTES)**.** A conventional packed-bed storage system consists of an insulated vessel filled with solid particles, rocks or pebbles. The spaces between the solid elements form an interconnected void fraction through which a Heat Transfer Fluid (HTF) can circulate. In a conventional charging process, the HTF is first heated by an external thermal source and then flows through the packed bed, transferring energy to the solid material. During discharge, the direction of energy transfer is reversed: a colder fluid enters the storage unit, extracts sensible heat from the solid particles and leaves the bed at an increased temperature. The storage capacity is therefore provided mainly by the solid filler, whereas the fluid is primarily responsible for

transporting thermal energy into and out of the bed [17], [18], [19]. Experimental work by Zanganeh et al. demonstrated packed-bed thermal storage using rocks as the storage medium and air as the working fluid, and the experimentally validated model was subsequently applied to the design of larger-scale systems [17].

Packed beds offer several attractive characteristics for large-scale TES. The use of solid filler materials makes it possible to employ low-cost natural materials or suitable industrial by-products, while the granular arrangement provides a large interfacial area between the storage medium and the HTF. This facilitates heat exchange without requiring complex internal heat-exchanger structures. Solid materials can also tolerate temperature ranges that would be problematic for several liquid heat-transfer and storage media. Furthermore, packed beds can be implemented as single-tank systems, reducing the quantity of expensive storage fluid and potentially decreasing system cost compared with conventional two-tank storage solutions. For these reasons, PBTES has been extensively investigated in the context of high-temperature renewable heat and CSP applications and is also considered a promising technology for industrial heat storage [18], [20], [21]. The literature includes both experimentally validated models and detailed studies of packed-bed topology, heat-transfer mechanisms and system design.

The choice of the heat-transfer fluid strongly affects the thermal and hydraulic behaviour of a packed-bed storage system. Gaseous and liquid HTFs can both be employed, with their suitability depending on operating temperature, system architecture and application requirements. Thermal oils provide favourable heat-transfer characteristics within their admissible temperature range but are limited by thermal degradation at high temperatures. Molten salts can operate at higher temperatures and possess relatively high volumetric heat capacity, but their use introduces challenges related to freezing, corrosion and material compatibility. Air, by contrast, is inexpensive, non-toxic, widely available and does not present freezing or decomposition constraints within the temperature range relevant to many high-temperature sensible-storage applications [22]. It is therefore particularly attractive for rock- or pebble-based storage systems. Its relatively low density and volumetric heat capacity, however, require larger volumetric flow rates and can lead to significant pressure losses through the packed bed, making fan or compressor consumption an important design consideration [18], [20], [22]. Zanganeh et al. specifically investigated high-temperature packed beds using air as the HTF for industrial-scale storage applications [20].

The hydraulic resistance of a packed bed is closely linked to its geometry and to the characteristics of the filler material. Particle diameter, bed porosity, vessel dimensions and fluid mass-flow rate affect both pressure drop and heat-transfer performance. Smaller particles generally

provide a larger solid-fluid interfacial area and can enhance thermal exchange, but they also increase the resistance encountered by the flowing fluid. Conversely, larger particles reduce pressure losses but may result in weaker solid-fluid heat transfer and larger internal temperature gradients [23]. Packed-bed design therefore requires a compromise between thermal performance and auxiliary energy consumption. Similar trade-offs arise when selecting the fluid mass-flow rate: increasing the flow rate can increase instantaneous thermal power and accelerate charging or discharging, but also increases pressure losses and modifies the evolution of the thermal front. These interactions explain why packed-bed performance cannot be assessed from storage capacity alone, but must also consider heat-transfer rate, pressure drop, thermal losses and discharge-temperature quality [18], [20], [24].

A distinctive feature of sensible packed-bed storage is the formation and propagation of a thermocline. During charging, the hot HTF entering the bed initially heats the solid material close to the inlet. As the process continues, a high-temperature region develops and progressively advances through the storage volume. A colder region remains further downstream, while the two regions are separated by a transition zone characterised by a substantial temperature gradient. This transition region is referred to as the thermocline. During discharge, an analogous thermal front travels through the bed as the stored energy is extracted. The ability to maintain a relatively narrow and well-defined thermocline is important because it allows a larger portion of the storage volume to remain close to either the hot or cold operating temperature, thereby preserving the quality of the energy delivered during discharge [18], [20].

The thickness and propagation velocity of the thermocline depend on several interacting parameters, including HTF velocity, particle diameter, porosity, solid-fluid heat-transfer coefficient, axial and radial heat transfer, thermophysical properties of both phases, tank geometry and heat losses through the vessel [25]. Thermal dispersion and conduction tend to broaden the transition region over time, reducing thermal stratification and causing the outlet temperature to deteriorate progressively during discharge. Repeated charging and discharging cycles can therefore produce a thermal behaviour different from that of an isolated single cycle, particularly if the bed is not completely returned to its initial thermal state between consecutive operations [26]. The design of high-temperature packed-bed systems must consequently consider cyclic operation and not only the performance of an individual charging or discharging process. Zanganeh et al. explicitly analysed these effects for industrial-scale packed beds and showed that design parameters such as tank geometry and particle diameter influence discharge temperature, pumping work and overall storage performance [20].

Heat losses to the surroundings constitute an additional mechanism affecting packed-bed performance. Although the storage vessel is thermally insulated, the temperature difference between the bed and the ambient environment produces heat transfer through the side walls and end surfaces. Their relative importance depends on storage temperature, insulation properties, tank dimensions and storage duration. At large scale, the surface-to-volume ratio decreases, which can reduce the relative importance of external thermal losses, but appropriate insulation remains essential, particularly for long storage periods [27]. Internal temperature non-uniformities must also be considered because heat losses are governed by local wall temperatures rather than solely by the average temperature of the storage medium. These effects become particularly relevant when the internal heat-generation or heat-transfer mechanism produces spatially non-uniform temperature distributions.

The selection of the solid filler material is therefore a key aspect of PBTES design. An appropriate storage material should combine a high volumetric heat capacity with thermal stability over the required operating-temperature range. Adequate thermal conductivity is desirable to reduce temperature gradients within individual particles and facilitate heat transfer, while resistance to mechanical degradation and repeated thermal cycling is essential for long-term operation [28]. Additional practical factors include availability, environmental impact, compatibility with the HTF and, particularly for large-scale storage, material cost. These requirements have motivated the investigation of natural rocks, quartzite, ceramics, concrete-based materials, slags and other industrial by-products as potential packed-bed fillers [8], [18]. Studies on alternative industrial materials, such as copper and induction-furnace slags, further illustrate the interest in exploiting inexpensive solids for high-temperature storage [29].

For a given tank volume and operating-temperature interval, volumetric heat capacity is particularly relevant because it directly determines the amount of sensible energy that can be stored within the available volume. Materials combining relatively high density and specific heat capacity can therefore reduce the volume required for a given storage capacity [30]. At the same time, the filler cannot be selected exclusively on the basis of storage density: thermal conductivity, particle morphology, pressure losses, cost and cycling behaviour influence the overall system response. As a result, the best material depends on the particular operating conditions and on the HTF with which it is coupled.

Among the possible solid storage materials, magnetite (Fe_3O_4) has been identified as an interesting candidate for medium-temperature sensible thermal storage. Filali Baba et al. performed a multilevel comparison between magnetite and quartzite, including thermophysical properties, thermal cycling and thermocline-storage performance over a medium-temperature

range. Their results showed that magnetite can provide a higher stored and recovered energy for the same tank size and discharge duration and may therefore reduce the storage volume required for a given amount of energy. Quartzite, however, displayed somewhat higher storage efficiencies, while the charging and discharging response was also shown to depend on the selected HTF and operating conditions [31]. Importantly, the study highlighted that packed-bed performance is determined not only by the filler material itself but by the interaction between storage material, heat-transfer fluid and system design.

Magnetite is particularly relevant to the present work for an additional reason. Besides acting as a sensible thermal-storage material, it is electrically conductive and exhibits ferromagnetic behaviour below its Curie temperature. These electromagnetic properties open the possibility of generating heat directly inside magnetite particles when they are exposed to a time-varying magnetic field. In a conventional PBTES, by contrast, electrical energy used for charging would first have to be converted into thermal energy by an external heating device and subsequently transferred to the bed through the HTF. Directly heating the solid storage medium offers the possibility of integrating the power-to-heat conversion mechanism with the thermal storage material itself. This concept constitutes the basis of the Induction-Heated Packed-Bed Thermal Energy Storage (IH-PBTES) system discussed in the following section.

1.2 Induction-heated packed-bed thermal energy storage

The possibility of directly heating the solid storage material introduced at the end of the previous section provides an alternative to conventional Power-to-Heat (PtH) configurations based on packed-bed storage. In a conventional electrically charged PBTES, electricity is first converted into heat by an external device, typically a resistive heater, and the generated thermal energy is subsequently transferred to a Heat Transfer Fluid (HTF). The hot fluid then flows through the packed bed and transfers heat to the solid filler. Although this configuration is conceptually simple, the charging process therefore involves two consecutive energy-transfer steps: from electricity to the HTF and from the HTF to the storage medium. When air is used as the HTF, the relatively low volumetric heat capacity and thermal conductivity of the fluid can limit the rate at which thermal energy is transferred to the bed, while forced circulation introduces additional auxiliary consumption and pressure losses. These characteristics can become particularly relevant when high charging rates and a rapid response to the availability of renewable electricity are required [18], [20].

A different approach consists in generating heat directly within the solid storage material [32]. Among the electrical heating technologies capable of achieving this objective, electromagnetic induction is especially attractive because it enables contactless and internally generated heating of materials having suitable electromagnetic properties [33]. Induction Heating (IH) is a mature electrothermal technology that has long been employed in industrial applications such as melting, forging and mass heating, heat treatment, welding and brazing. Its principal advantages include high achievable power densities, rapid dynamic response, accurate power control and the absence of direct electrical contact between the power supply and the material being heated [34], [35], [36]. While conventional industrial applications generally exploit induction to process metallic workpieces, the same physical principles can be applied to particulate materials and granular beds when the individual particles possess adequate electrical or magnetic properties [37].

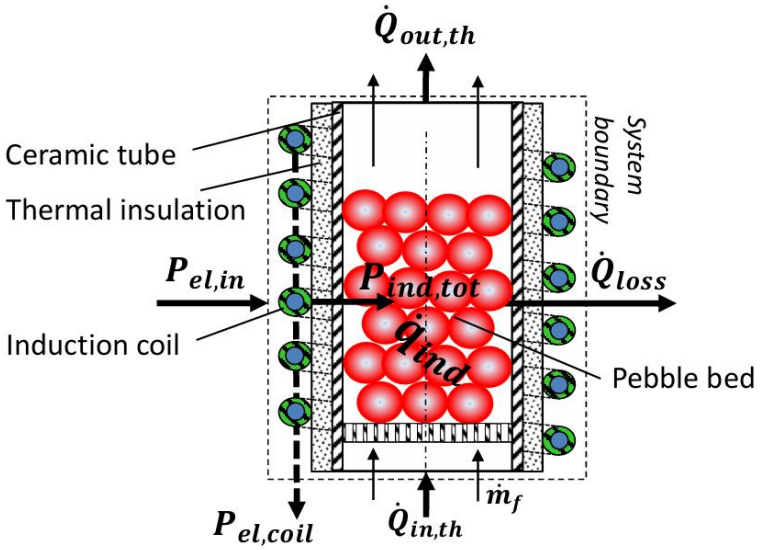


Figure 1.1– Conceptual arrangement and heat balance of an inductively heated pebble-bed system. Adapted from [32].

The basic principle of induction heating is based on electromagnetic coupling between an induction coil and the material located within its magnetic field. When an alternating electric current flows through a coil, a time-varying magnetic field is generated in the surrounding region. For an ideal infinitely long solenoid, the magnetic field strength inside the coil can be approximated as:

$$H \simeq \frac{NI}{L} \tag{1.3}$$

where N is the number of turns, I is the coil current and L is the coil length. This expression is useful for understanding the main dependence of magnetic-field strength on coil design and current. However, it represents an idealised condition. Real induction coils have finite dimensions,

and the magnetic field is consequently neither perfectly uniform nor exclusively axial. The field distribution depends on the coil geometry, turn spacing, distance between the coil and the target material and electromagnetic properties of the load. In particular, field distortion near the ends of finite coils and other electromagnetic effects can lead to significant spatial variations in the magnetic field and, consequently, in the locally generated heating power [35], [36], [38].

When the material exposed to the alternating magnetic field is electrically conductive, the time-varying magnetic flux induces circulating electrical currents within it according to Faraday's law. These currents, conventionally referred to as eddy currents, oppose the variation that generated them according to Lenz's law. Because the material has a finite electrical resistance, the induced currents dissipate electrical energy through the Joule effect, thereby generating heat directly within the material [39]. Eddy-current heating is therefore strongly influenced by the electrical conductivity of the target, the intensity and spatial distribution of the applied magnetic field, the operating frequency and the characteristic dimensions and geometry of the heated body [34], [35].

An important phenomenon associated with alternating-current induction is the skin effect, according to which the induced current density is not uniformly distributed throughout a conductive material but tends to become concentrated near its surface. Under the classical approximation of a homogeneous material, the characteristic penetration depth can be expressed as:

$$\delta = \sqrt{\frac{2}{\omega\mu\sigma}} = \frac{1}{\sqrt{\pi f \mu\sigma}} \tag{1.4}$$

where $\omega=2\pi f$ is the angular frequency, f is the excitation frequency, μ is the magnetic permeability and σ is the electrical conductivity of the material. The penetration depth therefore decreases as frequency, magnetic permeability or electrical conductivity increase [35], [36], [39]. Consequently, increasing frequency can enhance electromagnetic coupling but can also concentrate heat generation within a progressively smaller portion of the conductive material. Frequency selection in induction-heating systems is thus the result of a compromise between electrical efficiency, power density and the desired temperature uniformity [35], [36].

The electromagnetic behaviour of a granular packed bed is more complex than that of a single homogeneous workpiece. The solid phase is discontinuous and consists of a large number of particles separated by voids, while the geometry of the particles, their electromagnetic properties and their arrangement within the bed influence the effective response of the system.

Inductive heating of granular media has been investigated in previous studies, which demonstrated that the electromagnetic interaction between the induction coil and the granular load can be represented through appropriate equivalent descriptions of the electrically active bed [37]. This makes induction heating applicable not only to conventional continuous metallic components but also to particulate systems, opening the possibility of using the particles themselves as distributed heat sources [32], [37], [40].

A second heat-generation mechanism becomes relevant when the storage material is ferromagnetic. In this case, the alternating magnetic field repeatedly changes the magnetisation state of the material. Because the magnetisation does not respond reversibly and instantaneously to the applied field, the trajectory followed during magnetisation differs from that followed during demagnetisation, giving rise to a hysteresis loop in the M−H plane. The area enclosed by this loop represents magnetic energy dissipated during each complete magnetisation cycle. This energy is converted into heat and constitutes the magnetic hysteresis contribution to induction heating [35].

For a given ferromagnetic material, the volumetric energy dissipated through hysteresis during one cycle can be related to the hysteresis-loop area A_{hys} through:

$$e_{V,\mathrm{hys}} = \mu_0 A_{\mathrm{hys}} \tag{1.5}$$

and the associated volumetric heating power increases with the number of magnetisation cycles performed per unit time. Thus, in simplified terms,

$$\dot{q}_{\mathrm{hys}} \propto f e_{V,\mathrm{hys}} \tag{1.6}$$

The relationship between hysteresis power and operating conditions is nevertheless nonlinear because the hysteresis-loop area is itself a function of the peak magnetic-field strength, material properties and temperature. At low applied fields, the material may follow a minor hysteresis loop rather than the saturated major loop, so that estimating hysteresis heating requires a representation capable of describing both regimes. Noble et al. developed a modelling approach for major and minor magnetic-hysteresis loops specifically applicable to induction-heated particle beds, providing a basis for evaluating the energy dissipated under different magnetic-field amplitudes and temperatures [41].

Eddy-current and hysteresis heating may occur simultaneously, but their relative importance depends strongly on the material and operating conditions [42]. Highly conductive non-magnetic materials are heated essentially through eddy-current dissipation, whereas ferromagnetic materials may exhibit an additional and potentially substantial hysteresis

contribution. Frequency also affects the two mechanisms differently. Eddy-current generation depends on the induced electric field and current distribution, while hysteresis power depends both on the energy dissipated in each magnetisation cycle and on the frequency with which the cycle is repeated. The current supplied to the induction coil is similarly important because it governs the intensity of the generated magnetic field. The combination of coil current, operating frequency, coil geometry and material properties therefore determines both the total amount of heat produced and its spatial distribution [34], [35], [36].

These dependencies are particularly important for thermal-energy-storage applications because the target is fundamentally different from that of many conventional induction-heating processes. In surface hardening, welding or other manufacturing operations, intense and highly localised heating can be desirable. In a thermal storage system, by contrast, the objective is to increase the temperature of a large mass of storage material while maintaining acceptable temperature gradients and avoiding local overheating. A high total heating power is beneficial because it reduces charging time, but excessive localisation of the electromagnetic heat source can generate hot spots and leave other regions of the storage medium comparatively cold. The design of an induction-heated storage system must therefore consider not only the total induction power but also the spatial uniformity with which this power is deposited [43].

This requirement becomes even more important because the electromagnetic properties governing induction heating are themselves temperature dependent. Induction heating is therefore an intrinsically coupled electromagnetic–thermal phenomenon: the electromagnetic field determines the local heat generation, this heat generation modifies the temperature field and the evolving temperature subsequently modifies the electromagnetic response of the material [35], [44]. Electrical resistivity, magnetic permeability, saturation magnetisation and hysteresis characteristics can all vary substantially during heating, and assuming constant properties over a wide temperature range may consequently fail to capture important aspects of the process.

Magnetite is a particularly representative example of this coupling. Experimental measurements performed on magnetite have shown that its magnetic behaviour varies strongly with temperature [45]. Dunlop investigated the high-temperature magnetic susceptibility of magnetite and showed a significant temperature dependence approaching the Curie transition [46]. Subsequent measurements of magnetic hysteresis over a wide range of magnetite grain sizes showed that coercivity and remanent magnetic properties evolve considerably between room temperature and the Curie region [47]. For magnetite, the Curie temperature is approximately 580–

585 °C; as this temperature is approached, the ferromagnetic response progressively disappears, with a consequent strong reduction of hysteresis heating [46], [47] , [48].

The electrical behaviour of magnetite also varies with temperature [49]. Measurements on single-crystal magnetite performed by Botrous El Badramany et al. showed a monotonic decrease of DC electrical resistivity with increasing temperature between approximately 300 and 800 K [50]. Since electrical conductivity is the inverse of resistivity, this behaviour implies an increase in conductivity over this temperature interval. Such a variation is directly relevant to eddy-current heating, for which the electrical properties of the particles influence the induced currents and the associated Joule dissipation. Magnetite can therefore exhibit two competing temperature-dependent tendencies: its magnetic hysteresis contribution generally weakens as temperature rises towards the Curie point, whereas changes in electrical conductivity can favour stronger eddy-current generation. Capturing these opposite trends is essential when analysing the transient behaviour of an induction-heated magnetite bed.

The combination of these physical characteristics with the sensible-storage properties discussed in Section 1.1 forms the basis of the Induction-Heated Packed-Bed Thermal Energy Storage (IH-PBTES) concept. In this configuration, the packed bed does not act solely as a passive thermal-storage medium. Its solid particles also behave as electromagnetic susceptors and directly convert part of the electrical energy supplied to the induction system into heat. Power-to-heat conversion and thermal-energy storage are therefore integrated within the same material domain.

A representative IH-PBTES configuration consists of a cylindrical vessel containing the solid storage particles and surrounded by an induction coil. The coil is supplied with alternating current at a prescribed frequency through an appropriate power-electronic conversion system. The alternating current generates a time-varying magnetic field that penetrates the packed bed and interacts with the particles. If the filler is electrically conductive, eddy currents produce Joule heating within the particles; if it is ferromagnetic, magnetic hysteresis provides an additional heat-generation mechanism. The heat produced is directly accumulated as sensible thermal energy through the increase in temperature of the solid material. The packed bed is thermally insulated from the surroundings, while the containing structure must be designed so as not to undesirably interfere with the electromagnetic field. In practical induction systems, the coil is generally manufactured from highly conductive copper tubing and is actively cooled in order to limit the temperature rise of the conductor and the associated electrical resistance and Joule losses [35], [36].

The charging principle consequently differs fundamentally from that of a conventional PBTES. During induction charging, no continuously circulating hot HTF is required to transport

energy from an external heater to the storage particles. Instead, the electromagnetic field generates heat directly throughout the inductively active portion of the packed bed. The HTF can then be introduced when stored thermal energy is required. During the discharging phase, a fluid such as air flows through the void space of the packed bed, receives heat from the hot solid particles by convection and transports the recovered thermal energy towards the final process. The system therefore retains the conventional and well-established packed-bed mechanism for thermal discharge while replacing the indirect charging process with direct electromagnetic heating of the storage material.

This separation between the charging and discharging mechanisms is one of the most distinctive features of the concept. The charging process is governed primarily by electromagnetic heat generation, heat conduction within the packed bed and thermal losses towards the environment, whereas discharge is governed by the interaction between the solid thermal mass and the flowing HTF. This provides additional operational flexibility, since electrical charging can in principle be scheduled according to electricity availability or price independently of the instantaneous industrial heat demand, while the stored sensible energy can subsequently be recovered when needed.

The suitability of the solid filler for IH-PBTES consequently depends on a broader set of properties than in a conventional packed bed. In addition to high density, high heat capacity, adequate thermal conductivity, thermal stability, mechanical resistance and low cost, the material must exhibit electromagnetic properties capable of producing a useful induction-heating response. Electrical conductivity is required for significant eddy-current generation, while ferromagnetic behaviour enables hysteresis heating. These requirements explain the particular interest in iron-based materials and especially in magnetite. As discussed previously, magnetite can provide favourable sensible-storage characteristics [31], while its electrical conductivity and ferromagnetic nature allow the same particles to act as induction susceptors. The storage and heating functions can therefore be combined without introducing a separate high-cost active material into the packed bed.

Nevertheless, the direct integration of induction heating and packed-bed storage also introduces new design challenges. The induction coil itself dissipates electrical energy because of its finite resistance, and the magnitude of these losses depends on current, frequency, coil geometry and temperature. Power-electronic conversion introduces additional losses whose relevance generally increases with switching frequency [51]. At the same time, increasing current or frequency can enhance the heat generated in the packed bed. Selection of the operating point must

therefore balance useful induction power against coil and conversion losses, rather than simply maximising either current or frequency [35], [36], [51].

An equally important challenge concerns thermal uniformity. Since a finite coil does not generate a perfectly uniform magnetic field, different regions of the storage domain can experience different field amplitudes. Because both eddy-current and hysteresis heat generation depend on the local electromagnetic excitation, the resulting heat-source distribution can also be non-uniform. The system geometry, and in particular the relative dimensions of the packed bed and the coil, can consequently influence not only the average heating power but also the location and magnitude of local temperature maxima. The temperature dependence of the material properties further strengthens this coupling, as regions that initially heat more rapidly may subsequently exhibit a different electromagnetic response from colder regions.

These effects highlight an important distinction between evaluating the global feasibility of the IH-PBTES concept and predicting its actual transient thermal behaviour. Simplified models based on a representative magnetic-field intensity and a single average packed-bed temperature can provide useful first estimates of induction efficiency, required current, operating frequency and overall heating power. Such models are valuable for preliminary design and for identifying feasible orders of magnitude. However, the use of spatially averaged quantities cannot describe local variations of magnetic-field strength, distributed heat generation or temperature within the bed. It therefore cannot directly determine whether a given operating condition produces a sufficiently uniform thermal state or instead generates localised hot regions.

For this reason, a spatially resolved representation becomes particularly relevant when analysing induction-heated thermal storage. The finite geometry of the coil requires the magnetic field to be considered as a function of position, while the corresponding induction heat source must be linked to the local electromagnetic excitation. At the same time, thermal conduction, external heat losses and temperature-dependent material properties cause the temperature field to evolve both spatially and temporally. A realistic assessment of the charging process therefore requires these phenomena to be considered together. Furthermore, evaluating IH-PBTES as an actual storage technology requires the analysis to extend beyond charging alone and to include the subsequent recovery of heat through a flowing HTF and the behaviour of the system under repeated charge–discharge operation. These aspects define the framework and objectives of the present thesis, which are introduced in the following section.

Previous studies have investigated induction heating in granular and packed-bed systems with different levels of modelling detail. Duquenne et al. [37] introduced an equivalent electrical representation of conductive granular media subjected to an alternating electromagnetic field,

relating the electrical impedance of the bed to the induced heat generation. Niu et al. [40] subsequently developed an unsteady two-dimensional model in cylindrical coordinates for a two-layer packed bed of iron and graphite heated in a high-frequency induction furnace, including temperature-dependent material properties and validating the predicted thermal response against experimental measurements. More recently, Belik et al. [32] proposed and experimentally validated a three-dimensional coupled electromagnetic–thermal model of an inductively heated pebble-bed gas heater, resolving the heat generation and temperature distribution within the granular domain. Further studies have investigated the spatial distribution of induction heating at particle scale [59] and experimentally demonstrated non-uniform temperature distributions in inductively heated catalytic beds [60]. These works demonstrate that spatially resolved modelling of induction-heated granular media has already been addressed in the literature, although primarily in the context of furnaces, gas heaters and chemical-process applications rather than thermal-energy storage.

1.3 Scope and objectives of the thesis

To the best of the authors' knowledge, however, no previous study has applied such a spatially resolved approach to the specific IH-PBTES concept while combining the non-uniform electromagnetic excitation produced by a finite induction coil with transient thermal storage, subsequent air-based discharge and repeated charge–discharge operation.

The present work builds upon the previously developed numerical framework for Induction-Heated Packed-Bed Thermal Energy Storage (IH-PBTES) proposed by Famiglietti and Abbas [52]. The reference model was conceived as a system-level tool for assessing the technical feasibility of the IH-PBTES concept and for identifying suitable operating ranges in terms of electromagnetic power transfer and volumetric heat-generation rate. However, both the electromagnetic and thermal descriptions were spatially averaged: the magnetic field generated by the induction coil was represented by a single characteristic value, while the thermal state of the packed bed was described through a single representative temperature. Although this formulation is appropriate for preliminary feasibility studies, it cannot describe the spatial non-uniformities associated with a finite induction coil or the resulting local temperature gradients within the storage medium.

The main objective of this thesis is therefore to extend the reference IH-PBTES framework towards a spatially resolved representation of the charging, discharging and cyclic behaviour of

the storage system. In particular, the packed bed is described through a two-dimensional axisymmetric r-z domain in which both the magnetic-field distribution, $H(r, z)$, and the transient temperature field, $T(r, z, t)$, are resolved. This extension makes it possible to move beyond average quantities and to evaluate how the spatial distribution of electromagnetic excitation influences local heat generation, temperature non-uniformity and the development of hot regions within the storage medium.

The first objective concerns the charging phase. The magnetic field generated by the finite induction coil is evaluated throughout the computational domain and used to construct spatially distributed induction heat-generation terms. The thermal formulation is correspondingly extended to account for two-dimensional heat conduction, local heat losses at the boundaries and temperature-dependent thermophysical and electromagnetic properties of magnetite. Before analysing the complete non-uniform problem, the new two-dimensional thermal implementation is validated against the reference lumped model under equivalent uniform-source conditions. This comparison is intended to verify that the introduction of the spatial thermal domain does not alter the global thermal response when spatial variations of the heat source are deliberately suppressed. The validated framework is subsequently used to investigate the characteristic behaviour of the hysteresis and eddy-current contributions separately and to assess the influence of packed-bed aspect ratio under comparable electromagnetic excitation.

A second objective is to extend the analysis beyond the charging process and investigate the recovery of the stored thermal energy. For this purpose, the final two-dimensional temperature distributions obtained from the charging simulations are used as the initial thermal state of an air-based discharge model. The solid phase retains its spatially resolved temperature description, while the heat-transfer fluid extracts sensible energy from the packed bed as it flows towards the outlet. Different air mass-flow rates are examined in order to quantify the resulting trade-off between discharge duration, outlet-air temperature and recovered thermal power. In this way, the analysis is not limited to the amount of energy introduced during charging, but also considers the temperature level and rate at which that energy can subsequently be delivered.

The third objective is to investigate repeated charge-discharge operation. This extension is required because the packed bed is not necessarily returned to a uniform initial condition after each discharge. Instead, the residual two-dimensional temperature distribution becomes the initial condition of the subsequent charging phase and can progressively affect both the global performance and the local thermal state of the system. Two comparison criteria are therefore considered for the isolated hysteresis and eddy-current charging cases: operation under the same cumulative electrical-energy input and operation towards the same mean packed-bed temperature.

The cyclic analysis is used to examine the evolution of charging energy, recovered thermal energy, round-trip performance and local temperature maxima over successive cycles.

The scope of the present work remains that of a spatially resolved system-level numerical framework. The two-dimensional formulation increases the physical detail of the reference model without attempting to resolve the complete particle-scale electromagnetic problem. In particular, the magnetic-field model captures the spatial variation and end effects produced by the finite coil but does not constitute a fully coupled Maxwell solution including the electromagnetic response of the individual particles, while the eddy-current contribution retains the equivalent formulation inherited from the reference model rather than resolving microscopic current-density distributions within each pebble. These assumptions allow transient, parametric and cyclic simulations to remain computationally tractable while providing substantially more information on local thermal behaviour than the original lumped approach.

Overall, the thesis aims to establish a numerical framework capable of linking the spatial distribution of electromagnetic heating to the transient thermal response of the packed bed throughout charging, discharge and repeated operation. Particular attention is devoted to the interaction between magnetic-field non-uniformity, temperature-dependent material properties, packed-bed geometry and the two induction-heating mechanisms. The resulting model is therefore intended not only to assess global performance indicators, but also to identify local thermal effects that cannot be captured by a spatially averaged representation and that are relevant to the future design and operation of IH-PBTES systems for industrial process-heat applications.

2. Methodology

The numerical methodology adopted in this work follows a progressive extension of the reference IH-PBTES framework from a spatially averaged description towards a two-dimensional representation of the charging, discharging and cyclic behaviour of the storage system. Rather than replacing the original formulation entirely, the main physical and energy-balance relationships of the reference model are retained where appropriate and progressively coupled with additional spatial and temperature-dependent descriptions. This approach makes it possible to preserve the modelling basis previously established for the IH-PBTES concept while introducing the level of spatial resolution required to investigate local electromagnetic heat generation and temperature non-uniformities within the packed bed.

The chapter is organised according to this modelling progression. Section 2.1 first introduces the reference IH-PBTES framework and the assumptions inherited by the present work. Section 2.2 describes the charging formulation and the coupling between electromagnetic heat generation and the transient thermal response. The spatial magnetic-field model is then presented in Section 2.3, followed by the temperature-dependent properties of magnetite in Section 2.4. Sections 2.5 and 2.6 describe the two-dimensional thermal formulation and the treatment of heat losses and boundary conditions, respectively. The methodology is subsequently extended to thermal-energy recovery through the air-based discharging model presented in Section 2.7. Finally, Section 2.8 describes the coupling of charging and discharging calculations used to simulate repeated charge-discharge cycles and to propagate the residual thermal state between consecutive operating cycles.

2.1 Reference IH-PBTES Model

The numerical framework developed in the present thesis originates from the Induction-Heated Packed-Bed Thermal Energy Storage model proposed by Famiglietti and Abbas [52]. The reference model was developed as a physically based, system-level framework for assessing the technical viability of directly coupling electromagnetic induction heating with sensible thermal energy storage in a packed bed. Its main purpose was to identify feasible operating ranges in terms of induction efficiency and volumetric heating power density while retaining a sufficiently low computational complexity for parametric analyses. The formulation accounts for the principal energy-conversion mechanisms involved in the system, including magnetic hysteresis and eddy-current heat generation within the storage material, Joule losses in the induction coil, losses

associated with the frequency converter, and thermal losses from the storage unit to the ambient environment [52].

The physical configuration consists of a cylindrical vessel filled with solid pebbles and surrounded by a coaxial induction coil. During charging, alternating electrical current is supplied to the coil through a frequency converter. The resulting alternating magnetic field interacts directly with the solid particles, which therefore act simultaneously as sensible heat-storage material and electromagnetic susceptors. If the filler material is electrically conductive, eddy currents are induced within the particles and dissipate energy through Joule heating; if the material is ferromagnetic, magnetic hysteresis provides an additional heat-generation mechanism. The thermal energy generated by these mechanisms is stored as sensible heat in the packed bed. During discharge, thermal energy can subsequently be extracted by circulating a heat-transfer fluid through the void fraction of the bed [52].

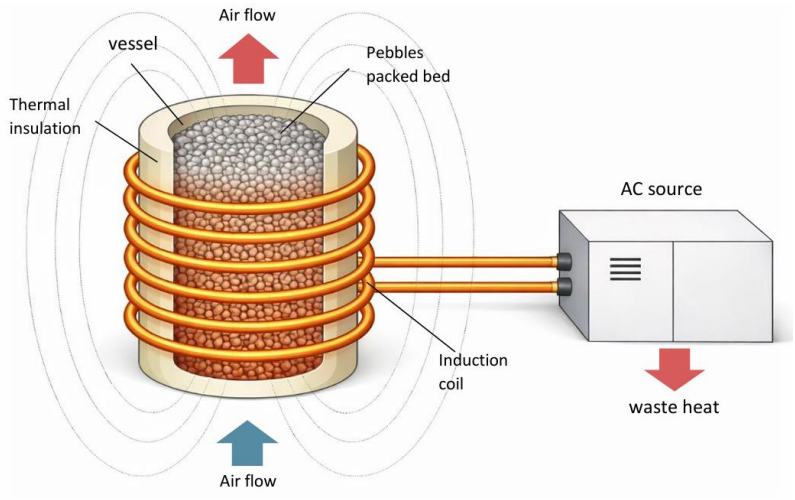


Figure 2.1-Schematic representation of the induction-heated packed-bed thermal energy storage system. Reproduced from [52]

The packed bed is represented as a cylindrical domain of diameter D_{PB} and height H_{PB}. Its geometry can be conveniently characterised through the aspect ratio defined as follows:

$$AR = \frac{H_{PB}}{D_{PB}} \tag{2.1}$$

The corresponding packed-bed volume is:

$$V_{PB} = \frac{\pi D_{PB}^2}{4} H_{PB} \tag{2.2}$$

The solid filler is represented by spherical and monodisperse pebbles having a characteristic diameter D_p. The packed-bed void fraction is denoted by ε, so that the fraction of the total volume occupied by the solid material is equal to $1-\varepsilon$. The effective mass of storage material can therefore be expressed as:

$$M_{PB} = (1 - \varepsilon)\rho_s V_{PB} \tag{2.3}$$

where ρ_s is the density of the solid storage material. The packed bed is enclosed within a cylindrical refractory vessel and surrounded by an external thermal-insulation layer. The induction coil is positioned externally with respect to the storage domain. Its geometrical arrangement and the principal dimensions entering the reference model are illustrated in Figure 2.2 [52].

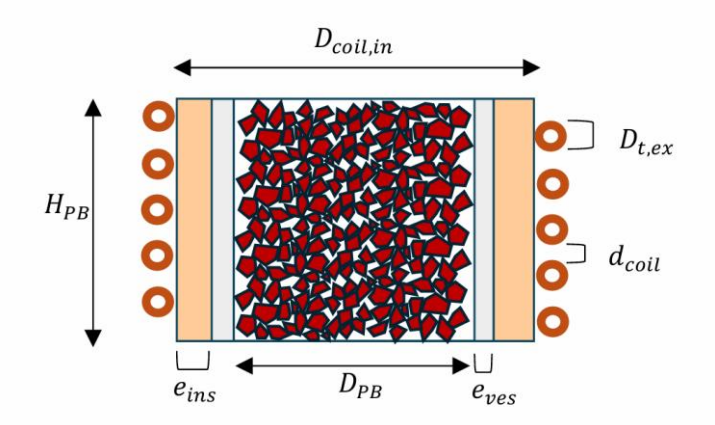


Figure 2.2-Cross-sectional view of the reference IH-PBTES configuration and definition of the main geometrical parameters. Reproduced from [52]

Here, e_{ves} denotes the thickness of the refractory vessel surrounding the packed bed. Although this quantity is introduced in the geometrical definition of the reference system, no numerical value is reported for it in the reference parameter set of [52].

A representative large-scale configuration was adopted in the original technical-viability study in order to establish realistic orders of magnitude for industrial thermal-energy-storage applications. The principal geometrical and reference parameters of this configuration are reported in Table 2.1. These values refer specifically to the configuration used in the original viability analysis and are reported here to define the scale on which the reference framework was assessed; they should not be confused with the geometry subsequently adopted for the two-dimensional simulations developed in the present thesis [52].

Parameter	**Symbol**	**Value**
Packed-bed diameter	D_{PB}	2.5 m
Packed-bed height	H_{PB}	5.0 m
Packed-bed void fraction	ε	0.40
Pebble diameter	D_p	0.020 m
Coil diameter	$D_{\mathrm{coil,in}}$	2.7 m
Coil height	H_{coil}	5.0 m
Coil-tube outer diameter	$D_{t,\mathrm{out}}$	0.025 m

Coil-tube wall thickness	e_t	0.002 m
Distance between consecutive turns	d_{coil}	0.050 m
Insulation thickness	e_{ins}	0.10 m
Coil reference temperature	T_{coil}	60 °C
Packed-bed reference temperature	T_{PB}	300 °C
Ambient reference temperature	T_{amb}	25 °C

Table 2.1-Main parameters of the reference IH-PBTES configuration adopted in [52].

The reference model relies on a number of simplifying assumptions intended to retain a level of complexity compatible with system-level and parametric analyses. The pebbles are assumed to be spherical and monodisperse, and the temperature within each individual particle is considered spatially uniform. Eddy-current and magnetic-hysteresis heating are treated as independent physical contributions whose thermal effects can be superimposed. Most importantly for the developments introduced in the present thesis, the applied magnetic field is assumed to be homogeneous throughout the packed-bed volume, with no radial or axial gradients [52].

In the numerical implementation inherited as the starting point of the present work, the induction coil is represented through a solenoidal approximation. For a root-mean-square coil current I and a coil composed of N turns over a height H_{coil}, the representative rms magnetic-field strength is evaluated as:

$$H_{\text{rms}} = \frac{NI}{H_{\text{coil}}} \tag{2.4}$$

and the corresponding peak magnetic-field strength used in the hysteresis formulation is:

$$H_m = \sqrt{2} H_{\text{rms}} \tag{2.5}$$

The same representative field is therefore assigned to the entire storage volume. This approach establishes a direct relationship between coil current and electromagnetic excitation but neglects the spatial variations associated with the finite dimensions of an actual induction coil. In particular, radial variations and the end effects occurring close to the upper and lower extremities of the winding cannot be represented by the reference formulation. The inherited numerical implementation explicitly follows this uniform-field approach.

The total electromagnetic power generated within the storage material is expressed as the sum of the contributions associated with magnetic hysteresis and eddy-current dissipation:

$$P_{\text{ind}} = P_{\text{hys}} + P_{\text{eddy}} \tag{2.6}$$

for an electrically conductive and ferromagnetic material such as magnetite, the two physical phenomena are expected to occur simultaneously. Their mathematical separation is therefore not intended to represent two alternative operating strategies, but enables their individual contributions to the total induced power to be evaluated separately. This distinction is particularly relevant in the present thesis, where isolated hysteresis-dominated and eddy-current-dominated cases are subsequently analysed in order to investigate the characteristic thermal behaviour associated with each contribution.

The hysteresis contribution is obtained from the magnetic energy dissipated during one complete magnetisation cycle. In the inherited framework, major and minor hysteresis loops are represented through the LangArc formulation, using temperature-dependent parameters describing the reversible and irreversible magnetisation components, the characteristic field and the saturation magnetisation. The area enclosed by the resulting hysteresis loop determines the energy dissipated per cycle, which is subsequently converted into heating power through the excitation frequency and the amount of magnetically active material. This formulation follows the approach adopted for induction-heated particle beds by Noble et al. [41]. The detailed implementation of the hysteresis source term used during charging is presented in Section 2.2, while the temperature dependence of its governing parameters is discussed in Section 2.4.

The eddy-current contribution is represented through an equivalent electrical description of the granular packed bed. The pebbles are considered electrically insulated from one another, so that eddy currents are induced independently within the individual particles rather than flowing through a continuous conducting matrix. Instead of resolving the microscopic current-density distribution inside every pebble, the electromagnetic load associated with the granular bed is represented by an equivalent resistance referred to the induction-coil side. The corresponding eddy-current heating power is therefore expressed as

$$P_{\mathrm{eddy}} = R_{\mathrm{eq}} I^2$$

where I is the rms current supplied to the induction coil and R_{eq} is the equivalent load resistance associated with eddy-current dissipation in the packed bed. Therefore, Idoes not represent the microscopic eddy current circulating within an individual particle, but the same coil current used to determine the electromagnetic excitation of the system.

In the inherited numerical implementation of the reference model, the equivalent resistance is evaluated as

$$R_{\mathrm{eq}} = \frac{2(1-\varepsilon)(\pi D_{\mathrm{coil}} N)^2}{H_{\mathrm{coil}} K_i D_p} \left(10^{-7} \frac{\mu_{r,p} f}{\sigma_p}\right)^{1/2} F(f)$$

where ε is the packed-bed void fraction, D_{coil} and H_{coil} are the diameter and height of the induction coil, respectively, N is the number of coil turns, D_p is the particle diameter, f is the excitation frequency, and σ_p and $\mu_{r,p}$ are the electrical conductivity and relative magnetic permeability of the particles. The geometrical correction factor K_i is defined as

$$K_i = 1 + 0.44\frac{D_{\mathrm{coil}}}{H_{\mathrm{coil}}}$$

The factor $F(f)$is the frequency-dependent power-transmission factor inherited from the reference eddy-current formulation and accounts for electromagnetic penetration into the particles. It is evaluated as a function of the particle skin depth and therefore depends on the excitation frequency and electromagnetic properties of the storage material. Its role in the construction of the spatially distributed eddy-current source is discussed in Section 2.2, while the temperature dependence of the electromagnetic penetration depth is introduced in Section 2.4. The equivalent resistance therefore incorporates the effects of packed-bed and coil geometry, solid volume fraction, particle size, electromagnetic material properties and excitation frequency into a single coil-referred load parameter. This formulation should be interpreted as a global equivalent representation of the eddy-current power absorbed by the granular medium, rather than as the physical resistance of a continuous packed-bed conductor or as a direct solution of the microscopic current-density distribution inside each pebble [52].

This distinction is maintained in the present thesis. The development of a spatially resolved thermal model does not introduce a microscopic eddy-current calculation at particle scale. Instead, the global equivalent formulation inherited from the reference model is retained and subsequently coupled with the two-dimensional description of the magnetic field and thermal domain.

The induction coil introduces an additional electrical loss because of the finite resistance of the copper conductor. In alternating-current operation, its effective resistance accounts for the temperature dependence of copper resistivity as well as skin and proximity effects. The corresponding Joule loss is expressed as:

$$P_{\mathrm{coil}} = R_{\mathrm{coil,AC}} I^2 \tag{2.8}$$

The electrical power transferred to the combined coil–load system can consequently be written as:

$$P_{\mathrm{el}} = P_{\mathrm{ind}} + P_{\mathrm{coil}} \tag{2.9}$$

An additional loss is associated with the upstream frequency converter. Denoting its efficiency by η_{conv}, the electrical input power is:

$$P_{\mathrm{in}} = \frac{P_{\mathrm{el}}}{\eta_{\mathrm{conv}}} \tag{2.10}$$

and the corresponding conversion loss is:

$$P_{\mathrm{conv}} = P_{\mathrm{in}} - P_{\mathrm{el}} \tag{2.11}$$

The reference framework therefore distinguishes the electromagnetic power deposited in the packed bed from electrical losses occurring in the induction coil and power-electronic conversion stage. This separation is retained in the present work because it enables the thermal behaviour of the storage medium to be analysed together with the principal electrical penalties associated with induction charging. On the thermal side, the numerical implementation used as the starting point of this thesis adopts a lumped representation of the packed bed. The entire storage medium is described by a single time-dependent representative temperature $T_{PB}(t)$. Consequently, radial and axial temperature gradients within the packed bed are not resolved, and internal thermal conduction between different regions of the storage volume is not explicitly represented.

The net thermal power contributing to the increase of sensible energy stored in the packed bed is calculated as the difference between the total induced power and heat losses to the ambient environment:

$$P_{\mathrm{ch}} = P_{\mathrm{ind}} - P_{\mathrm{amb}} \tag{2.12}$$

Ambient heat losses are represented through a lumped thermal-resistance approach. Heat is transferred radially through the external insulation layer and subsequently from the outer surface to the surrounding environment by convection. The loss calculation is based on the representative packed-bed temperature and the ambient temperature, so that local variations of the wall temperature are not resolved in the reference formulation [52]. The detailed thermal-resistance formulation and its extension to local boundary conditions in the two-dimensional model are presented in Section 2.6.

The transient thermal response of the reference packed bed is consequently governed by the global sensible-energy balance:

$$M_{PB} c_{p,s} \frac{dT_{PB}}{dt} = P_{\mathrm{hys}} + P_{\mathrm{eddy}} - P_{\mathrm{amb}} \tag{2.13}$$

Using the definition of the net charging power, the same balance can be written in compact form as:

$$M_{PB} c_{p,s} \frac{dT_{PB}}{dt} = P_{\mathrm{ch}} \tag{2.14}$$

In the inherited numerical implementation, this equation is advanced explicitly in time. At each time step, the induction and ambient-loss powers are recalculated at the current packed-bed temperature and the temperature is updated according to:

$$T_{PB}^{n+1} = T_{PB}^{n} + \frac{P_{\mathrm{ch}}^{n}\Delta t}{M_{PB}c_{p,s}} \tag{2.15}$$

The lumped formulation therefore describes the evolution of the complete storage system through a single thermal state variable. While this representation is computationally efficient and appropriate for preliminary feasibility assessments, it cannot determine whether the induced power is deposited uniformly within the storage volume or whether local temperature maxima develop during charging. Two principal performance indicators are used in the reference framework. The induction efficiency quantifies the fraction of the electrical power delivered to the coil–load system that is electromagnetically transferred to the packed bed rather than dissipated by Joule heating in the coil,

$$\eta_{\mathrm{ind}} = \frac{P_{\mathrm{ind}}}{P_{\mathrm{ind}} + P_{\mathrm{coil}}} \tag{2.16}$$

In addition to the induction efficiency, three complementary efficiency indicators are used in the subsequent charging analysis. The frequency-converter efficiency quantifies the fraction of the upstream electrical input that is delivered to the coil–load system, whereas the thermal charging efficiency accounts for the fraction of the induced power that effectively contributes to increasing the sensible energy of the packed bed after ambient heat losses. They are defined as

$$\eta_{conv} = \frac{P_{el}}{P_{in}} = 1 - \frac{P_{conv}}{P_{in}}$$

$$\eta_{th} = \frac{P_{ch}}{P_{ind}} = \frac{P_{ind} - P_{amb}}{P_{ind}}$$

Combining the converter, induction and thermal contributions, an overall charging efficiency is defined as

$$\eta_{ch} = \frac{P_{ch}}{P_{in}} = \eta_{conv}\eta_{ind}\eta_{th}$$

The quantity η_{ch} therefore represents an instantaneous charging-stage efficiency evaluated at the current thermal state of the packed bed. It includes frequency-converter losses, coil Joule losses and ambient thermal losses occurring during charging. It does not account for the subsequent discharge process.

The second indicator is the volumetric induction-heating power density, defined as:

$$\dot{q}_{\mathrm{ind}} = \frac{P_{\mathrm{ind}}}{V_{PB}} \tag{2.17}$$

The induction efficiency characterises the effectiveness of electromagnetic power transfer relative to coil losses, whereas the volumetric power density indicates the rate at which heat is generated per unit packed-bed volume. The original viability analysis used these two quantities to identify operating conditions capable of simultaneously providing efficient electrical-to-thermal conversion and charging rates compatible with thermal-energy-storage applications [52].

The reference model provides a computationally efficient and physically based representation of the principal mechanisms governing induction charging of a packed-bed thermal storage system. Its spatially averaged formulation is appropriate for evaluating global performance and for identifying the dominant dependencies on coil current, excitation frequency, system geometry and material properties. However, the assumptions that enable this computational simplicity also define the main limitations addressed in the present thesis. In particular, the homogeneous-field approximation cannot capture the radial and axial variations produced by a finite induction coil, while the lumped thermal formulation cannot describe internal temperature gradients, conductive redistribution of heat or the formation of local hot spots. Thermal losses are likewise evaluated from a representative packed-bed temperature rather than from the local temperatures of the system boundaries. Furthermore, the reference charging framework does not describe the dynamic extraction of stored heat by a flowing heat-transfer fluid or the propagation of a residual temperature distribution through repeated charge–discharge cycles. These limitations constitute the starting point for the developments introduced in the present work. The physical and energy-balance structure of the reference framework is retained where appropriate, while the packed bed is progressively reformulated as a spatially resolved axisymmetric domain. The following sections describe the charging formulation adopted in the present model, the calculation of the two-dimensional magnetic-field distribution, the introduction of temperature-dependent material properties, the two-dimensional thermal formulation and boundary conditions, and the subsequent extension of the framework to discharging and repeated cyclic operation.

2.2 Charging Model

The charging model developed in the present work describes the transient heating of the packed bed during induction charging under axisymmetric conditions. In this phase, the storage unit is directly heated by the electromagnetic field generated by the surrounding induction coil, while no heat-transfer fluid is circulated through the bed. The model receives as principal inputs the coil current, the excitation frequency, the initial thermal state of the packed bed and the system geometry. Starting from these quantities, the magnetic-field distribution is evaluated over the computational domain and used to construct a spatially distributed volumetric heat source. This local source term is then coupled with the transient thermal model in order to calculate the evolution of the temperature field within the packed bed. Compared with the lumped formulation described in Section 2.1, the charging model developed in this thesis introduces two essential extensions. First, the induction source is no longer treated as a single global power term, but as a local volumetric heat-generation map defined over the two-dimensional axisymmetric domain. Second, the source term is recalculated during the transient as a function of the local temperature, so that the electromagnetic and thermal problems are coupled through the temperature dependence of the material properties. The charging model therefore provides a spatially resolved description of the induction-heating process while preserving the physical structure of the original reference framework.

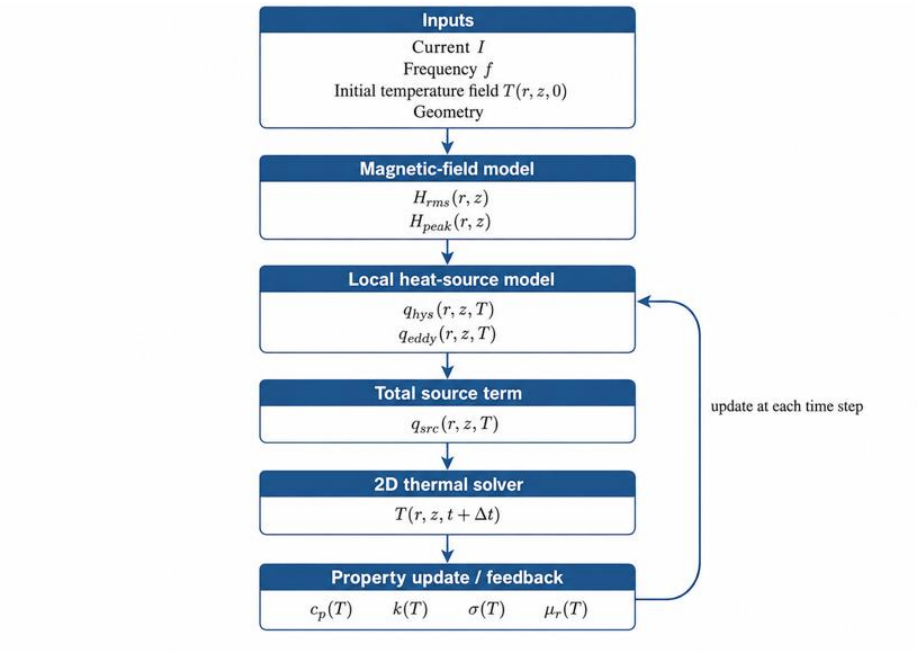


Figure 2.3– Workflow of the charging model adopted in the present work.

The local magnetic-field map is the starting point of the charging calculation. For each point of the axisymmetric domain, the rms magnetic-field strength is evaluated through the

electromagnetic model described in the following section. The corresponding local peak field is then obtained as:

$$H_{\mathrm{peak}}(r,z) = \sqrt{2}\, H_{\mathrm{rms}}(r,z) \tag{2.18}$$

The peak field is required by the hysteresis formulation, whereas the rms field is used in the construction of the eddy-current source term. The use of local values of the magnetic field allows the model to capture the non-uniformity of the electromagnetic excitation within the packed bed, which is one of the main limitations of the reference lumped formulation.

The total local heat source applied during charging is defined as the sum of the hysteresis and eddy-current contributions,

$$q_{\mathrm{src}}(r,z,T) = q_{\mathrm{hys}}(r,z,T) + q_{\mathrm{eddy}}(r,z,T) \tag{2.19}$$

The quantity q_{src} is expressed per unit bulk packed-bed volume, i.e. with respect to the total geometrical volume including both the solid and void fractions. The induction heat generation itself occurs only within the magnetite solid phase; the presence of the voids is accounted for through the solid volume fraction $(1-\varepsilon)$ when converting the material-specific heat-generation rate into a volumetric packed-bed sourc. Since the model is developed for an axisymmetric two-dimensional domain, the source is evaluated locally in every computational cell and updated throughout the transient.

The hysteresis contribution is evaluated cell by cell from the local peak magnetic field, the local temperature and the operating frequency. In the implemented formulation, the LangArc model provides the specific hysteresis-heating power of the magnetic material in W kg^{-1}. This quantity is then converted into a volumetric source term by multiplying by the density of the solid phase and by the solid volume fraction of the packed bed. The resulting local hysteresis source term is written as:

$$q_{\mathrm{hys}}(r,z,T) = P_{\mathrm{hys,sp}}\big(H_{\mathrm{peak}}(r,z),T,f\big)\rho_s(1-\varepsilon) \tag{2.20}$$

where $P_{\mathrm{hys,sp}}$ is the specific hysteresis-heating power returned by the LangArc-based formulation, ρ_s is the solid density and is the packed-bed void fraction. This expression implies that the hysteresis contribution varies spatially because both the magnetic field and the temperature vary from cell to cell. In practice, the local field non-uniformity introduces spatial differences in the generated power, while the temperature dependence of the magnetic parameters provides an additional thermal feedback on the source intensity. A practical limitation was identified for the hysteresis formulation at low magnetic-field amplitudes. In particular, when the local peak field

becomes too small, the LangArc-based prediction may show non-physical behaviour. For this reason, the operating conditions used for hysteresis-dominated charging were selected so that the minimum local peak field within the computational domain remained above a threshold of approximately 20 kA m^{-1}. This modelling constraint does not represent a physical operating limit of the storage system, but a precaution required to ensure a reliable use of the hysteresis formulation in the present numerical framework.

The eddy-current contribution requires a different treatment from the hysteresis source. As described in Section 2.1, the reference IH-PBTES model does not resolve the eddy-current distribution inside the packed bed. Instead, it provides a single global eddy-current power for the entire storage volume through the equivalent-resistance formulation,

$$P_{\mathrm{eddy,ref}} = R_{\mathrm{eq}}(f)\, I^2$$

In the reference model, this global power is converted into an average volumetric heat-generation rate by dividing it by the total packed-bed volume. Accordingly, the reference eddy-current source density used as the starting point of the two-dimensional formulation is defined as:

$$\overline{q}_{\mathrm{eddy,ref}} = \frac{P_{\mathrm{eddy,ref}}}{V_{\mathrm{TES}}} = \frac{R_{\mathrm{eq}}(f) I^2}{V_{\mathrm{TES}}}$$

where V_{TES} is the bulk geometrical volume of the packed bed, including both the solid and void fractions. The quantity $\bar{q}_{\mathrm{eddy,ref}}$ therefore represents a single volume-averaged source value rather than a spatially resolved heat-generation field.

The purpose of the two-dimensional extension is not to recalculate the absolute eddy-current power from a local electromagnetic solution, since the microscopic current-density distribution within the individual particles is not resolved. Instead, the global source predicted by the reference model is spatially redistributed over the packed-bed domain. The local rms magnetic-field map calculated by the finite-coil model is used to determine this distribution. Since the present electromagnetic model does not resolve the local eddy-current density within the particles, an additional modelling assumption is required to reconstruct the relative spatial distribution of the eddy-current heat source. In the present implementation, this distribution is assumed to scale with the square of the local rms magnetic-field intensity, consistently with the H_{rms}^2 weighting adopted in the numerical model.

The reconstructed reference eddy-current source is therefore written as:

$$q_{\mathrm{eddy,ref}}(r,z) = \overline{q}_{\mathrm{eddy,ref}} \frac{H_{\mathrm{rms}}^2(r,z)}{\langle H_{\mathrm{rms}}^2 \rangle_V}$$

where $\langle H_{\mathrm{rms}}^2 \rangle_V$ denotes the volume-weighted average of $H_{\mathrm{rms}}^2(r, z)$ over the complete packed-bed domain. The denominator in Eq. (2.22) is therefore a normalisation factor. Its purpose

is to modify only the spatial distribution of the reference eddy-current source without introducing an additional change in its global magnitude. Consequently, regions subjected to a magnetic field higher than the volume-average level receive a larger local eddy-current source, whereas regions exposed to a weaker field receive a smaller contribution.

By construction, the volume average of the reconstructed source is equal to the original reference value, and its integral over the packed-bed volume therefore reproduces the global eddy-current power of the reference model:

$$\langle q_{\mathrm{eddy,ref}} \rangle_V = \overline{q}_{\mathrm{eddy,ref}}, \qquad \int_{V_{\mathrm{TES}}} q_{\mathrm{eddy,ref}}(r,z)\, dV = P_{\mathrm{eddy,ref}}$$

This normalisation is introduced deliberately because the two-dimensional magnetic-field model provides information on where the electromagnetic excitation is stronger or weaker, but it does not independently provide a new absolute eddy-current power law. The absolute reference level is therefore retained from the previously established equivalent model, while the newly calculated magnetic-field map is used only to reconstruct its spatial distribution.

In the numerical implementation, the intermediate weighting function is evaluated as $F(f)H_{\mathrm{rms}}^2(r,z)$, where $F(f)$ is the frequency-dependent power-transmission factor inherited from the reference formulation. However, for a prescribed operating frequency and temperature-independent reference properties, $F(f)$ is spatially uniform. It therefore cancels when the weighting function is divided by its volume average. The spatial redistribution is consequently equivalent to that expressed in Eq. (2.22), while the influence of $F(f)$ on the absolute eddy-current power is already included through $R_{\mathrm{eq}}(f)$ in Eq. (2.21).

The formulation described above defines the reference two-dimensional eddy-current source used as the baseline for the subsequent temperature-dependent correction. Temperature dependence is subsequently introduced as a relative local correction. Rather than replacing the equivalent-resistance formulation with a new absolute eddy-current model, the reconstructed reference source is multiplied by the relative variations of electrical conductivity and effective relative magnetic permeability with respect to a reference temperature T_{ref}. In the implemented model, this correction is written as:

$$q_{\mathrm{eddy}}(r,z,T) = q_{\mathrm{eddy,ref}}(r,z)\,\frac{\sigma(T)}{\sigma(T_{\mathrm{ref}})}\left(\frac{\mu_r(T)}{\mu_r(T_{\mathrm{ref}})}\right)^2$$

In the present implementation, a fixed reference temperature $T_{\mathrm{ref}} = 293.15\mathrm{K}$ is adopted for the relative conductivity and permeability corrections. At $T = T_{\mathrm{ref}}$, both correction ratios are equal to unity and Eq. (2.23) therefore reduces exactly to the spatially reconstructed reference source of Eq. (2.22). As the local packed-bed temperature subsequently evolves, the conductivity

and permeability ratios modify the eddy-current source independently in each computational cell. This temperature-dependent correction is implemented as a relative scaling around the reference state rather than as a new particle-scale electromagnetic solution.

It is important to distinguish the two operations involved in this procedure. The normalisation in Eq. (2.22) preserves the global eddy-current power predicted by the reference model when constructing the baseline two-dimensional spatial distribution. Once the temperature-dependent correction of Eq. (2.23) is applied, however, the local source values, and consequently the total eddy-current power, are allowed to evolve with the thermal state of the packed bed. The model therefore preserves the reference global power only at the reference state, while subsequently introducing thermo-electromagnetic feedback through the temperature-dependent material properties.

In addition to the physically complete source term, the charging framework includes the possibility of activating isolated source modes. This functionality was introduced as a diagnostic tool to clarify the separate thermal and energetic influence of hysteresis and eddy-current heating. Accordingly, the implemented source term can be written in the following general form:

$$q_{\mathrm{src}} = \begin{cases} q_{hys} + q_{eddy}, & \text{total mode} \\ q_{hys}, & \text{hysteresis} - \text{only mode} \\ q_{eddy}, & \text{eddy} - \text{only mode} \end{cases} \tag{2.24}$$

The hysteresis-only and eddy-only modes are not intended to represent two alternative operating strategies. In a real induction-heated packed bed, both hysteresis losses and eddy-current losses would occur simultaneously. Their separate activation in the present work is therefore a modelling choice used exclusively to isolate and analyse the role of each contribution in the temperature distribution, energy balance and charging behaviour of the system. This clarification is important for the correct interpretation of the charging and cyclic results discussed in the following chapters.

At the beginning of the charging phase, the packed bed is assigned an initial temperature field. For the standalone charging simulations presented in this thesis, a spatially uniform initial condition is imposed, namely

$$T(r, z, 0) = T_{\mathrm{init}} \tag{2.25}$$

where T_{init} is the prescribed initial charging temperature. During the transient, the temperature field is updated by the thermal solver, and at every time step the source terms are recalculated from the current thermal state. The charging model therefore operates through a sequential thermo-electromagnetic coupling: the temperature field affects the material properties,

the updated properties modify the local induction source, and the new source distribution drives the subsequent thermal evolution.

From a numerical point of view, the charging algorithm can be summarised as follows. For a given operating condition, the local magnetic-field distribution is first computed over the two-dimensional axisymmetric domain. The initial temperature field is then assigned, and the local hysteresis and eddy-current source terms are evaluated according to the selected source mode. The resulting source term is passed to the transient thermal model, which updates the temperature field over one time step. The thermophysical and electromagnetic properties are then updated from the new temperature, and the source calculation is repeated. This sequence is iterated until the final charging time is reached or, in those simulations where a prescribed energetic or thermal target is imposed, until the relevant stopping criterion is satisfied. The charging model described above constitutes the central component of the numerical framework developed for the induction-heating phase. Its purpose is to translate the non-uniform magnetic excitation generated by the induction coil into a temperature-dependent volumetric heat source acting on the packed bed. The subsequent sections provide the specific modelling ingredients required to complete this framework, namely the calculation of the two-dimensional magnetic-field distribution, the temperature dependence of the relevant material properties, and the formulation of the two-dimensional transient thermal problem and its boundary conditions.

2.3 Two-Dimensional Magnetic Field

The two-dimensional magnetic-field model constitutes the electromagnetic core of the charging framework. Its purpose is to replace the uniform-field assumption adopted in the reference lumped model with a spatially resolved description of the magnetic excitation inside the packed bed. In the real induction-heating configuration, the field generated by the surrounding coil is not uniform, but varies both in the radial and axial directions as a consequence of the finite geometry of the coil and of the relative position of the storage domain. A spatial representation of the magnetic field is therefore required in order to construct local heat-source terms for both hysteresis and eddy-current heating. In the present work, the packed bed is described through an axisymmetric – representation. The computational domain extends from the axis of symmetry to the outer radius of the packed bed, and from the bottom to the top of the storage region. The induction coil is represented as a set of discrete circular turns surrounding the packed bed at a prescribed radial position. This geometrical representation is illustrated in Figure 2.4, which shows the axisymmetric packed-bed domain, the discretised coil and the main geometrical quantities used in the electromagnetic model.

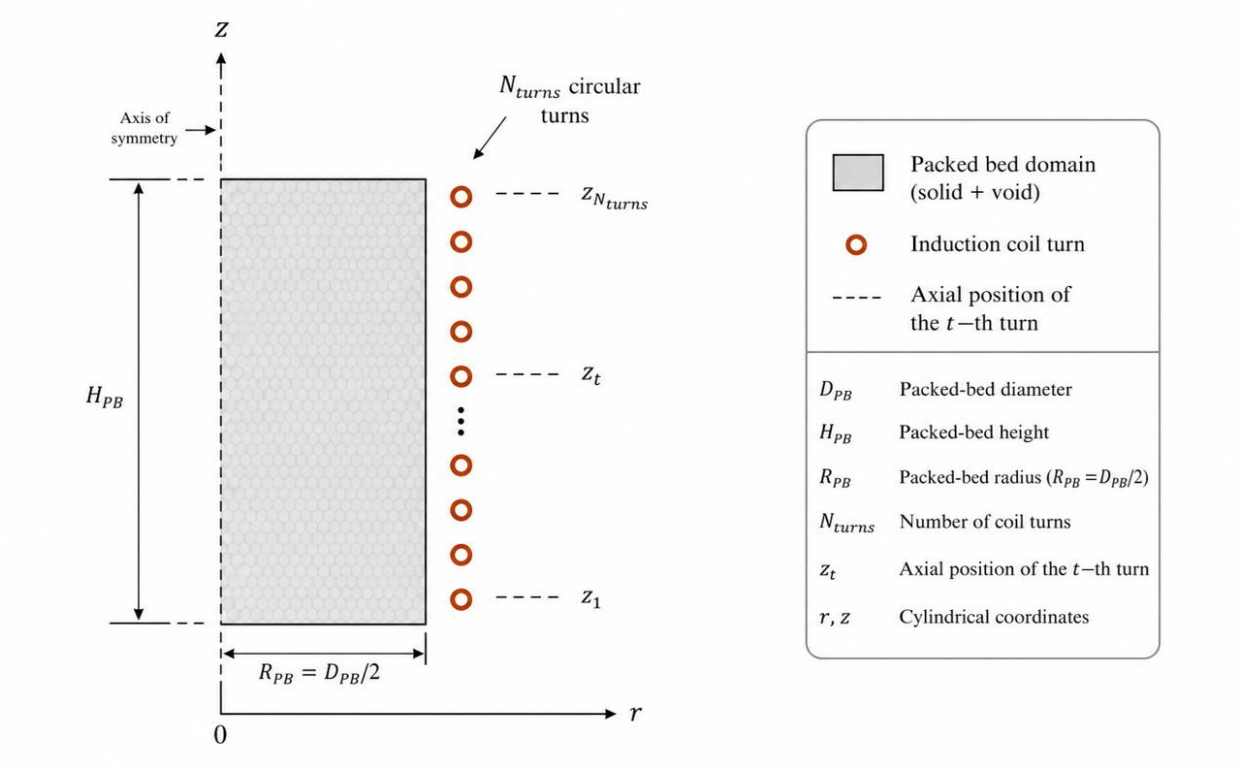


Figure 2.4– Axisymmetric geometrical representation of the packed-bed domain and discretised induction coil used in the two-dimensional magnetic-field model.

The radial position of the coil is represented through its mean radius, defined as

$$a_{\text{coil}} = \frac{D_{\text{coil}}}{2} \tag{2.26}$$

where D_{coil} is the coil diameter. The total number of turns used in the axisymmetric model is denoted by N_{turns}. These turns are distributed along the coil height H_{coil} . For the case with more than one turn, the axial position of the t-th turn is defined as:

$$z_t = \frac{t-1}{N_{\text{turns}}-1} H_{\text{coil}}, \qquad t = 1, \dots, N_{\text{turns}} \tag{2.27}$$

This discretisation provides a simple and effective representation of the actual solenoidal coil while preserving the axisymmetric nature of the model. Once the turn positions are defined, the magnetic field is evaluated by computing the contribution of each circular turn and then summing all the individual contributions through the superposition principle.

The magnetic field generated by a single circular turn is obtained from the Biot–Savart law in cylindrical coordinates. For a turn of radius a, located at axial coordinate z_t and crossed by current I, the relative axial coordinate is first defined as:

$$z_{\text{rel}} = z - z_t \tag{2.28}$$

Along the axis of symmetry, that is for r=0 , the radial component of the magnetic field is zero and the axial component reduces to the well-known analytical expression

$$B_z(0,z) = \frac{\mu_0 I a^2}{2\left(a^2 + z_{\mathrm{rel}}^2\right)^{3/2}} \tag{2.29}$$

For off-axis points, the field is described in terms of the radial and axial components $B_r(r,z)$ and $B_z(r,z)$. In this case, the expressions involve complete elliptic integrals of the first and second kind. The auxiliary quantities used in the formulation are:

$$\alpha^2 = (a+r)^2 + z_{\mathrm{rel}}^2 \tag{2.30}$$

$$\beta^2 = (a-r)^2 + z_{\mathrm{rel}}^2 \tag{2.31}$$

$$k^2 = \frac{4ar}{\alpha^2} \tag{2.32}$$

Using these definitions, the radial component of the magnetic field generated by a single turn can be written as:

$$B_r(r,z) = \frac{\mu_0 I}{2\pi\alpha}\frac{z_{\mathrm{rel}}}{r}\left[-K(k^2) + E(k^2)\frac{a^2 + r^2 + z_{\mathrm{rel}}^2}{\beta^2}\right] \tag{2.33}$$

where $K(k^2)$ and $E(k^2)$ denote the complete elliptic integrals of the first and second kind, respectively. The corresponding axial component is

$$B_z(r,z) = \frac{\mu_0 I}{2\pi\alpha}\left[K(k^2) + E(k^2)\frac{a^2 - r^2 - z_{\mathrm{rel}}^2}{\beta^2}\right] \tag{2.34}$$

These expressions are evaluated for each discrete turn and for each node of the r-z computational grid. Since the magnetic problem is linear with respect to the imposed current, the total field generated by the full coil is obtained by superposition of the contributions of all turns. Accordingly, the total radial and axial components of the magnetic induction are given by

$$B_r^{\mathrm{tot}}(r,z) = \sum_{t=1}^{N_{\mathrm{turns}}} B_{r,t}(r,z) \tag{2.35}$$

$$B_z^{\mathrm{tot}}(r,z) = \sum_{t=1}^{N_{\mathrm{turns}}} B_{z,t}(r,z) \tag{2.36}$$

The magnitude of the total magnetic induction is then computed as

$$B^{\mathrm{tot}}(r,z) = \sqrt{\left(B_r^{\mathrm{tot}}(r,z)\right)^2 + \left(B_z^{\mathrm{tot}}(r,z)\right)^2} \tag{2.37}$$

In the present model, the local rms magnetic-field strength is obtained, as a first approximation, by dividing the magnetic induction by the permeability of free space. This gives

$$H_{\mathrm{rms}}(r,z) = \frac{B^{\mathrm{tot}}(r,z)}{\mu_0} \tag{2.38}$$

This assumption implies that the magnetic field is computed as an equivalent free-space field generated by the imposed coil current. In other words, the model does not solve a fully coupled magnetostatic problem including the detailed electromagnetic feedback of the packed-bed material on the field distribution. The objective of the present electromagnetic model is instead to

provide a consistent local field map that can be used as input for the thermal source formulation developed in the previous section.

Once the rms field has been calculated, the local peak magnetic field is obtained as

$$H_{\mathrm{peak}}(r,z) = \sqrt{2}\, H_{\mathrm{rms}}(r,z) \tag{2.39}$$

The distinction between rms and peak field is important in the present framework. The local peak value $H_{\mathrm{peak}}(r,z)$ is used in the hysteresis-heating model, whereas the local rms field $H_{\mathrm{rms}}(r,z)$ enters the construction of the eddy-current source term. The two-dimensional magnetic-field model therefore provides the electromagnetic link between the coil operating conditions and the local volumetric heat-generation map used in the charging simulations.

In addition to local field values, the model also makes use of a volume-averaged magnetic-field strength. This quantity is especially important in the comparison of different packed-bed aspect ratios, for which the operating current is adjusted so as to preserve the same average magnetic excitation inside the storage domain. In discrete form, the volume-averaged field is calculated as

$$\langle H \rangle_V = \frac{\sum_{i=1}^{N_r} \sum_{j=1}^{N_z} H_{i,j}\, V_{i,j}}{\sum_{i=1}^{N_r} \sum_{j=1}^{N_z} V_{i,j}} \tag{2.40}$$

where $V_{i,j}$ is the axisymmetric volume associated with cell (i,j) . For the present mesh, the cell volume is evaluated as

$$V_{i,j} = 2\pi r_i\, \Delta r\, \Delta z \tag{2.41}$$

The two-dimensional magnetic-field model described above captures the main spatial features of the electromagnetic excitation inside the packed bed, including radial non-uniformities and end effects associated with the finite coil height. At the same time, it remains computationally inexpensive and easily coupled with the thermal solver. Its output is the local field map $\mathrm{H}(r,z)$, from which the source terms for hysteresis and eddy-current heating are subsequently constructed. In this sense, the magnetic-field model represents the key intermediate step between the imposed electrical operating conditions and the spatially distributed heat generation acting within the storage domain.

The following section presents the temperature-dependent material properties introduced in the model, which provide the thermal feedback required to update the local induction source during the charging simulations.

2.4 Temperature-Dependent Material Properties

The spatially resolved thermal formulation introduced in the present work requires the material properties of magnetite to be evaluated locally rather than through constant representative values. Since different regions of the packed bed may reach significantly different temperatures during charging, the use of temperature-independent properties would neglect an important source of thermo-electromagnetic coupling. For this reason, the specific heat capacity, thermal conductivity, electrical conductivity and effective relative magnetic permeability are updated locally as functions of the instantaneous cell temperature.

At each time step, the temperature of every computational cell is used to evaluate the corresponding thermophysical and electromagnetic properties. The resulting values affect both the transient thermal response and the local electromagnetic heat-generation terms. The implemented coupling can therefore be represented schematically as a feedback sequence in which the temperature field determines the material properties, the properties influence the local induction source and thermal diffusion, and the resulting energy balance produces a new temperature field. The four temperature-dependent properties implemented in the numerical framework are shown in Figure 2.5.

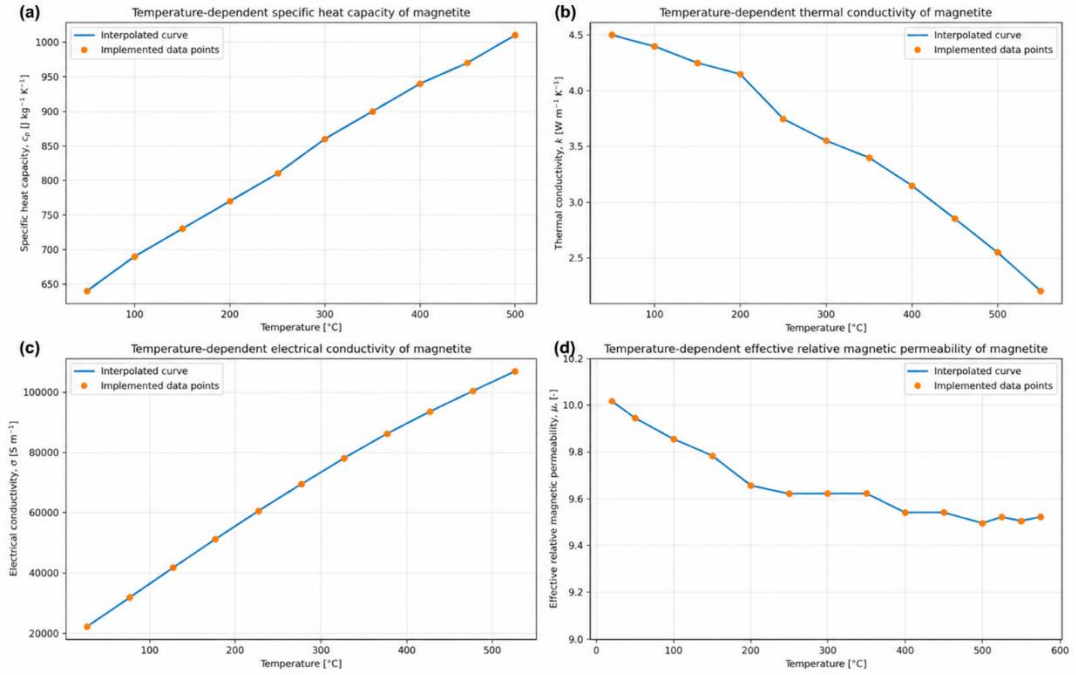


Figure 2.5-Temperature-dependent thermophysical and electromagnetic properties of magnetite implemented in the numerical model: (a) specific heat capacity, (b) thermal conductivity, (c) electrical conductivity, and (d) effective relative magnetic permeability. Thermophysical data are based on [31], [53], electrical conductivity on [50], and magnetic scaling on [46].

The temperature dependence of the specific heat capacity was implemented using experimental data for raw magnetite reported in the literature [31], [53]. In the adopted dataset, the specific heat increases monotonically from approximately 640 J $kg^{-1}K^{-1}$ at 50 °C to

approximately 1010 J $kg^{-1}K^{-1}$ at 500 °C. This trend is consistent with the experimental characterization of raw magnetite reported by Filali Baba et al. [31], who measured a marked increase in specific heat over the same temperature interval, as well as with the independent characterization reported by Grosu et al. [53].

Within the numerical model, the specific heat is evaluated by linear interpolation between the implemented experimental data points. Since the packed bed contains both solid material and void space, the local volumetric heat capacity used in the transient thermal equation is obtained by accounting for the solid volume fraction of the bed. It is therefore expressed as

$$\left(\rho c_p\right)_{\text{eff}}(T) = (1-\varepsilon)\rho_s c_p(T) \tag{2.42}$$

Where ρ_s is the solid density and ε is the packed-bed porosity. The increase in c_p with temperature implies that progressively more energy is required to produce the same local temperature increase as the packed bed becomes hotter. In the transient solver, this effect is therefore directly included in the thermal inertia of each computational cell.

The thermal conductivity of raw magnetite was also introduced as a temperature-dependent property based on the experimental trends reported in [31], [53]. In contrast to the specific heat capacity, the adopted thermal conductivity decreases with increasing temperature. The implemented values vary from approximately 4.5 W $m^{-1}\ K^{-1}$ at 50 °C to approximately 2.2 W $m^{-1}\ K^{-1}$ at 550 °C.

The thermal-conductivity data reported in the cited studies show the same general decreasing trend; Filali Baba et al. [31], in particular, report the raw-magnetite curve directly over approximately 50–550 °C, while Grosu et al. [53] likewise report the dependence of magnetite thermal conductivity on temperature and treatment conditions. At each grid cell, the local value k(T) is used in the conductive term of the two-dimensional thermal equation described in Section 2.5. The decrease in thermal conductivity with temperature reduces the ability of increasingly hot regions to redistribute locally generated heat by conduction. This temperature dependence is therefore relevant to the development of spatial thermal gradients, although its actual effect on the temperature distributions obtained during charging is analysed in the Results chapter.

The electrical conductivity of magnetite plays a direct role in the equivalent eddy-current formulation. Its temperature dependence was derived from the electrical-resistivity measurements reported by Botrous El Badramany et al. [50]. The original experimental data are expressed as electrical resistivity in $\Omega\ cm$ over the range 300–800 K. These values are first converted to SI units according to

$$\rho_e[\Omega\,\mathrm{m}] = 10^{-2}\rho_e[\Omega\,\mathrm{cm}] \tag{2.43}$$

The corresponding electrical conductivity is subsequently calculated as the reciprocal of the resistivity,

$$\sigma(T) = \frac{1}{\rho_e(T)} \tag{2.44}$$

The implemented curve exhibits a strong increase in electrical conductivity with temperature. Over the available experimental range, the conductivity rises from approximately $2.2*10^4$ S m^{-1} at 300 K to approximately $1.07*10^5$ S m^{-1} at 800 K. This variation is substantially larger, in relative terms, than the temperature variation of the effective magnetic permeability introduced below.

The strong temperature sensitivity of electrical conductivity is particularly relevant to the eddy-current heat-generation model. As introduced in Section 2.2, the temperature-dependent eddy-current source is scaled through the ratio between the local conductivity and its reference value. Consequently, a local increase in temperature modifies the electrical response of the magnetite and may reinforce the corresponding eddy-current source. This constitutes a potential positive thermo-electromagnetic feedback: a hotter region may become more electrically conductive, which modifies the local eddy-current heating and can further affect its temperature. The actual influence of this mechanism on the spatial temperature distribution is evaluated in the Results chapter.

The temperature dependence of magnetic permeability requires particular care because the available experimental data do not directly provide an absolute relative permeability for centimetric magnetite pebbles. Therefore, the measurements reported by Dunlop [46] were not used as absolute values of μ_r. Instead, the temperature evolution of the initial magnetic susceptibility measured for the 110 µm magnetite fraction was employed only as a relative thermal scaling function.

The scaling factor is defined from the initial susceptibility k_0 as

$$f_\mu(T) = \frac{k_0(T)}{k_0(T_{\mathrm{ref}})} \tag{2.45}$$

where the reference temperature is approximately 20 °C. The digitised experimental curve is therefore used to reproduce only the relative variation of magnetic susceptibility with temperature. The absolute electromagnetic reference value remains that adopted in the original IH-PBTES model, namely

$$\chi_{\mathrm{ref}} = \mu_{r,\mathrm{ref}} - 1 \tag{2.46}$$

with an adopted reference relative permeability of $\mu_{r,\mathrm{ref}} = 10$. The effective temperature-dependent relative permeability is then calculated as

$$\mu_r(T) = 1 + \chi_{\mathrm{ref}} f_\mu(T) \tag{2.47}$$

This procedure preserves the absolute reference value used in the baseline electromagnetic model while introducing the relative temperature trend observed experimentally. As shown in Figure 2.5(d), the resulting effective relative permeability varies only moderately over the investigated temperature interval, decreasing from approximately 10 at room temperature to approximately 9.5 at the highest temperatures considered. The small local variations visible in the curve at high temperature originate from the discrete experimental susceptibility data used to construct the scaling and should not be interpreted as large physical oscillations of the permeability.

It should also be emphasised that the temperature-dependent effective permeability introduced here does not replace the temperature-dependent parameters used in the LangArc hysteresis model. In the present implementation, the effective $\mu_r(T)$ described in this section is primarily used in the eddy-current correction and in derived electromagnetic quantities, whereas the temperature dependence of hysteresis is treated independently through the LangArc parameters introduced previously.

Electrical conductivity and magnetic permeability jointly determine the electromagnetic penetration depth inside the magnetite particles. The corresponding temperature-dependent skin depth is evaluated as

$$\delta(T, f) = \sqrt{\frac{2}{\omega \mu_0 \mu_r(T) \sigma(T)}} \tag{2.48}$$

Where $\omega = 2\pi f$, f is the excitation frequency and μ_0 is the magnetic permeability of free space. The skin depth therefore changes with both operating frequency and local material temperature. Nevertheless, as discussed in Section 2.2, the present model does not resolve the microscopic current-density distribution inside each pebble. The skin-depth calculation remains part of the equivalent eddy-current formulation and should not be interpreted as a particle-scale electromagnetic solution.

All temperature-dependent properties are implemented from discrete data points. Between two consecutive experimental temperatures, the property value is obtained through linear interpolation. For a generic material property X, the interpolation between two adjacent tabulated points can be expressed as

$$X(T) = X_i + \frac{X_{i+1} - X_i}{T_{i+1} - T_i}(T - T_i) \tag{2.49}$$

No uncontrolled extrapolation is performed outside the available temperature ranges. Instead, the temperature supplied to each property correlation is clipped to the nearest boundary

of the corresponding dataset. Consequently, $c_p(T)$ is evaluated over 50–500 °C, $k(T)$over 50–550 °C, $\sigma(T)$ over 300–800 K, and the magnetic susceptibility scaling used for $\mu_r(T)$ over approximately 20–575 °C. Below or above these intervals, the corresponding boundary value is retained.

This approach improves numerical robustness and avoids extrapolating experimental correlations beyond their validated ranges, but it also represents a modelling limitation. In particular, the magnetic transition of magnetite reported in the literature approximately 570–585 °C, depending on the considered dataset and material characteristics, is not explicitly represented as a latent-heat contribution in the present sensible-heat formulation [53]. The implemented thermophysical correlations reproduce the selected temperature-dependent trends used in the numerical model, while property values above their respective upper limits remain fixed at the last available value.

Property	Symbol	Implemented range	Numerical treatment	Source
Specific heat capacity	$c_p(T)$	50–500 °C	Linear interpolation + clipping	[31], [53]
Thermal conductivity	$k(T)$	50–550 °C	Linear interpolation + clipping	[31], [53]
Electrical conductivity	$\sigma(T)$	300–800 K	Interpolated resistivity, then inversion + clipping	[50]
Effective relative magnetic permeability	$\mu_r(T)$	20–575 °C	Relative susceptibility scaling + clipping	[46]

Table 2.2– Temperature-dependent magnetite properties implemented in the numerical model and corresponding literature sources.

The combined implementation of these properties provides the temperature feedback required by the two-dimensional charging framework. The thermophysical properties $c_p(T)$ and $k(T)$ determine the local thermal inertia and conductive redistribution of heat, whereas $\sigma(T)$ and $\mu_r(T)$ influence the equivalent eddy-current response. Among the electromagnetic properties, the conductivity exhibits by far the strongest relative variation over the implemented temperature range, while the effective relative permeability changes comparatively little. The resulting interaction between spatially non-uniform induction heating and temperature-dependent material behaviour is naturally captured by updating all relevant properties at every time step and in every computational cell.

Having defined the temperature-dependent properties required by the model, the following section presents the two-dimensional transient thermal formulation used to determine the evolution of the packed-bed temperature field during induction charging.

2.5 Two-Dimensional Transient Heat-Conduction Model

The internal thermal response of the packed bed during induction charging is described through a two-dimensional transient heat-conduction formulation with spatially distributed volumetric heat generation. Packed-bed thermal storage systems are commonly represented at the macroscopic scale as porous continuous media rather than by explicitly resolving each individual particle and particle-to-particle contact [18], [31]. Following this approach, the present model represents the magnetite packed bed as an equivalent axisymmetric thermal domain in which the locally generated induction heat is redistributed by conduction.

Individual magnetite pebbles are not geometrically resolved. Consequently, the model does not explicitly calculate thermal contact resistances between adjacent particles, conduction through the gas contained in the void space, or inter-particle radiative heat transfer. Instead, the temperature-dependent thermal conductivity of raw magnetite introduced in Section 2.4 is directly assigned as the conductivity coefficient of the equivalent continuous domain. This represents a modelling simplification and should not be interpreted as a dedicated effective-conductivity correlation for the packed bed.

The thermal inertia of the bed is instead corrected for the solid fraction. As defined in Eq. (2.42), the effective volumetric heat capacity is obtained from the local specific heat of magnetite and the solid volume fraction $1 - \varepsilon$. The thermal capacity of the gas occupying the void fraction is neglected during charging, since no heat-transfer fluid is circulated through the packed bed in this phase. The resulting thermal formulation therefore describes the transient sensible heating of the solid storage medium under a spatially distributed internal heat source.

For an axisymmetric domain with no dependence on the azimuthal coordinate, the local temperature field is governed by the transient heat-conduction equation with volumetric heat generation. Using the local-property approximation implemented in the numerical solver, the governing equation is written as

$$\left(\rho c_p\right)_{\text{eff}}(T)\frac{\partial T}{\partial t} = k(T)\left[\frac{\partial^2 T}{\partial r^2} + \frac{1}{r}\frac{\partial T}{\partial r} + \frac{\partial^2 T}{\partial z^2}\right] + q_{\text{src}}(r, z, T) \tag{2.50}$$

The left-hand side of Eq. (2.50) represents the local sensible-energy accumulation within the packed bed. The first term on the right-hand side describes heat redistribution by conduction

in the radial and axial directions, while $q_{\mathrm{src}}(r, z, T)$ represents the local volumetric heat source generated by electromagnetic induction, as described in Section 2.2. Transient thermal formulations combining internal volumetric heat generation and conduction are widely used in electrothermal modelling [36], while macroscopic energy equations are also extensively employed for packed-bed thermal storage systems [18], [31].

It is important to note that Eq. (2.50) reflects the specific numerical approximation adopted in this work. The temperature-dependent thermal conductivity of raw magnetite, $k_s(T)$, evaluated at the local cell temperature, is used directly as the conduction coefficient of the equivalent continuum domain and multiplies the Laplacian of the temperature field. As noted above, this coefficient represents the intrinsic conductivity of the solid material rather than an effective packed-bed conductivity accounting for inter-particle contacts and heat transfer through the void space. The solver therefore does not discretise the more general conservative form $\nabla\cdot[\, k(T)\nabla \mathrm{T}]$, which would additionally account for spatial gradients of the conductivity itself. Instead, $k(T)$ is evaluated locally at each cell temperature and applied to the discrete temperature Laplacian. This approximation preserves the temperature dependence of the conductivity while retaining a relatively simple explicit thermal solver.

The thermal domain coincides with the axisymmetric packed-bed domain introduced in Section 2.3. The radial coordinate extends from the symmetry axis to the packed-bed radius, whereas the axial coordinate extends from the bottom to the top of the storage volume. The computational domain is therefore defined by

$$0 \le r \le R_{PB}, \qquad 0 \le z \le H_{PB} \tag{2.51}$$

The domain is discretised using N_r radial nodes and N_z axial nodes. The corresponding uniform grid spacings are:

$$\Delta r = \frac{R_{PB}}{N_r - 1} \tag{2.52}$$

$$\Delta z = \frac{H_{PB}}{N_z - 1} \tag{2.53}$$

The geometrical and numerical parameters adopted for the two-dimensional simulations are summarised in Table 2.3. For the baseline packed-bed configuration, $D_{PB} = 0.86$ m and $H_{PB} = 1.72$ m, corresponding to an aspect ratio $AR = 2$, while the pebble diameter is $D_p = 0.020$ m. The final temperature-dependent two-dimensional simulations are performed using $N_r = 20$ radial nodes and $N_z = 40$ axial nodes. According to Eqs. (2.52) and (2.53), this corresponds to uniform grid spacings of $\Delta r = 2.26 \times 10^{-2}$m and $\Delta z = 4.41 \times 10^{-2}$m. A time step of $\Delta t_{\mathrm{ch}} = 10$ s is

adopted for the charging calculations. The preliminary uniform-source validation presented in Section 3.1 was performed using a 40×80 grid and the same charging time step.

Parameter	**Symbol**	**Value**
Packed-bed diameter	D_{PB}	0.86 m
Packed-bed height	H_{PB}	1.72 m
Packed-bed aspect ratio	AR	2
Pebble diameter	D_P	0.020 m
Radial nodes, final 2D simulations	N_r	20
Axial nodes, final 2D simulations	N_z	40
Radial grid spacing	Δr	0.0226 m
Axial grid spacing	Δz	0.0441 m
Charging time step	Δt	10 s
Discharging time step	Δt_{dis}	5 s
Validation grid	$N_z * N_r$	40 × 80

Table 2.3– Geometrical and numerical parameters adopted in the two-dimensional simulations.

The 20×40 discretisation is used consistently throughout the final temperature-dependent analyses. A systematic grid- and time-step-independence study was not performed within the scope of the present work and is therefore retained as a limitation of the numerical analysis.

Each node (i,j) is associated with a local temperature $T_{i,j}$. At every time step, the temperature-dependent specific heat and thermal conductivity are evaluated from the current value of $T_{i,j}$, while the induction model provides the corresponding local heat-generation term $q_{src,i,j}$. The model therefore allows neighbouring regions of the packed bed to evolve differently according to both the imposed non-uniform electromagnetic source and the conductive exchange with the surrounding cells.

The spatial derivatives in Eq. (2.50) are approximated using finite differences. For an internal node, the second-order axial derivative is evaluated using a central difference,

$$\left(\frac{\partial^2 T}{\partial z^2}\right)_{i,j} \approx \frac{T_{i,j+1} - 2T_{i,j} + T_{i,j-1}}{\Delta z^2} \tag{2.54}$$

The corresponding second-order radial derivative is

$$\left(\frac{\partial^2 T}{\partial r^2}\right)_{i,j} \approx \frac{T_{i+1,j} - 2T_{i,j} + T_{i-1,j}}{\Delta r^2} \tag{2.55}$$

while the first-order radial derivative appearing in the axisymmetric term is approximated as

$$\left(\frac{\partial T}{\partial r}\right)_{i,j} \approx \frac{T_{i+1,j} - T_{i-1,j}}{2\Delta r} \tag{2.56}$$

For an internal node located away from the symmetry axis and the external boundaries, the complete discrete axisymmetric Laplacian is therefore expressed as

$$(\nabla^2 T)_{i,j} \approx \frac{T_{i+1,j} - 2T_{i,j} + T_{i-1,j}}{\Delta r^2} + \frac{1}{r_i}\frac{T_{i+1,j} - T_{i-1,j}}{2\Delta r} + \frac{T_{i,j+1} - 2T_{i,j} + T_{i,j-1}}{\Delta z^2} \tag{2.57}$$

This formulation enables heat generated in one region of the packed bed to be redistributed to neighbouring regions during the charging transient. However, this redistribution represents heat diffusion through the equivalent continuum rather than a resolved particle-scale description of pebble-to-pebble heat transfer. The actual thermal contacts between individual pebbles and the detailed geometry of the void space are therefore not explicitly represented.

Special treatment is required at the axis of symmetry because the cylindrical-coordinate operator contains the term $r^{-1}\frac{\partial T}{\partial r}$, which appears singular at $r = 0$. Axisymmetry imposes a zero radial temperature gradient at the centreline,

$$\left(\frac{\partial T}{\partial r}\right)_{r=0} = 0 \tag{2.58}$$

Using the limiting form of the cylindrical heat operator together with the symmetry condition, the radial contribution at the first radial node is discretised in the model as

$$\left(\frac{\partial^2 T}{\partial r^2} + \frac{1}{r}\frac{\partial T}{\partial r}\right)_{r=0,j} \approx \frac{4\left(T_{1,j} - T_{0,j}\right)}{\Delta r^2} \tag{2.59}$$

This treatment avoids the mathematical singularity at the axis while preserving the symmetry of the physical problem. It is implemented directly in the thermal solver before the axial contribution is added to obtain the complete local Laplacian.

The transient temperature equation is advanced in time using an explicit finite-difference scheme. For each computational cell, the volumetric heat capacity, thermal conductivity and induction source are first evaluated from the temperature field at the current time level n. The new temperature is then calculated according to

$$T_{i,j}^{n+1} = T_{i,j}^{n} + \frac{\Delta t}{\left(\rho c_p\right)_{\mathrm{eff},i,j}^{n}}\left[k_{i,j}^{n}(\nabla^2 T)_{i,j}^{n} + q_{\mathrm{src},i,j}^{n}\right] \tag{2.60}$$

After all cells have been updated, the new temperature field replaces the previous one and is used to recalculate the local material properties and electromagnetic heat source for the following time step. The numerical algorithm consequently reproduces the sequential thermo-electromagnetic feedback introduced in Section 2.2. This explicit update is also retained in the later cyclic simulations, ensuring that the same thermal formulation is used consistently throughout the charging analyses.

Because an explicit time-integration scheme is employed, the time step must be restricted in relation to the spatial resolution and thermal diffusivity. The local thermal diffusivity associated with the implemented continuum model is defined as

$$\alpha(T) = \frac{k(T)}{\left(\rho c_p\right)_{\text{eff}}(T)} \tag{2.61}$$

Before the transient calculation, the numerical implementation evaluates the maximum thermal diffusivity associated with the reference temperature field and estimates the explicit stability limit as

$$\Delta t_{\text{lim}} = \frac{1}{2\alpha_{\max}\left(\frac{1}{\Delta r^2} + \frac{1}{\Delta z^2}\right)} \tag{2.62}$$

A conservative warning criterion is then applied: if the selected time step exceeds 80% of this estimated limit, the solver reports that a smaller value should be adopted. The practical criterion used in the simulations is therefore

$$\Delta t \leq 0.8\Delta t_{\text{lim}} \tag{2.63}$$

The stability estimate is evaluated using the temperature-dependent conductivity and heat capacity introduced in Section 2.4. This check is particularly relevant because explicit finite-difference algorithms may become unstable when the temporal resolution is too coarse relative to the spatial mesh and thermal diffusivity. The implemented expression and the additional safety margin were therefore used to verify the suitability of the selected time step before the transient calculations.

In addition to the complete two-dimensional temperature field, several global quantities are evaluated during each charging simulation. The mean packed-bed temperature is obtained through an axisymmetric volume-weighted average,

$$T_{\text{mean}}(t) = \frac{\sum_{i=1}^{N_r}\sum_{j=1}^{N_z} T_{i,j}\,(t)\Delta V_{i,j}}{\sum_{i=1}^{N_r}\sum_{j=1}^{N_z} \Delta\, V_{i,j}} \tag{2.64}$$

where $\Delta V_{i,j}$ denotes the axisymmetric volume associated with each computational grid location. In the discrete implementation, this volume is evaluated as

$$\Delta V_{i,j} = 2\pi r_i^{\text{eff}} \Delta r \Delta z$$

where $r_i^{\text{eff}} = r_i$ away from the symmetry axis, while $r_i^{\text{eff}} = \Delta r/2$i s used at $r = 0$. This treatment assigns a finite volume to the central region and avoids assigning zero weight to the cells located on the symmetry axis.

The model also stores the maximum packed-bed temperature, the volume-averaged and maximum induction-source densities, and selected snapshots of the complete temperature field.

These quantities provide the basis for the spatial and temporal analyses presented in the Results chapter.

The resulting thermal formulation represents an intermediate level of complexity between the lumped model described in Section 2.1 and a fully resolved particle-scale simulation. Its principal advantage is the ability to predict radial and axial temperature gradients and local temperature maxima at a computational cost compatible with transient parametric and cyclic analyses. At the same time, the continuum approximation introduces several limitations. Individual pebble temperatures and contact resistances are not resolved, the thermal effect of the gas contained in the void fraction is neglected during charging, and the raw-magnetite thermal conductivity is used directly as the continuum conduction coefficient rather than through a dedicated effective packed-bed conductivity correlation.

Furthermore, radiative heat exchange between individual particles is not modelled explicitly. These simplifications mean that the predicted internal heat redistribution should be interpreted at the macroscopic packed-bed scale. Nevertheless, the formulation retains the principal effects required for the objectives of the present work: spatially non-uniform induction heating, transient conductive redistribution, temperature-dependent thermal properties and the development of a two-dimensional temperature field.

The treatment described in this section applies to the internal thermal evolution of the packed bed. Heat exchange with the external environment requires a separate treatment of the lateral, upper and lower boundaries of the storage domain. The equivalent thermal resistances, heat-transfer coefficients and ghost-node boundary formulations used to represent these losses are presented in Section 2.6.

2.6 Heat Losses and Boundary Conditions

Heat losses to the surroundings are included in the two-dimensional thermal model through local boundary conditions applied to the lateral, upper and lower surfaces of the packed bed. This represents an important extension with respect to the reference lumped formulation described in Section 2.1, in which the entire storage unit is characterised by a single representative temperature and the ambient heat loss is evaluated as a global power term. In the spatially resolved model, the temperatures of the boundary cells evolve independently, so that different portions of the storage surface may exchange different amounts of heat with the environment.

Thermal losses through the walls of packed-bed storage systems can significantly influence their overall energy balance, particularly at high operating temperatures and during extended storage periods [18], [54]. Calderón-Vásquez and Cardemil [54], for example, distinguish the

thermal losses occurring through the lateral, top and bottom surfaces of PBTES systems and represent the thermal path through the storage envelope by means of equivalent thermal resistances. A similar resistance-based approach is adopted in the present work, while retaining the simplified loss formulation inherited from the reference IH-PBTES model [52]. Cylindrical thermal-resistance formulations for insulated systems are also well established in heat-transfer modelling [36].

At each external boundary, heat transfer from the packed bed towards the ambient is represented through an equivalent convective boundary condition. In general form, the outward conductive heat flux at the storage boundary is balanced by an equivalent heat-transfer term according to

$$-k(T)\frac{\partial T}{\partial n} = h_{\mathrm{eq}}(T_s - T_{\mathrm{amb}}) \tag{2.65}$$

In Eq. (2.65), T_s denotes the local packed-bed boundary temperature, T_{amb} is the prescribed ambient temperature and h_{eq} is an equivalent heat-transfer coefficient that combines conduction through the external insulation and convection from its outer surface to the surrounding air. The use of the local boundary temperature is important because the two-dimensional model may develop substantial spatial temperature differences during charging.

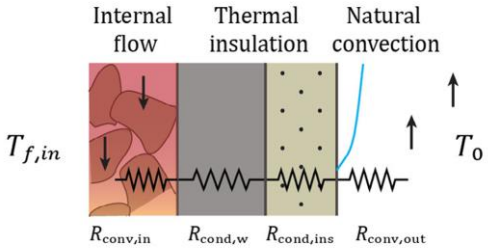


Table 2.3– Schematic representation of the thermal-loss model through the lateral surface of an axial-flow packed-bed thermal energy storage system. Adapted from [54].

For the cylindrical lateral surface, the equivalent heat-transfer coefficient is derived from the same thermal-resistance structure used for the ambient-loss term of the reference model [52]. In the inherited numerical implementation used as the starting point of the present work, the thermal conductivity of the rock-wool insulation is represented by the following temperature-dependent linear relation:

$$k_{\mathrm{ins}}(T_{\mathrm{ref}}) = 0.035 + 10^{-4}(T_{\mathrm{ref}} - 300) \tag{2.66}$$

where T_{ref} is expressed in K and the resulting k_{ins} in $\mathrm{W}m^{-1}K^{-1}$. This temperature-dependent correlation was already implemented in the inherited reference code and is retained unchanged in the present work. It should be noted that Ref. [52] reports instead a constant

insulation thermal conductivity of $k_{\mathrm{ins}} = 0.062\mathrm{W}m^{-1}K^{-1}$. Therefore, Eq. (2.66) represents an implementation-specific relation inherited from the original numerical code rather than a correlation taken directly from Ref. [52]. Unless a different value is explicitly supplied to the solver, the initial packed-bed temperature is used as T_{ref}. An external convective heat-transfer coefficient of $h_{\mathrm{ext}} = 10\mathrm{W}m^{-2}K^{-1}$ is prescribed, consistently with the reference model [52]. These parameters are used to determine the equivalent heat-transfer coefficients before the transient integration begins.

The outer diameter of the insulation layer is defined as

$$D_{\mathrm{eff}} = D_{PB} + 2e_{\mathrm{ins}} \tag{2.67}$$

Where e_{ins} is the insulation thickness. The radial conductive resistance through the cylindrical insulation layer is then expressed as

$$R_{\mathrm{cond,side}} = \frac{\ln(D_{\mathrm{eff}}/D_{PB})}{2\pi k_{\mathrm{ins}} H_{PB}} \tag{2.68}$$

The corresponding external convective resistance is

$$R_{\mathrm{conv,side}} = \frac{1}{h_{\mathrm{ext}}\pi D_{\mathrm{eff}} H_{PB}} \tag{2.69}$$

The two resistances are assumed to act in series, giving the total lateral thermal resistance

$$R_{\mathrm{tot,side}} = R_{\mathrm{cond,side}} + R_{\mathrm{conv,side}} \tag{2.70}$$

In the reference lumped model, this resistance is used directly to determine the total ambient-loss power from the representative packed-bed temperature. In the two-dimensional formulation, the same global resistance is converted into an equivalent heat-transfer coefficient referred to the internal lateral surface of the packed bed. Since the internal lateral area is $\pi D_{PB} H_{PB}$, the coefficient used in the local boundary condition is

$$h_{\mathrm{eq,side}} = \frac{1}{\pi D_{PB} H_{PB} R_{\mathrm{tot,side}}} \tag{2.71}$$

This transformation preserves the thermal-resistance structure of the original ambient-loss model while allowing the loss term to depend on the local temperature of the external radial boundary. Consequently, regions of the lateral surface that reach higher temperatures exchange more heat with the surroundings than colder regions, even though the equivalent heat-transfer coefficient itself remains fixed during an individual charging simulation. The code evaluates $h_{\mathrm{eq,side}}$ before the transient time loop using the selected reference temperature.

Heat losses through the upper and lower surfaces are treated separately because the heat-flow path through the insulation is approximated as one-dimensional and planar rather than cylindrical. The area-specific thermal resistance is therefore written as

$$R''_{\mathrm{tot,tb}} = \frac{e_{\mathrm{ins}}}{k_{\mathrm{ins}}} + \frac{1}{h_{\mathrm{ext}}} \tag{2.72}$$

where the first contribution represents conduction across the insulation and the second represents convection from its external surface to the ambient. The corresponding equivalent heat-transfer coefficient for the top and bottom surfaces is

$$h_{\mathrm{eq,tb}} = \frac{1}{R''_{\mathrm{tot,tb}}} \tag{2.73}$$

The same insulation conductivity and external convection coefficient used for the lateral surface are adopted. However, the distinction between $h_{\mathrm{eq,side}}$ and $h_{\mathrm{eq,tb}}$ is retained because the thermal-resistance geometry differs between the cylindrical side wall and the planar end surfaces. The final thermal implementation therefore allows heat losses through all three exposed regions of the axisymmetric storage domain rather than restricting losses to the lateral surface alone. The final code implements exactly this separate side and top/bottom treatment.

The boundary conditions are incorporated into the finite-difference thermal solver through ghost nodes positioned immediately outside the computational domain. This approach allows the same central-difference operators introduced in Section 2.5 to be retained at the physical boundaries while enforcing the required heat flux towards the surroundings.

At the external radial boundary r=R_{PB} , the boundary temperature corresponds to node $i = N_r - 1$. Applying Eq. (2.65) and approximating the radial derivative through a centred difference involving an external ghost node gives the ghost temperature

$$T_{\mathrm{ghost},r} = T_{i-1,j} - 2\Delta r \frac{h_{\mathrm{eq,side}}}{k_{i,j}} \left(T_{i,j} - T_{\mathrm{amb}}\right) \tag{2.74}$$

The local packed-bed conductivity $k_{i,j} = \mathrm{k}(T_{i,j})$ is used in the boundary expression, consistently with the temperature-dependent thermal model described in Sections 2.4 and 2.5. The resulting ghost-node temperature is then inserted into both the first- and second-order radial finite-difference terms used to evaluate the axisymmetric heat-conduction operator at the external wall. This is the exact procedure implemented in the final solver.

At the lower boundary z=0, the node immediately inside the domain is $T_{i,1}$, whereas the ghost node lies below the packed bed. Application of the top-and-bottom equivalent coefficient gives

$$T_{\mathrm{ghost,bot}} = T_{i,1} - 2\Delta z \frac{h_{\mathrm{eq,tb}}}{k_{i,0}} \left(T_{i,0} - T_{\mathrm{amb}}\right) \tag{2.75}$$

This ghost value is subsequently used as the lower neighbouring temperature in the second-order axial derivative. The formulation therefore produces an outward heat flux whenever the local bottom-surface temperature exceeds the ambient temperature.

An analogous treatment is applied at the upper boundary z=H_{PB} . In this case, the internal neighbouring node is T_{i,N_z-2}, while the external ghost node is defined as

$$T_{\text{ghost,top}} = T_{i,N_z-2} - 2\Delta z \frac{h_{\text{eq,tb}}}{k_{i,N_z-1}} \left(T_{i,N_z-1} - T_{\text{amb}}\right) \tag{2.76}$$

The bottom and top boundaries therefore use the same equivalent heat-transfer coefficient but different local boundary temperatures. This preserves the spatially resolved character of the model and allows the two end surfaces to exhibit different instantaneous heat-loss rates if the axial temperature field becomes asymmetric. The corresponding expressions are implemented explicitly in the final thermal solver. It should be noted that axial heat losses through the top and bottom boundaries are included through the equivalent boundary conditions described above. However, axial heat conduction within the vessel wall itself is not explicitly resolved, since the tank structure is not represented as a separate solid computational domain. Its thermal effect is therefore accounted for only through the equivalent boundary heat-transfer formulation.

The remaining radial boundary corresponds to the symmetry axis at r=0 . No heat flux crosses this axis because it is not a physical external surface. The zero-gradient symmetry condition introduced in Eq. (2.58) is therefore retained,

$$\left(\frac{\partial T}{\partial r}\right)_{r=0} = 0$$

No new equation number is required here because this condition has already been defined in Section 2.5. Its numerical implementation through the special cylindrical-axis stencil given by Eq. (2.59) remains unchanged.

A distinction must be made between the quantities that vary dynamically during the simulation and those that remain fixed. The local packed-bed conductivity appearing in the ghost-node expressions is recalculated at every time step from the current boundary-cell temperature. Similarly, the temperature difference driving each heat loss changes continuously because the boundary temperatures evolve during charging. By contrast, the equivalent coefficients $h_{\text{eq,side}}$ and $h_{\text{eq,tb}}$ are calculated once before the transient simulation using the reference temperature T_{ref} and are then retained throughout that charging calculation. This implementation follows directly from the final numerical code.

Consequently, the model captures the principal effect of spatially and temporally varying boundary temperatures while avoiding the additional numerical complexity that would arise from

recalculating the insulation and external convection resistances at every time step. This approach also maintains continuity with the ambient-loss formulation inherited from the reference model [52].

The adopted heat-loss formulation is intentionally simplified. The insulation layer is not represented as an independent transient thermal domain, and its internal temperature distribution and thermal inertia are therefore not resolved. Similarly, the external convection coefficient is prescribed as a constant value rather than being recalculated from a temperature-dependent natural-convection correlation. More detailed PBTES models may determine external convection through Nusselt and Rayleigh correlations and explicitly distinguish different heat-transfer mechanisms at each storage surface [54]. In the present model, these effects are condensed into the equivalent coefficients defined above. Calderón-Vásquez and Cardemil, for example, explicitly evaluate natural convection at the outer storage surfaces through Nusselt-number correlations, which illustrates the higher level of detail possible in a full enclosure model.

Radiative heat exchange between the external storage surface and the surroundings is also not introduced as an independent boundary term. In addition, the thermal resistance and transient thermal inertia of the refractory vessel are not resolved separately in the two-dimensional charging formulation; the adopted boundary coefficients retain the simplified insulation-plus-external-convection structure of the inherited ambient-loss model. These assumptions should be considered when interpreting the absolute magnitude of predicted environmental heat losses, particularly at the highest operating temperatures.

Despite these simplifications, the local boundary formulation represents a significant improvement over the lumped ambient-loss treatment of the reference model. The thermal solver no longer uses a single average packed-bed temperature to determine the heat transferred to the environment. Instead, each external region exchanges heat according to its local thermal state, allowing non-uniform magnetic heating, conductive redistribution and surface losses to interact within the same two-dimensional transient framework.

With the charging-phase thermal formulation fully defined, including internal heat diffusion, temperature-dependent properties and environmental heat losses, the model can determine the complete temperature field reached at the end of charging. This two-dimensional thermal state provides the initial condition for the subsequent discharge process, during which the stored sensible energy is extracted by a flowing air stream. The discharge formulation is described in Section 2.7.

2.7 Discharging Model

The discharging model was developed to extend the IH-PBTES framework beyond the induction-charging phase and to quantify the useful thermal energy that can subsequently be recovered from the storage medium. At the end of charging, the packed bed is characterised by a two-dimensional solid-temperature distribution rather than by a single representative temperature. This final charging map is therefore directly transferred to the discharge model and used as the initial thermal state of the storage medium. During discharge, the induction source is deactivated and ambient air is introduced through the void fraction of the bed, where it extracts sensible heat from the magnetite particles before leaving the storage system at an increased temperature.

The thermal behaviour during discharge is described through a two-temperature formulation in which the solid and fluid phases are allowed to have different local temperatures. Such non-local-thermal-equilibrium approaches are widely adopted for packed-bed thermal storage because finite heat-transfer coefficients prevent the solid and the heat-transfer fluid from remaining at the same temperature during transient operation [18], [31], [54]. In the present model, however, the complete transient fluid energy equation is not solved. Instead, the solid retains its two-dimensional transient representation, while the air is propagated sequentially through the storage domain using a local cell-by-cell Number of Transfer Units (NTU) formulation. This provides a computationally efficient means of coupling the evolving solid-temperature field with the temperature rise of the flowing air.

Unlike the conventional single-direction axial-flow configuration commonly adopted in packed-bed thermocline systems, the discharge arrangement considered in the present work is symmetric with respect to the central axial plane. This choice is consistent with the symmetry of the charging problem, for which the electromagnetic excitation, initial thermal condition and end-boundary conditions generate a temperature field that is symmetric about the bed mid-plane. The two halves of the storage volume are therefore treated as equivalent thermal domains and are discharged in parallel: the imposed total air flow is introduced simultaneously from the two physical ends of the packed bed and directed towards a common outlet at the central plane. Under this assumption, the two end-to-centre flow paths are equivalent and only one half of the full packed-bed length needs to be simulated. The adopted arrangement should therefore be interpreted as a modelling configuration specific to the present IH-PBTES analysis rather than as the conventional single-direction thermocline discharge configuration discussed in Section 1.1. The computational discharge height is therefore

$$H_{\text{half}} = \frac{H_{PB}}{2} \tag{2.77}$$

The imposed total air mass-flow rate is divided equally between the two physical ends of the storage system. The mass flow associated with the simulated half-domain is consequently

$$\dot{m}_{\text{half}} = \frac{\dot{m}_{\text{total}}}{2} \tag{2.78}$$

The final implementation follows exactly this end-to-centre half-bed configuration.

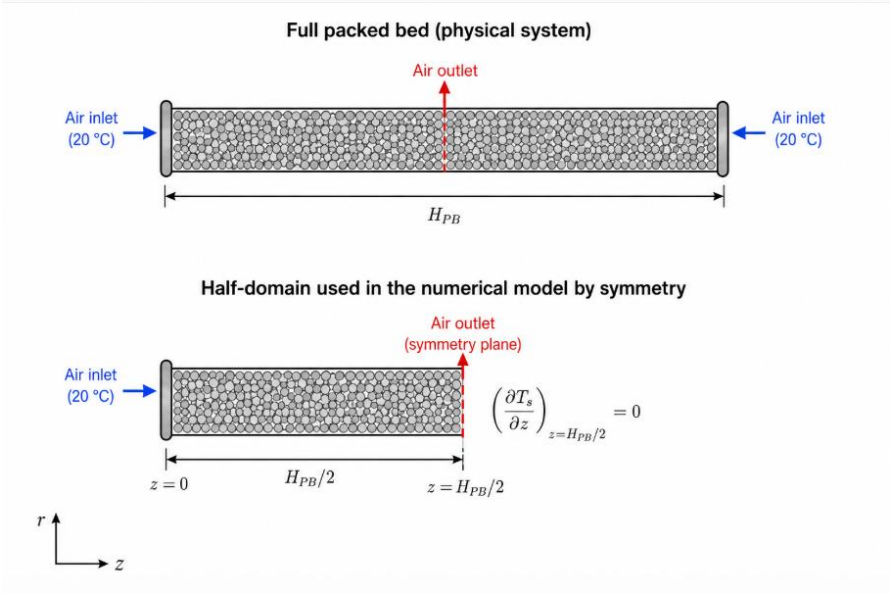


Figure 2.6– Schematic representation of the discharge configuration and half-bed computational domain adopted in the numerical model. Air enters from both physical ends of the full packed bed and flows towards a common outlet at the central plane; only one half of the system is simulated by symmetry.

Under the charging conditions adopted in the present work, the electromagnetic excitation, initial thermal condition and top and bottom boundary conditions are symmetric with respect to the central axial plane. The resulting charging temperature field is therefore expected to be symmetric about $z = H_{\text{PB}}/2$, apart from possible negligible numerical differences. For the discharge calculation, the numerical implementation nevertheless constructs a single representative half-bed by extracting the two end-to-centre halves of the complete charging map, reversing the second half to obtain a common axial orientation, and averaging the two fields according to

$$T_{s,0}^{\text{half}}(r,z) = \frac{T_{s,0}^{\text{left}}(r,z) + T_{s,0}^{\text{right,flipped}}(r,z)}{2} \tag{2.79}$$

For an exactly symmetric charging field, this averaging operation leaves the temperature distribution unchanged. Its purpose is to provide a robust numerical mapping from the complete charging domain to the single half-domain used for the symmetric end-to-centre discharge calculation. The resulting half-bed retains the radial and axial temperature non-uniformities generated during charging. At the central plane, the solid temperature therefore satisfies an axial symmetry condition,

$$\left(\frac{\partial T_s}{\partial z}\right)_{z=H_{PB}/2} = 0 \tag{2.80}$$

The physical end at z=0, by contrast, remains exposed to the ambient-loss boundary condition introduced in Section 2.6.

During discharge, no electromagnetic heat-generation term is applied. The solid phase nevertheless retains the two-dimensional axisymmetric thermal formulation developed for charging, including radial and axial conduction, temperature-dependent magnetite properties and heat losses through the exposed boundaries. The solid-energy equation can therefore be represented conceptually as

$$(1-\varepsilon)\rho_s c_{p,s}(T_s)\frac{\partial T_s}{\partial t} = k_s(T_s)\nabla^2 T_s - q_{sf} \tag{2.81}$$

Where q_{sf} represents the local volumetric rate at which thermal energy is transferred from the solid phase to the flowing air. Environmental heat losses do not appear as a separate volumetric term in Eq. (2.81), since they are imposed through the lateral and end boundary conditions described in Section 2.6. As in the charging model, the thermal conductivity of raw magnetite is used directly as the continuum conduction coefficient.

Numerically, the thermal update is performed sequentially. At each time step, the solid-temperature field is first advanced considering conduction and environmental heat losses only, producing an intermediate field T_s^* . The local solid-to-air energy extraction is then calculated and subtracted from this intermediate thermal state. This operator-splitting procedure makes it possible to retain the previously developed two-dimensional conduction solver while adding the fluid-energy extraction as a separate local process. The final code implements precisely this sequence before marching the air through each axial cell.

The air flow is assumed to be uniformly distributed over the cross-sectional area of each half-bed. The total packed-bed cross-sectional area is

$$A_{\text{cross}} = \pi R_{PB}^2 \tag{2.82}$$

The superficial mass flux associated with the simulated half-domain is therefore defined as

$$G = \frac{\dot{m}_{\text{half}}}{A_{\text{cross}}} \tag{2.83}$$

The quantity G is assumed to be uniform over the entire circular cross section. The radial discretisation is consequently interpreted as a set of parallel annular flow paths subjected to the same superficial mass flux. Because the area of the annuli increases with radius, the absolute mass flow associated with an outer annulus is larger than that associated with an inner annulus, even though the mass flux per unit area is identical. No radial mixing of the fluid between adjacent annular paths is explicitly modelled. Each radial path is instead propagated independently from

the physical inlet at z=0 to the outlet at the central plane. This modelling assumption is consistent with the axial-flow treatment adopted for the discharge model.

The thermophysical properties of air vary significantly over the temperature interval encountered during discharge. To avoid using constant fluid properties, the model employs the open-source thermophysical-property library CoolProp [55]. Air properties are evaluated at atmospheric pressure, P=101325 Pa, and tabulated over the temperature interval from 250 to 1200 K. The implemented property tables contain specific heat capacity $c_{p,f}$, density ρ_f , dynamic viscosity μ_f thermal conductivity k_f , and specific enthalpy h_f . During the transient simulation, the required values are obtained through interpolation of these precomputed tables.

Temperature-dependent air properties are retained throughout the discharge calculation in order to account for variations in the thermophysical behaviour of the fluid over the investigated temperature range. In particular, the local heat-transfer calculation uses temperature-dependent specific heat capacity, dynamic viscosity and thermal conductivity, while the recovered thermal power is evaluated from the air enthalpy rise rather than from a constant-c_p approximation. This provides a thermodynamically consistent evaluation of the energy transferred to the air without assuming constant fluid properties. The local heat-transfer coefficient between the magnetite particles and the flowing air is evaluated using the correlation proposed by Gunn [56]. This correlation was developed for heat and mass transfer in fixed and fluidised particle beds and relates the Nusselt number to Reynolds number, Prandtl number and bed porosity. It is also adopted in recent packed-bed thermal-energy-storage models, including the formulation of Calderón-Vásquez and Cardemil [54]. Gunn's original correlation covers fixed and fluidised beds over a porosity range of approximately 0.35–1.0.

Fluid properties entering the correlation are evaluated locally. An air temperature representative of each axial cell is first estimated from the inlet and outlet temperatures, while the fluid properties used in the heat-transfer correlation are evaluated at a film temperature based on the local solid and air temperatures. Since the outlet temperature itself depends on the heat-transfer coefficient, this procedure is repeated through three internal iterations in each computational cell. The Reynolds number is based on particle diameter and superficial mass flux,

$$Re = \frac{G d_p}{\mu_f} \tag{2.84}$$

while the local Prandtl number is calculated as

$$Pr = \frac{c_{p,f}\mu_f}{k_f} \tag{2.85}$$

The Gunn Nusselt-number correlation implemented in the model is

$$Nu = (7 - 10\varepsilon + 5\varepsilon^2)\left(1 + 0.7Re^{0.2}Pr^{1/3}\right) + (1 - 2.4\varepsilon + 1.2\varepsilon^2)Re^{0.7}Pr^{1/3} \quad (2.86)$$

The corresponding local particle-to-fluid heat-transfer coefficient is

$$h_{sf} = \frac{Nu\, k_f}{d_p} \quad (2.87)$$

For a packed bed of spherical monodisperse particles, the specific solid surface area available for solid–fluid heat exchange is given by [54]

$$a_s = \frac{6(1-\varepsilon)}{d_p} \quad (2.88)$$

The volumetric solid–fluid heat-transfer coefficient is consequently obtained as

$$h_v = h_{sf} a_s \quad (2.89)$$

The resulting coefficient is expressed in W $m^{-3}K^{-1}$ and represents the heat-transfer capability between the solid and fluid phases per unit packed-bed volume. This formulation is consistent with the particle-to-volumetric heat-transfer conversion adopted by Calderón-Vásquez and Cardemil [54]. The air phase is propagated sequentially along the axial direction. For every radial annulus and axial cell, the local volumetric heat-transfer coefficient is used to define a cell-scale Number of Transfer Units, where Δz_{cell} denotes the axial length of a computational cell in the discharge half-domain:

$$NTU_{\text{cell}} = \frac{h_v \Delta z_{\text{cell}}}{G c_{p,f}} \quad (2.90)$$

Although only one half of the packed bed is simulated during discharge, the axial cell size is not halved; since both the domain length and the number of axial cells are halved, $\Delta z_{\text{cell}} = H_{\text{PB}}/N_z$, equal to the axial spacing of the corresponding full-domain discretisation.

Assuming the solid temperature to remain locally constant during the passage of the air through an individual cell over the fluid-marching calculation, the corresponding outlet-air temperature is evaluated as

$$T_{f,out} = T_s - \left(T_s - T_{f,in}\right)e^{-NTU_{\text{cell}}} \quad (2.91)$$

The outlet temperature of one cell becomes the inlet temperature of the following axial cell. Air is therefore marched successively from the physical end towards the centre of the packed bed. At higher mass-flow rates, G increases and the local NTU decreases, reducing the temperature rise experienced by the air within an individual cell. The total recovered power may nevertheless increase because a larger mass of air is heated per unit time. This competition between outlet temperature and recovered power constitutes one of the main quantities investigated in the discharge Results. The implemented cell-by-cell formulation and this dependence on G are explicitly reflected in the final numerical model.

Once the outlet temperature of a cell has been obtained, its specific enthalpy is evaluated from the CoolProp-based property table. The volumetric rate at which thermal energy is transferred from the solid to the air in that cell is then calculated directly from the fluid enthalpy increase,

$$q_{sf} = \frac{G\left(h_{f,out} - h_{f,in}\right)}{\Delta z_{\text{cell}}} \tag{2.92}$$

Because G is expressed in kg $m^{-2}s^{-1}$, multiplication by the specific-enthalpy difference and division by the axial cell length produces a volumetric heat-transfer rate in W m^{-3}. This formulation provides direct energetic consistency between the fluid enthalpy increase and the heat removed from the solid.

The solid temperature is subsequently corrected from the intermediate conduction-and-loss state T_s^* according to

$$T_s^{n+1} = T_s^* - \frac{\Delta t\, q_{sf}}{(1-\varepsilon)\rho_s c_{p,s}(T_s^*)} \tag{2.93}$$

The energy gained by the air in each cell is therefore removed from the local thermal capacity of the magnetite. The air state stored within the cell is represented by the mean of the inlet and outlet enthalpies, whereas the outlet edge state is passed directly to the following cell. This sequence is repeated for all cells and radial annuli at every discharge time step.

The discharge calculations are advanced using a fixed time step of $\Delta t_{\text{dis}} = 5$ s. Starting from the 20×40 full-domain discretisation used during charging, the symmetry reduction described above results in a 20×20 computational half-domain, while preserving the same axial spatial resolution as the corresponding full-domain grid.

At the central outlet plane, different radial paths may reach different air temperatures because they have interacted with different portions of the two-dimensional solid-temperature field. The overall outlet state is therefore obtained through an area-weighted average of the specific enthalpy rather than by averaging temperature directly. For radial annulus *i*, the area weight is approximated by $A_i = 2 * \pi * r_{eff,i} * \Delta r$, with an effective radius equal to $\Delta r/2$ at the symmetry axis. The outlet enthalpy is then evaluated as

$$h_{out} = \frac{\sum_{i=1}^{N_r} h_{out,i}\, A_i}{\sum_{i=1}^{N_r} A_i} \tag{2.94}$$

The corresponding outlet temperature T_{out} is obtained through the inverse enthalpy–temperature relation for air. Since the simulation represents only one half of the packed bed while the physical system contains two identical discharge streams, the useful recovered thermal power is calculated using the total imposed air mass-flow rate,

$$P_{\text{rec}}(t) = \dot{m}_{\text{total}}[h_{\text{out}}(t) - h_{\text{in}}] \tag{2.95}$$

The cumulative thermal energy recovered during discharge is then obtained by integrating the recovered power over time,

$$E_{\mathrm{rec}}(t) = \int_0^t P_{\mathrm{rec}}(\tau)\, d\tau \tag{2.96}$$

The final implementation evaluates P_{rec} from the total mass flow and the area-averaged outlet enthalpy, and accumulates this quantity over time to obtain E_{rec}.

The discharge model provides both local and global outputs. The complete two-dimensional solid- and air-temperature fields are retained at selected times, together with the local solid-to-air volumetric heat-transfer rate. Global outputs include the mean, maximum and minimum solid temperatures, outlet-air temperature $T_{out}(t)$, recovered thermal power $P_{\mathrm{rec}}(t)$ and cumulative recovered energy $E_{\mathrm{rec}}(t)$.

An additional indicator is used to characterise the axial development of the air-temperature profile. For a prescribed target temperature, the model determines the first axial position z_{target} at which the area-averaged flowing-air temperature reaches or exceeds that target. In the discharge analyses presented in this work, 300 °C is used as a reference temperature for useful industrial heat. The crossing position is obtained by linear interpolation between neighbouring air-cell edges when the target lies between two discrete axial locations. If the target temperature is not reached anywhere within the simulated half-bed, the indicator remains undefined. This diagnostic is implemented directly in the discharge routine.

For the standalone discharge analyses, the model can be run for a prescribed maximum duration in order to investigate the influence of air mass-flow rate on outlet temperature, thermal power and recovered energy. In the repeated cycle simulations introduced in Section 2.8, the useful discharge interval is instead terminated when the outlet temperature falls below 300 °C after having first exceeded that threshold. This distinction avoids the artificial termination that would otherwise occur at the initial instant, when the outlet-air state is still assigned to the cold inlet condition. The dedicated cyclic routine explicitly implements this threshold logic.

The discharge formulation introduces several simplifying assumptions. The flow is assumed to divide equally between the two ends of the full packed bed, and only a symmetric half-domain is subsequently simulated. The initial half-bed temperature is obtained by averaging the two end-to-centre halves of the charging map. The air superficial mass flux is assumed uniform over the entire cross section, and no radial redistribution or mixing of the fluid between neighbouring annular flow paths is explicitly resolved.

The solid phase remains spatially resolved and transient, whereas the air is treated through a quasi-steady cell-by-cell marching procedure rather than through a full transient two-

dimensional fluid-energy equation. The Gunn correlation assumes a granular packed bed represented through a characteristic particle diameter and bed porosity, without resolving the local arrangement or individual particle wakes. Pressure drop is not coupled to the thermal calculation, and fan or compressor electricity is therefore not deducted from the recovered thermal energy. This should be considered when interpreting the discharge performance as a thermal rather than net-electric efficiency.

The model also neglects radial fluid conduction and explicit thermal dispersion in the air phase. Conversely, temperature-dependent thermophysical properties are retained for both the solid and the air, solid conduction remains active throughout discharge, and the lateral and physical-end thermal losses introduced in Section 2.6 continue to operate. The model therefore preserves the principal interactions required to investigate how a non-uniform two-dimensional charging state affects the subsequent recovery of sensible heat.

The discharge model consequently provides the link between the thermal state generated during induction charging and the useful thermal output of the IH-PBTES system. By retaining the two-dimensional solid-temperature distribution while propagating air locally through the packed bed, the framework can evaluate not only the total recovered energy but also the temperature quality and temporal stability of the delivered heat. The following section couples the charging and discharging models in order to analyse repeated charge–discharge operation and the evolution of the residual thermal state from one cycle to the next.

2.8 Charge-Discharge Cycle Modelling

The charging and discharging models described in the previous sections were subsequently coupled in order to investigate repeated charge–discharge operation. The analysis of cyclic behaviour is particularly relevant for packed-bed thermal energy storage because the thermal state remaining after a discharge generally differs from the initial state preceding the first charging process. Consequently, the performance of an isolated first cycle may not be representative of subsequent operation, as also recognised in the broader PBTES literature [18], [20]. The cyclic framework developed in the present work therefore preserves the complete two-dimensional residual temperature distribution between consecutive cycles rather than resetting the packed bed to a uniform initial temperature.

For each cycle, the charging model produces a final two-dimensional temperature field $T_{\mathrm{ch},end}^{(n)}(r,z)$. This field is transferred to the discharge model, which extracts useful sensible heat until the prescribed discharge stopping criterion is reached. The resulting residual solid-

temperature distribution $T_{\mathrm{dis,end}}^{(n)}(r,z)$ is then reconstructed over the full packed-bed domain and used directly as the initial condition of the following charging phase. The coupling condition between two consecutive cycles can therefore be written as

$$T_{\mathrm{ch},0}^{(n+1)}(r,z) = T_{\mathrm{dis,end}}^{(n)}(r,z) \tag{2.97}$$

This procedure retains the spatial thermal history of the storage medium and makes it possible to determine whether temperature non-uniformities decay, persist or accumulate during repeated operation.

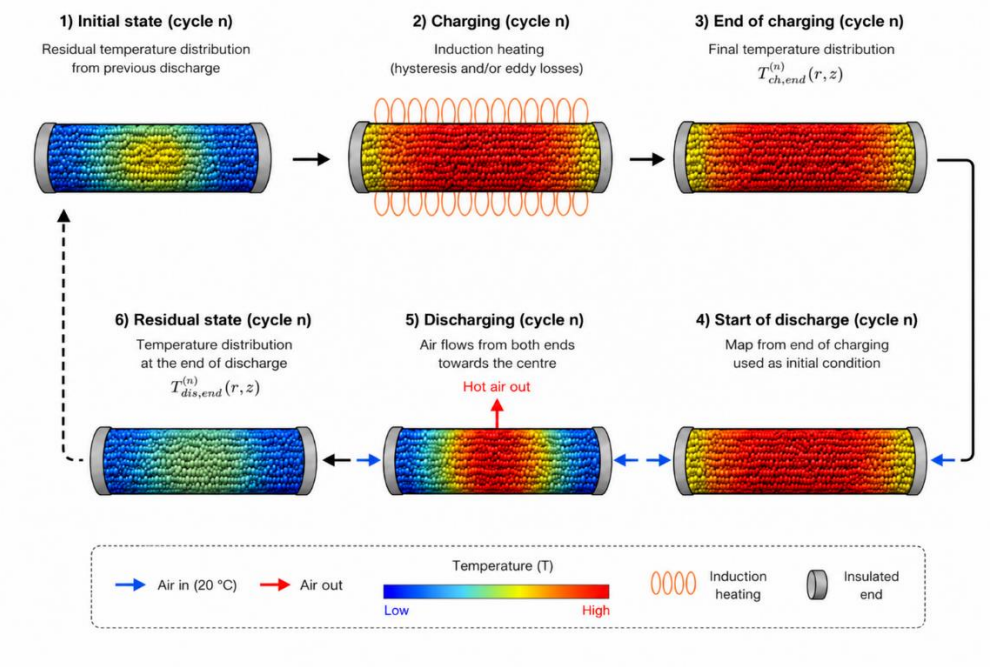


Figure 2.7– Schematic representation of the cyclic charging–discharging framework adopted for the IH-PBTES system, showing the transfer of the final charging temperature map to the discharge model and the propagation of the residual temperature distribution to the subsequent cycle.

The first cycle differs from all subsequent cycles because the storage medium is initially assumed to be at a uniform prescribed temperature. For the cyclic simulations considered in this work, the initial packed-bed temperature is equal to the ambient and inlet-air temperature, namely 20 °C. The first-cycle initial condition is therefore

$$T_{\mathrm{ch},0}^{(1)}(r,z) = T_{\mathrm{init}} = 20^{\circ}\mathrm{C} \tag{2.98}$$

From the second cycle onwards, no thermal reset is imposed and Eq. (2.97) is applied. The cyclic model therefore accounts for the sensible energy remaining in the packed bed after each useful discharge and for the non-uniform spatial distribution associated with this residual energy.

The cyclic analysis retains the isolated source modes defined in Section 2.2 solely as diagnostic cases. All other charging and discharging formulations are kept identical, so that differences between the simulations can be attributed to the distinct behaviour of the active heat-generation contribution.

The first cyclic comparison strategy is based on imposing the same target electrical-energy input during charging. A target of 300 kWh per charging phase is prescribed. In the present cycle calculations, the electrical input is defined at the coil–load level and therefore includes both the electromagnetic energy transferred to the packed bed and the Joule losses occurring in the induction coil. The charging electrical input is consequently defined as

$$E_{\mathrm{input,ch}} = E_{\mathrm{ind,ch}} + E_{\mathrm{coil,loss}} \tag{2.99}$$

Where $E_{\mathrm{ind,ch}}$ is the cumulative electromagnetic energy deposited in the packed bed and $E_{\mathrm{coil,loss}}$ is the cumulative Joule loss in the induction coil. Losses associated with the upstream frequency converter are not included in the cycle energy accounting adopted in this work. This definition is therefore consistent with the coil electrical-input convention used in the implemented cyclic model.

Under the same-energy strategy, the nominal charging target is

$$E_{\mathrm{input,target}} = 300\ \mathrm{kWh} \tag{2.100}$$

Charging is continued until the prescribed cumulative electrical input is reached, unless the maximum-temperature safety criterion described below is activated first. The use of an identical energy target provides a direct comparison of the thermal state produced by the isolated source mechanisms for the same amount of electrical energy supplied to the coil–load system.

A secondary charging stopping condition is introduced to prevent the numerical simulations from developing excessively high local temperatures. A preliminary maximum-temperature threshold of 650 °C is imposed according to

$$T_{\max}(t) \geq T_{\mathrm{max,safety}} = 650°\mathrm{C} \tag{2.101}$$

When this condition is satisfied, the charging phase is terminated even if the prescribed electrical-energy or mean-temperature target has not yet been reached.

The value of 650 °C must be interpreted exclusively as a preliminary numerical safety threshold adopted for the present simulations. It does not represent a validated material limit, a maximum allowable operating temperature of magnetite or a definitive design constraint for an IH-PBTES system. Its purpose is to prevent continued numerical charging when strongly localised hot regions develop and to provide a common stopping criterion for the cyclic analyses. The sensitivity of the conclusions to the adopted threshold should therefore be considered in future model refinements.

A second comparison strategy was introduced in order to compare the isolated charging mechanisms at a common average thermal state rather than at a common electrical-energy input. In this case, charging is targeted to a volume-averaged packed-bed temperature of 400 °C,

$$T_{\mathrm{mean,target}} = 400°\mathrm{C} \tag{2.102}$$

and the charging phase is terminated when the volume-averaged temperature defined in Eq. (2.64) reaches this value.

The maximum-temperature safety condition given by Eq. (2.101) remains active simultaneously. The actual charging stopping condition for this comparison can therefore be expressed as

$$T_{\mathrm{mean}}(t) \geq T_{\mathrm{mean,target}} \quad \text{or} \quad T_{\mathrm{max}}(t) \geq T_{\mathrm{max,safety}} \tag{2.103}$$

This distinction is important because a charging process characterised by strong spatial non-uniformity may reach the local safety threshold before the target mean temperature is attained. Such a cycle must therefore be identified as safety-limited rather than as a successful attainment of the prescribed mean-temperature target.

Each completed charging phase is followed by a discharge simulation using the model described in Section 2.7. For the cyclic calculations, the total air mass-flow rate is fixed at 0.20 kg s^{-1}, corresponding to 0.10 kg s^{-1} through each physical half of the storage system. The inlet-air temperature is maintained at 20 °C. The final charging temperature field is used directly to initialise the discharge, without any intermediate thermal reset or homogenisation beyond the half-bed transformation described in Section 2.7.

Useful discharge is defined according to the temperature quality of the air delivered by the storage system. The discharge phase is terminated when the outlet-air temperature falls below 300 °C after having previously reached or exceeded this threshold. The stopping condition can therefore be written as

$$T_{\mathrm{out}}(t) < T_{\mathrm{out,min}} = 300°\mathrm{C} \tag{2.104}$$

with the additional requirement that T_{out} must first have reached $T_{\mathrm{out,min}}$. This logic avoids immediate termination at the beginning of the discharge calculation, when the outlet state is initially associated with the cold inlet-air condition. Thermal energy remaining in the packed bed after this stopping point is retained in the residual temperature map and becomes part of the initial condition of the following charging phase.

For each cycle, the energy balance is evaluated consistently with the electrical-input definition introduced in Eq. (2.99). The electrical energy supplied during charging is partly recovered as useful thermal energy during discharge and partly dissipated through electrical losses in the induction coil. The remaining contribution is evaluated as a balance remainder according to

$$E_{\mathrm{unrec}} = E_{\mathrm{input,ch}} - E_{\mathrm{rec}} - E_{\mathrm{coil,loss}} \tag{2.105}$$

where E_{rec} is the useful thermal energy recovered during discharge, calculated according to Eq. (2.96). The quantity E_{unrec} should not be interpreted as the thermal energy lost to the surroundings. Rather, it is the residual term required to close the cycle-level energy balance.

The energy balance can equivalently be expressed as

$$E_{\mathrm{unrec}}^{(n)} = E_{\mathrm{amb,loss}}^{(n)} + \left(E_{\mathrm{sens,end}}^{(n)} - E_{\mathrm{sens,start}}^{(n)}\right) \tag{2.106}$$

where $E_{\mathrm{amb,loss}}^{(n)}$ denotes the cumulative thermal energy transferred to the surroundings during the charging and discharge phases of cycle n, while $E_{\mathrm{sens,start}}^{(n)}$ and $E_{\mathrm{sens,end}}^{(n)}$ are the sensible energies stored in the packed bed at the beginning and at the end of the same cycle, respectively. Therefore, E_{unrec} contains both the actual environmental heat losses and the net change in sensible energy retained by the storage medium over the cycle.

This distinction becomes essential after the first cycle. The first cycle starts from the prescribed cold initial state, whereas each subsequent cycle starts from the residual temperature distribution produced by the preceding discharge. Consequently, from Cycle 2 onwards, the sensible energy remaining in the packed bed at the end of discharge cannot be attributed entirely to the electrical energy supplied during that cycle. Only the net variation $E_{\mathrm{sens,end}}^{(n)} - E_{\mathrm{sens,start}}^{(n)}$ contributes to the corresponding cycle-level balance.

The balance remainder defined by Eq. (2.105) is subsequently used in the Results chapter together with the useful recovered energy and coil electrical losses to construct the cycle-level energy-balance diagrams. It must therefore be interpreted as a balance remainder rather than as a direct measure of environmental thermal losses. A cycle-level round-trip energy efficiency is defined as the ratio between the useful thermal energy recovered during discharge and the actual electrical energy supplied during the corresponding charging phase,

$$\eta_{\mathrm{RT}} = \frac{E_{\mathrm{rec}}}{E_{\mathrm{input,ch}}} \tag{2.107}$$

This indicator quantifies the fraction of the considered charging electrical input that is subsequently delivered as useful thermal energy above the adopted discharge-temperature criterion. It is important to distinguish the cycle-level round-trip efficiency η_{RT} from the overall charging efficiency η_{ch} defined in Section 2.1. The latter is an instantaneous power-based indicator referring exclusively to the charging process and is defined between the upstream electrical input and the net thermal power stored in the packed bed. It therefore accounts for converter losses, coil Joule losses and ambient thermal losses during charging, but does not include the subsequent recovery of stored heat. By contrast, η_{RT} is an energy-based indicator evaluated over a complete charge–discharge cycle. Its numerator is the useful thermal energy recovered during discharge,

while its denominator is the actual electrical energy supplied during the corresponding charging phase. Moreover, the cyclic energy accounting adopted in the present work uses the coil–load electrical boundary defined in Eq. (2.99), $E_{\mathrm{input,ch}} = E_{\mathrm{ind,ch}} + E_{\mathrm{coil,loss}}$, and therefore excludes frequency-converter losses. Consequently, η_{ch} and η_{RT} refer to different processes and slightly different system boundaries and should not be compared directly as equivalent efficiency indicators.

Particular care is required when interpreting η_{RT} for cycles terminated by the maximum-temperature safety criterion. In such cases, the actual charging energy may be substantially lower than the nominal target because charging is interrupted before the prescribed energetic or mean-temperature condition is reached. A high value of η_{RT} under these conditions therefore does not, by itself, demonstrate superior global performance. The stopping reason and the actual charging energy must always be considered together with the efficiency value.

Three consecutive charge–discharge cycles are simulated for each investigated source mode and comparison strategy. The purpose of using multiple cycles is to determine how the residual thermal state modifies the subsequent charging and discharging behaviour and whether the system begins to approach a repeatable thermal condition. The simulations are not intended to establish a mathematically rigorous periodic steady state, which would require continuing the cycle calculation until a formal convergence criterion is satisfied. Instead, the comparison between the first, second and third cycles provides an initial assessment of the transition from a cold-start condition towards quasi-cyclic operation.

For every cycle, the complete residual temperature map is propagated to the following cycle. Consequently, not only the mean residual energy but also radial and axial thermal non-uniformities are retained. This feature is particularly important for the present two-dimensional framework because a cycle may exhibit a similar mean temperature to another one while containing substantially different local temperature maxima and minima.

A common set of charging and discharging quantities is recorded for each simulated cycle. During charging, the model stores the actual electrical input $E_{\mathrm{input,ch}}$, electromagnetic energy transferred to the packed bed $E_{\mathrm{ind,ch}}$, coil Joule losses $E_{\mathrm{coil,loss}}$, charging duration, final mean temperature, maximum and minimum solid temperatures, and the reason for charging termination. The complete two-dimensional final charging map is also retained.

During discharge, the stored outputs include the useful recovered energy E_{rec}, discharge duration, outlet-air temperature, final mean, maximum and minimum solid temperatures, and the complete residual two-dimensional temperature map. From these quantities, the round-trip efficiency defined by Eq. (2.107) and the unrecovered contribution defined by Eq. (2.105) are

subsequently evaluated. The latter decomposition provides the basis for distinguishing useful recovered energy, electrical coil losses and unrecovered thermal energy / losses in the cycle energy-balance visualisations.

The principal parameters and stopping conditions adopted for the cyclic simulations are summarised in Table 2.3. These settings are applied consistently to the isolated hysteresis and eddy-current cases, except where charging is terminated earlier by the maximum-temperature safety criterion.

Parameter	**Adopted value**
Number of consecutive cycles	3
Initial packed-bed temperature, Cycle 1	20 °C
Air inlet temperature	20 °C
Total discharge air mass-flow rate	0.20 kg s^{-1}
Same-energy charging target	300 kWh
Same-mean-temperature target	400 °C
Preliminary numerical safety threshold	650 °C
Useful discharge temperature threshold	300 °C
Electrical-input definition	Induced energy + coil Joule losses
Converter losses in cycle energy accounting	Not included

Table 2.4 Main operating conditions and stopping criteria adopted in the charge–discharge cycle simulations.

The cyclic framework inherits the assumptions of the charging and discharging models described in the previous sections. In addition, the hysteresis and eddy-current contributions are activated separately rather than simultaneously, and their cyclic behaviour must therefore be interpreted as an analysis of isolated heating contributions. Material ageing, mechanical degradation, changes in pebble arrangement and irreversible modification of the thermophysical or electromagnetic properties after repeated thermal exposure are not represented.

The cyclic energy accounting is based on the electrical energy supplied to the coil–load system and does not include frequency-converter losses or auxiliary electrical consumption associated with air circulation. The round-trip efficiency defined in Eq. (2.107) is therefore a thermal recovery indicator based on the specific system boundaries adopted in the present model rather than a complete plant-level electrical-to-useful-heat efficiency.

The discharge-temperature threshold of 300 °C is used to distinguish useful high-temperature heat from the lower-temperature energy remaining in the storage system, while the 650 °C charging threshold is a preliminary numerical safeguard rather than a validated physical

design limit. Different choices of these thresholds would modify the calculated recovered energy and cyclic performance and should therefore be considered in future sensitivity analyses.

Despite these limitations, the developed cyclic framework provides a consistent method for propagating the complete spatial thermal state of the IH-PBTES system through repeated charging and discharging processes. It enables the evolution of electrical-energy requirements, useful heat recovery, temperature non-uniformity and local thermal constraints to be evaluated simultaneously. The methodology described in Sections 2.1–2.8 therefore provides the complete numerical framework used to generate the results presented in the following chapter.

3. Results

3.1 Model Validation

Before analysing the spatially non-uniform induction-heating problem, the newly developed two-dimensional thermal formulation was validated against the reference lumped IH-PBTES model described in Section 2.1. The purpose of this validation was to verify the numerical implementation of the two-dimensional thermal solver independently of the additional complexity introduced by the spatial magnetic-field distribution. For this reason, the non-uniform electromagnetic field was not activated during the validation test. Instead, the packed bed was subjected to the same uniform heat-source assumption adopted in the reference model [52].

The validation was performed at a coil current of 1066 A and an excitation frequency of 80 Hz. Both models were simulated over a charging period of three hours under equivalent thermal and electromagnetic assumptions. Since the reference lumped formulation represents the entire packed bed through a single temperature, its prediction was compared with the volume-averaged temperature of the two-dimensional model, calculated according to Eq. (2.64). The comparison between the temperature results obtained from the two formulations is shown in Figure 3.1.

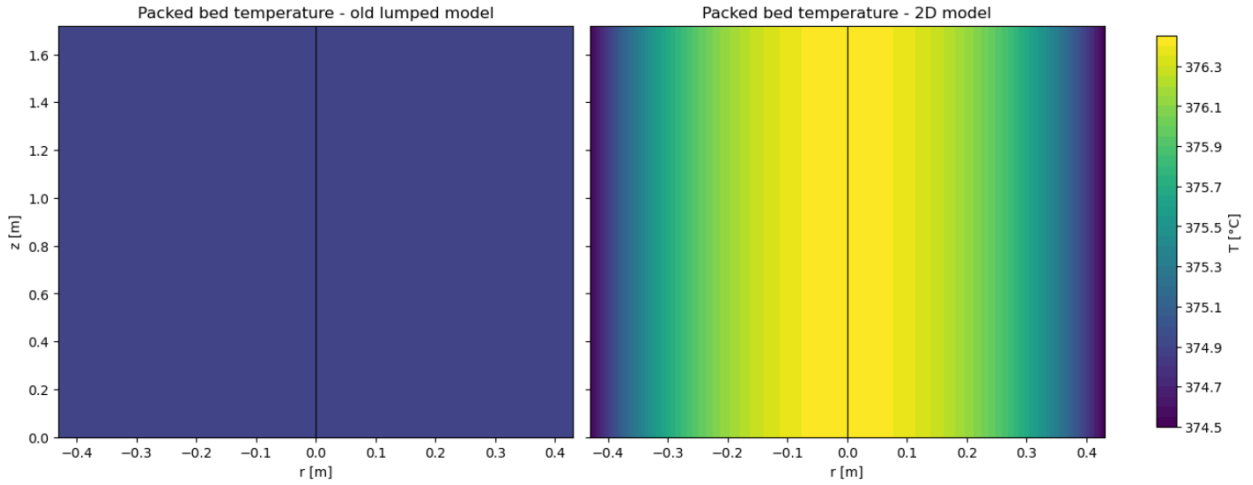


Figure 3.1– Comparison between the temperature results obtained with the reference lumped model and the two-dimensional thermal model under equivalent uniform-source validation conditions.

Although a uniform volumetric heat source is imposed in both models during the validation test, the two-dimensional formulation develops a slight spatial temperature gradient due to the locally resolved heat losses at the external boundaries. Consequently, the central region of the packed bed remains slightly warmer than the regions close to the external surfaces. The reference lumped model cannot reproduce this spatial behaviour, since the entire storage medium is represented by a single bulk temperature. The relevant quantity for validation is therefore the

volume-averaged temperature of the two-dimensional domain rather than the local temperature distribution.

As shown in Figure 3.1, the two-dimensional thermal model reproduces very closely the thermal response predicted by the reference lumped formulation when the same uniform-source assumption is imposed. After three hours of charging, the reference model predicts a packed-bed temperature of 374.9 °C, whereas the volume-averaged temperature obtained with the two-dimensional model is 375.6 °C. The resulting absolute difference is only 0.7 °C and therefore remains below 1 °C, indicating a very close agreement between the two numerical formulations.

The main validation results are summarised quantitatively in Table 3.1.

Quantity	**Value**
Coil current	1066 A
Excitation frequency	80 Hz
Charging duration	3h
Reference lumped-model final temperature	374.9 °C
2D volume-averaged final temperature	375.6 °C
Absolute temperature difference	0.7 °C

Table 3.1– Main operating conditions and final temperature comparison used for validation of the two-dimensional thermal model.

The close agreement obtained between the two models confirms that the discretisation of the packed-bed domain and the numerical implementation of the transient thermal balance do not introduce significant deviations with respect to the previously established lumped formulation. In particular, when spatial variations of the heat source are intentionally removed, the introduction of the two-dimensional computational domain does not alter the overall thermal response of the storage medium. This validation step is particularly important because it isolates the thermal formulation from the subsequent electromagnetic extension of the model. A direct comparison performed after introducing the finite-coil magnetic-field distribution would not provide an equivalent validation condition, since the reference and two-dimensional models would then be subjected to different spatial heat-generation patterns. By maintaining a uniform source during the validation stage, the agreement between the two formulations can instead be attributed directly to the consistency of the thermal implementation.

Following this verification, the uniform-field assumption was removed and the complete two-dimensional formulation was activated. The spatial magnetic-field distribution $H(r,z)$, the corresponding local induction heat-generation terms and the temperature-dependent material properties described in Chapter 2 were therefore introduced. The resulting spatial and transient

charging behaviour is analysed in the following section, where the isolated contributions of hysteresis and eddy-current heating are examined.

3.2 Hysteresis and Eddy-Current Heating Analysis

Following the validation of the two-dimensional thermal implementation, the complete charging model was activated by introducing the non-uniform magnetic-field distribution, the local temperature-dependent induction source and the thermal boundary conditions described in Chapter 2. The resulting framework was then used to investigate separately the characteristic behaviour of hysteresis and eddy-current heating.

As discussed in Section 2.2, the two source modes are analysed separately only to isolate their characteristic thermo-electromagnetic response.

Two distinct operating conditions were therefore selected. The hysteresis-only case was simulated at a low excitation frequency of 80 Hz and a coil current of approximately 2203 A. The current was selected so that the minimum local peak magnetic-field intensity remained above approximately 20 kA/m throughout the packed bed, preventing operation in the low-field region in which the adopted hysteresis model becomes poorly constrained. The eddy-current-only case was instead investigated at 50 kHz and 100 A. The two operating points are summarised in Table 3.2.

Case	**Coil current**	**Frequency**	**Active induction source**
Hysteresis-only	≈ 2203 A	80 Hz	q_{hys}
Eddy-current-only	100 A	50 kHz	q_{eddy}

Table 3.2 – Operating conditions adopted to isolate the hysteresis and eddy-current contributions during the charging analysis.

The temporal behaviour of the hysteresis-only charging process is shown in Figure 3.2. Starting from the initially cold packed bed, the temperature increases continuously throughout the three-hour charging period. The mean and maximum temperatures follow a smooth evolution, reaching approximately 418 °C and 446 °C, respectively, at the end of the simulation.

At the same time, a markedly different trend is observed for the induction heat-generation rate. The volume-averaged induced power density decreases progressively from approximately 120 kW/m³ at the beginning of charging to approximately 48 kW/m³ after three hours. Consequently, the total induced power follows the same decreasing trend, falling from approximately 120 kW to 48 kW over the simulated period, as illustrated in Figure 3.2.

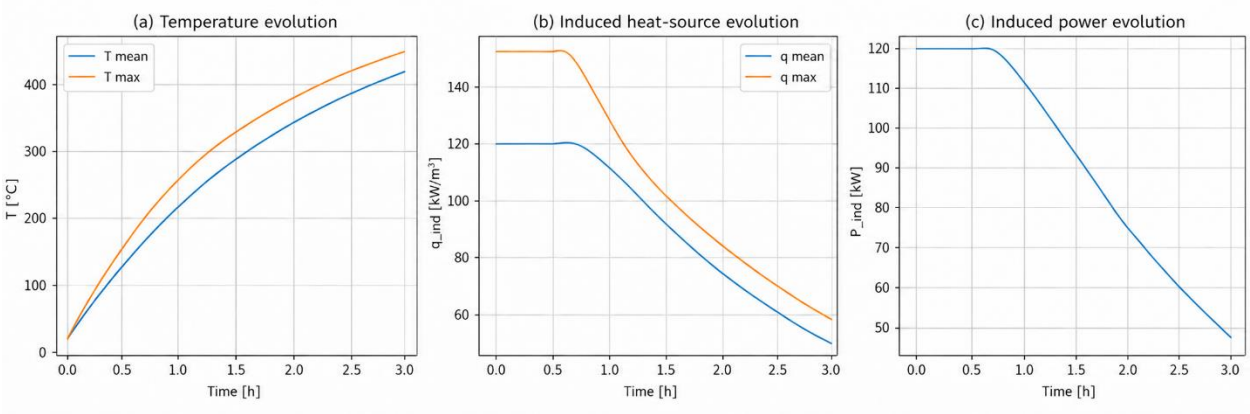


Figure 3.2– Temporal evolution of (a) mean and maximum packed-bed temperature, (b) mean and maximum induced volumetric heat-generation rate, and (c) total induced power during the hysteresis-only charging simulation at 80 Hz and approximately 2203 A.

The reduction in induced power as the packed bed becomes hotter is a direct consequence of the temperature dependence of the hysteresis contribution. As the magnetite temperature increases, the hysteresis-loop area used by the model progressively decreases. Since the volumetric hysteresis source is proportional to the hysteresis energy dissipated per cycle, the resulting heat-generation rate decreases as charging proceeds. The hysteresis-only case therefore exhibits a negative thermo-electromagnetic feedback: increasing temperature reduces the local heat-generation rate, which in turn limits the subsequent rate of temperature increase.

This behaviour provides a degree of thermal self-regulation. Regions experiencing a stronger initial heat-generation rate progressively reduce their hysteresis contribution as their temperature rises, limiting the amplification of local temperature differences. Nevertheless, the final thermal field is not perfectly uniform because both the magnetic excitation and the heat losses vary spatially within the finite packed-bed geometry.

The spatial distributions of temperature and hysteresis heat generation provide a clearer representation of this effect and are shown in Figure 3.3.

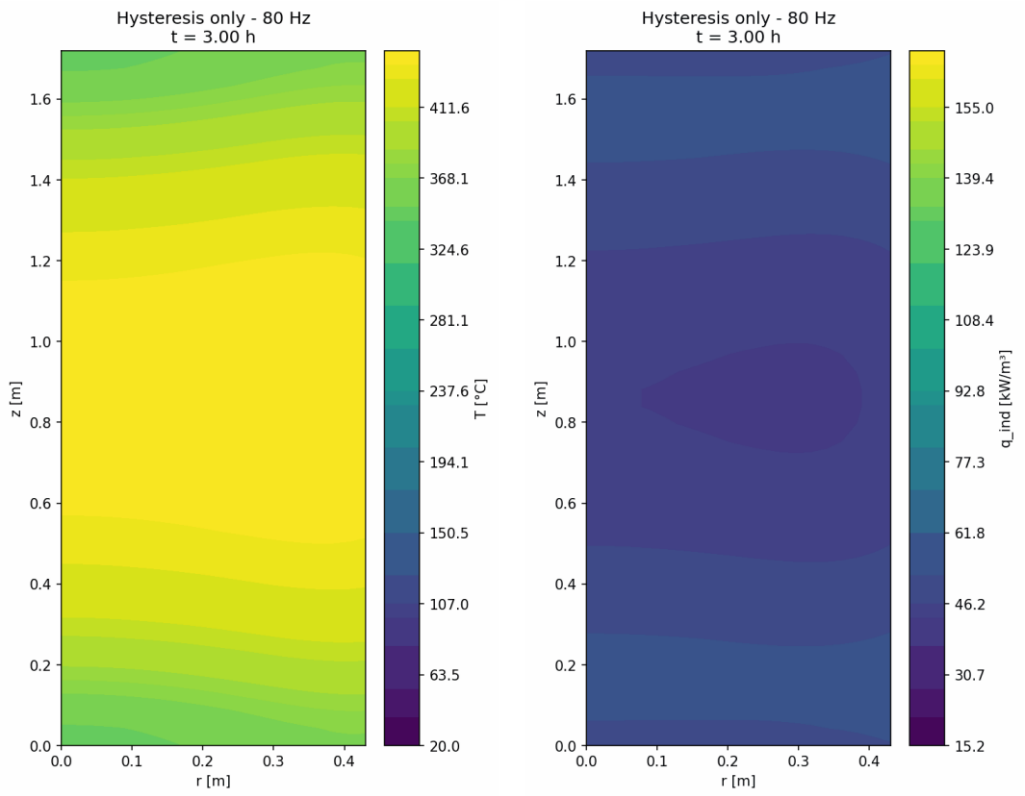


Figure 3.3– Final two-dimensional distributions of (a) packed-bed temperature and (b) hysteresis heat-generation rate after three hours of hysteresis-only charging.

As shown in Figure 3.3, the final temperature field presents a warmer central region and lower temperatures towards the boundaries of the packed bed. This distribution results from the combined effect of the non-uniform magnetic excitation, local temperature-dependent heat generation, thermal conduction and heat exchange with the surroundings. In particular, cooling near the axial ends is enhanced by the top and bottom thermal losses introduced in the two-dimensional model.

The corresponding heat-source distribution does not simply reproduce the final temperature field. As the temperature increases locally, the hysteresis contribution weakens, so that the hottest regions progressively experience a reduction in heat-generation intensity. This behaviour is consistent with the decreasing global induced-power trend observed in Figure 3.2 and confirms that the negative temperature feedback acts both temporally and spatially in the hysteresis-only simulation.

The eddy-current-only case exhibits a substantially different transient response. Figure 3.4 shows the evolution obtained at an excitation frequency of 50 kHz and a coil current of 100 A. After three hours of charging, the mean packed-bed temperature reaches approximately 331 °C, while the maximum local temperature reaches approximately 434 °C. Although the maximum temperature is therefore of the same order as in the hysteresis-only case, the significantly lower mean temperature indicates a considerably larger spatial temperature non-uniformity.

A second major difference concerns the evolution of the heat-generation rate. In contrast to the hysteresis-only simulation, the volume-averaged eddy-current source increases continuously during charging, from approximately 34 kW/m³ to 113 kW/m³. The total induced power consequently increases from approximately 34 kW at the beginning of the simulation to approximately 112 kW after three hours.

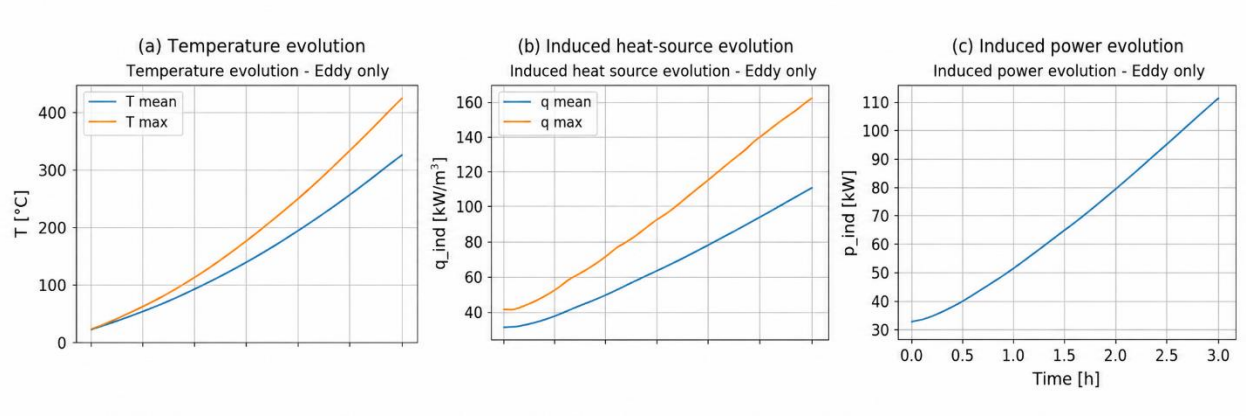


Figure 3.4– Temporal evolution of (a) mean and maximum packed-bed temperature, (b) mean and maximum induced volumetric heat-generation rate, and (c) total induced power during the eddy-current-only charging simulation at 50 kHz and 100 A.

The increasing source intensity shown in Figure 3.4 originates primarily from the temperature dependence of the electrical conductivity adopted for magnetite. Within the temperature range considered in the model, electrical conductivity increases as the material becomes hotter. Since the eddy-current heat-generation formulation depends on the electrical properties of the storage material, an increase in local temperature can consequently reinforce the eddy-current contribution.

The eddy-current-only simulation therefore exhibits a positive thermo-electromagnetic feedback. A region that becomes warmer experiences an increase in electrical conductivity and can consequently generate a larger local eddy-current source. This additional heating further increases its temperature and can progressively amplify spatial differences within the packed bed. The contrast with the self-regulating hysteresis behaviour is evident from the opposite evolution of the induced power in Figures 3.2 and 3.4.

The resulting localisation can be observed more directly from the final spatial distributions reported in Figure 3.5.

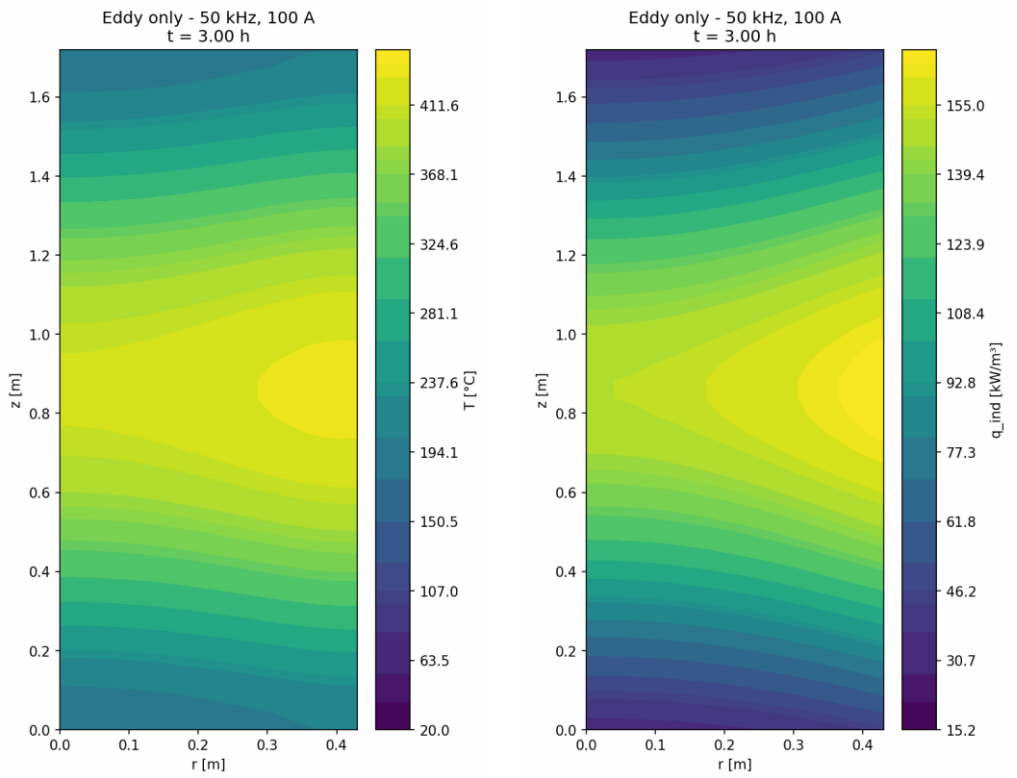


Figure 3.5– Final two-dimensional distributions of (a) packed-bed temperature and (b) eddy-current heat-generation rate after three hours of eddy-current-only charging.

Figure 3.5 confirms the stronger spatial localisation associated with the eddy-current contribution. The temperature field exhibits a larger difference between the hottest regions and the volume-averaged thermal state than in the hysteresis-only case. This behaviour is consistent with the difference between $T_{max} \approx 434°C$ and $T_{mean} \approx 331°C$, corresponding to a temperature difference exceeding 100 °C.

The spatial distribution of the eddy-current source further illustrates the positive feedback described above. Regions in which the combination of magnetic-field intensity and temperature-dependent electrical conductivity favours stronger heat generation progressively receive a larger fraction of the induced power. The resulting temperature field is therefore more strongly affected by local electromagnetic non-uniformities than in the hysteresis-only simulation.

The opposite thermal feedback associated with the two isolated heating contributions becomes particularly evident when their induced-power and heat-generation evolutions are compared

directly. Figure 3.6 reports the total induced power together with the maximum volumetric heat-generation rates for the hysteresis-only and eddy-current-only cases.

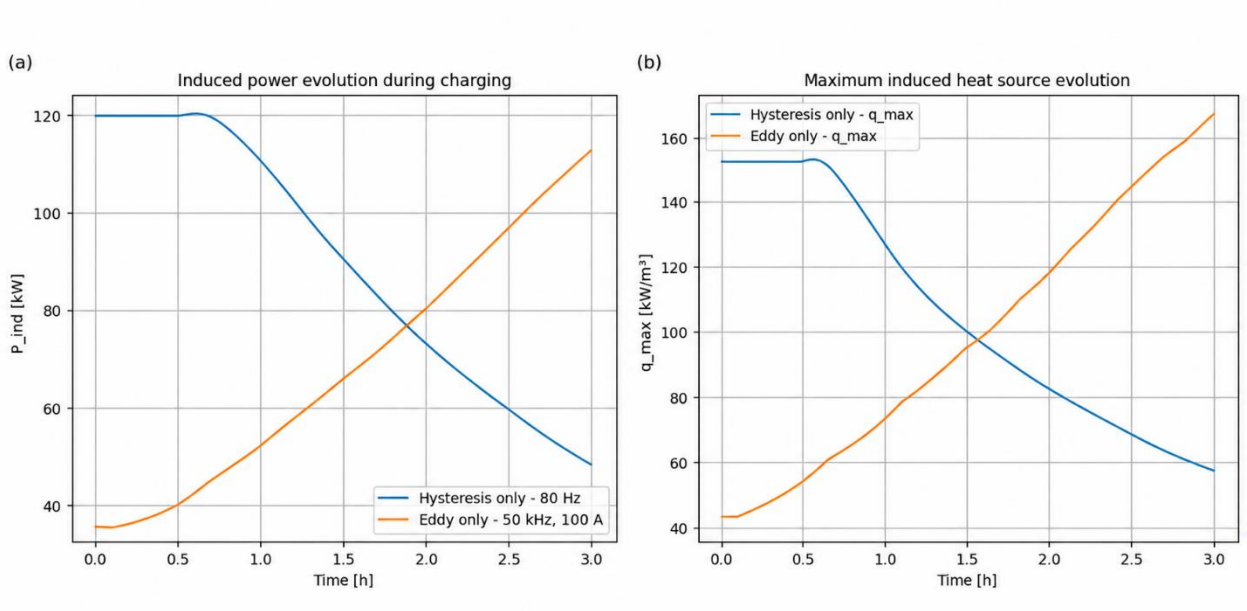


Figure 3.6 – Comparison between the hysteresis-only and eddy-current-only charging simulations in terms of (a) total induced power and (b) maximum induced volumetric heat-generation rate.

As shown in Figure 3.6, the two mechanisms exhibit opposite transient trends. The hysteresis contribution is initially stronger but progressively decreases as the packed bed becomes hotter, whereas the eddy-current contribution increases continuously with temperature. The comparison therefore reveals two fundamentally different thermo-electromagnetic feedback mechanisms rather than simply two heat sources of different magnitude.

Because the two simulations correspond to different operating points, the comparison is intended to contrast their characteristic transient behaviour rather than to rank the two heating mechanisms directly.

In addition to the thermal behaviour, the two operating regimes differ substantially in terms of charging efficiency. The efficiency indicators calculated according to the definitions adopted from the reference IH-PBTES framework are compared in Figure 3.7. The comparison includes the induction efficiency η_{ind}, the thermal charging efficiency η_{th} and the overall charging efficiency η_{ch}, according to the definitions introduced in Section 2.1. These quantities describe the instantaneous performance of the charging process as the packed-bed temperature evolves and should not be confused with the cycle-level round-trip efficiency η_{RT} introduced in Section 2.8.

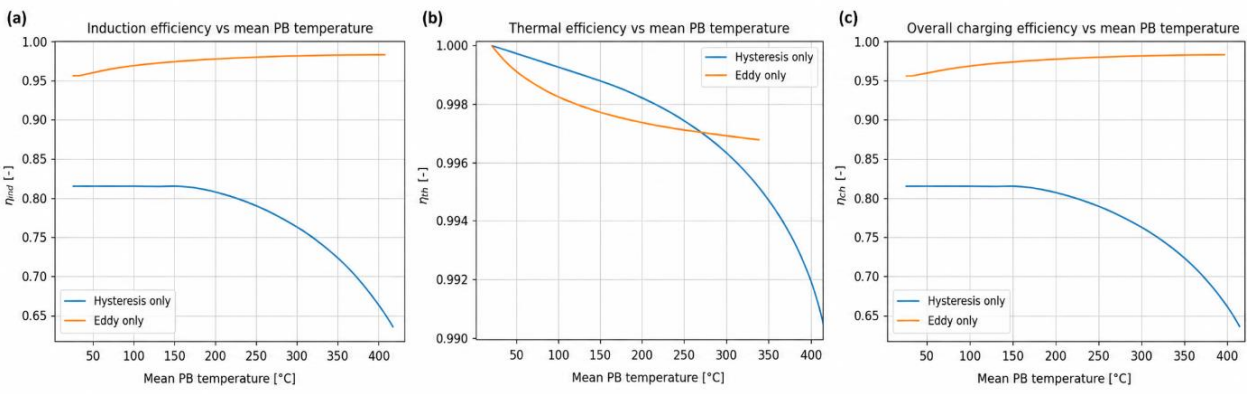


Figure 3.7– Evolution of (a) induction efficiency η_{ind}, (b) thermal charging efficiency η_{th} and (c) overall charging efficiency η_{ch} for the hysteresis-only and eddy-current-only operating conditions.

The efficiency comparison highlights the strong influence of the selected electrical operating point. In the hysteresis-only simulation, a coil current in the kiloampere range was adopted in order to maintain the minimum local peak magnetic-field intensity above approximately 20 kA/m, where the adopted LangArc hysteresis model remains sufficiently well constrained. This requirement is therefore a limitation of the present hysteresis modelling approach rather than a physical lower bound on the coil current required for hysteresis heating. In a real system, or with a hysteresis model validated over a wider low-field range, lower coil currents could in principle be considered, leading to lower Joule losses in the induction coil and potentially higher induction efficiency. Consequently, the lower induction efficiency obtained for the hysteresis-only case should not be interpreted as an intrinsic disadvantage of hysteresis heating, but rather as a result that is partly influenced by the operating condition imposed by the adopted LangArc formulation.

Within the operating conditions investigated here, the eddy-current-only case exhibits substantially lower coil electrical losses and therefore a higher induction efficiency. This electrical advantage must nevertheless be considered together with the corresponding thermal response: the eddy-current case develops a more strongly localised temperature field, whereas the hysteresis contribution exhibits a more uniform and self-regulating behaviour. The comparison should therefore be interpreted as a contrast between the two simulated operating regimes rather than as a general ranking of the two heating mechanisms.

The results presented in this section demonstrate that temperature-dependent electromagnetic behaviour plays a decisive role in the transient response of the IH-PBTES system. The hysteresis and eddy-current contributions exhibit opposite feedback with increasing temperature, leading to different source evolutions, temperature distributions and electrical-loss characteristics. In addition to the heating mechanism itself, however, the spatial distribution of the magnetic field is strongly affected by the geometry of the packed bed and surrounding coil. The

influence of this geometrical parameter is therefore investigated in the following section through a systematic packed-bed aspect-ratio analysis.

3.3 Effect of Packed-Bed Aspect Ratio

The influence of packed-bed geometry on the charging behaviour was investigated by varying the aspect ratio AR=H_{PB}/D_{PB} . Since a modification of the packed-bed dimensions also changes the magnetic coupling between the induction coil and the storage material, a direct comparison performed at constant coil current would not isolate the geometrical effect. Different aspect ratios operated at the same current would in fact experience different average magnetic-field intensities and, consequently, different electromagnetic excitation levels.

For this reason, the coil current was recalculated for each geometry so that the volume-averaged magnetic field inside the packed bed remained equal to the reference value. In the hysteresis-only simulations, the corrected current was additionally required to satisfy the local condition $H_{peak,min} \geq 20 kA/m$ throughout the domain, ensuring that all computational cells remained within the adopted validity range of the hysteresis model. For the eddy-current-only simulations, the target corresponded instead to the volume-averaged RMS magnetic field of the reference 50 kHz, 100 A case. Consequently, the remaining differences between the investigated configurations can primarily be associated with the packed-bed geometry, the spatial distribution of the magnetic field, heat losses and temperature-dependent material properties rather than with a different average electromagnetic excitation.

The corrected coil currents and the corresponding final volume-averaged induction heat-generation rates are reported in Figure 3.8.

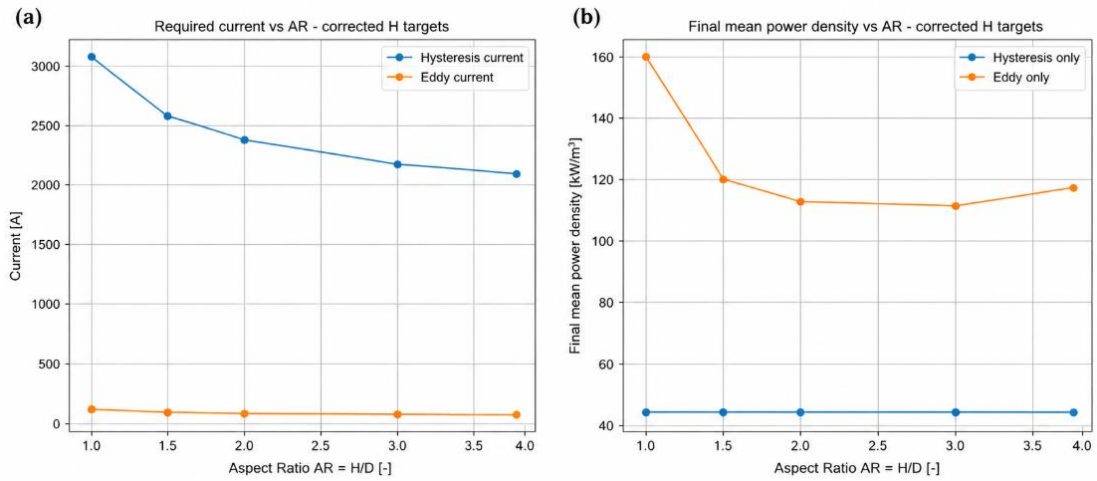


Figure 3.8– Effect of packed-bed aspect ratio on (a) the corrected coil current required to maintain the prescribed average magnetic-field intensity and (b) the final volume-averaged induction heat-generation rate for the isolated hysteresis and eddy-current cases.

As shown in Figure 3.8(a), the coil current required to preserve the prescribed magnetic-field target decreases as the packed-bed aspect ratio increases. This indicates that the electromagnetic coupling between the coil and the storage volume is significantly affected by the packed-bed geometry. The difference in current magnitude between the two isolated regimes nevertheless remains substantial, with the hysteresis-only cases requiring currents in the kiloampere range, while the eddy-current cases operate at considerably lower currents.

The effect of the geometrical correction on the heat-generation rate is shown in Figure 3.8(b). Once the average magnetic-field intensity is normalised, the final volume-averaged hysteresis contribution remains only weakly affected by the aspect ratio. The eddy-current contribution instead exhibits a substantially stronger dependence on geometry, with the AR=1 configuration producing the highest final mean power density among the investigated cases.

This difference demonstrates that an equivalent volume-averaged magnetic-field intensity does not imply an equivalent local electromagnetic response. The aspect ratio changes the spatial distribution of the magnetic field within the finite coil–packed-bed geometry. Since the eddy-current source depends strongly on the local magnetic-field intensity and on the temperature-dependent electrical conductivity, these geometrical differences can be progressively amplified during charging. The final temperature non-uniformity is quantified through the temperature spread $\Delta T = T_{\max} - T_{\min}$. The resulting effects on the final thermal response and on the overall charging efficiency are reported in Figure 3.9.

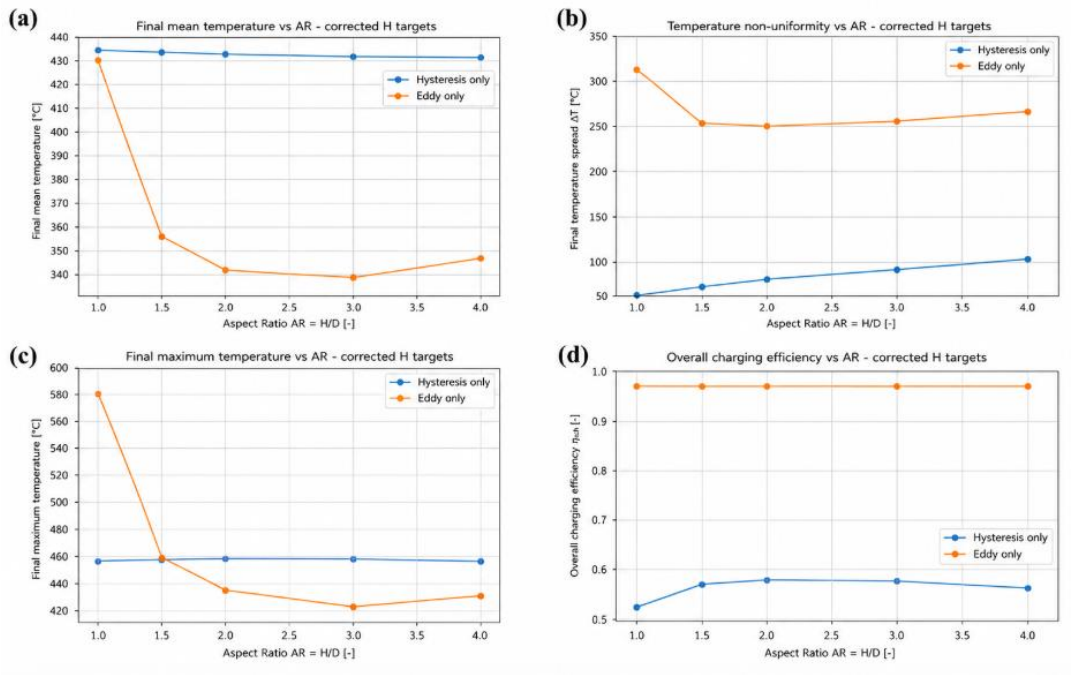


Figure 3.9– Effect of packed-bed aspect ratio on (a) final mean temperature, (b) temperature non-uniformity, (c) final maximum temperature and (d) overall charging efficiency for the isolated hysteresis and eddy-current charging simulations.

The hysteresis-only simulations exhibit a relatively limited variation of the final mean and maximum packed-bed temperatures once the average magnetic-field excitation is corrected. This behaviour is consistent with the comparatively small variation of the mean hysteresis heat-generation rate observed in Figure 3.8(b). The temperature spread, however, remains sensitive to the packed-bed shape, indicating that similar mean thermal conditions do not necessarily correspond to the same degree of spatial temperature uniformity.

The eddy-current-only simulations show a substantially stronger sensitivity to aspect ratio. In particular, the AR=1 configuration develops a more pronounced local temperature increase, resulting in a larger separation between the maximum and average thermal state of the packed bed. Intermediate and more elongated configurations exhibit a more controlled spatial thermal response under the corrected magnetic-field condition.

The effect of aspect ratio is also reflected in the overall charging efficiency, as shown in Figure 3.9(d). Changes in geometry influence not only the temperature field but also the electrical operating conditions required to maintain the prescribed magnetic excitation. Consequently, the overall charging performance results from the combined effect of electromagnetic coupling, induced heat generation, coil losses and thermal losses.

The efficiency trend should therefore not be interpreted independently from the temperature indicators. A configuration exhibiting favourable electrical or overall charging performance may simultaneously develop a larger local maximum temperature or a less uniform thermal field. The aspect-ratio analysis consequently highlights the need to consider both energetic performance and spatial thermal behaviour when evaluating different packed-bed geometries.

The spatial origin of these differences can be examined directly through the final temperature distributions shown in Figure 3.10.

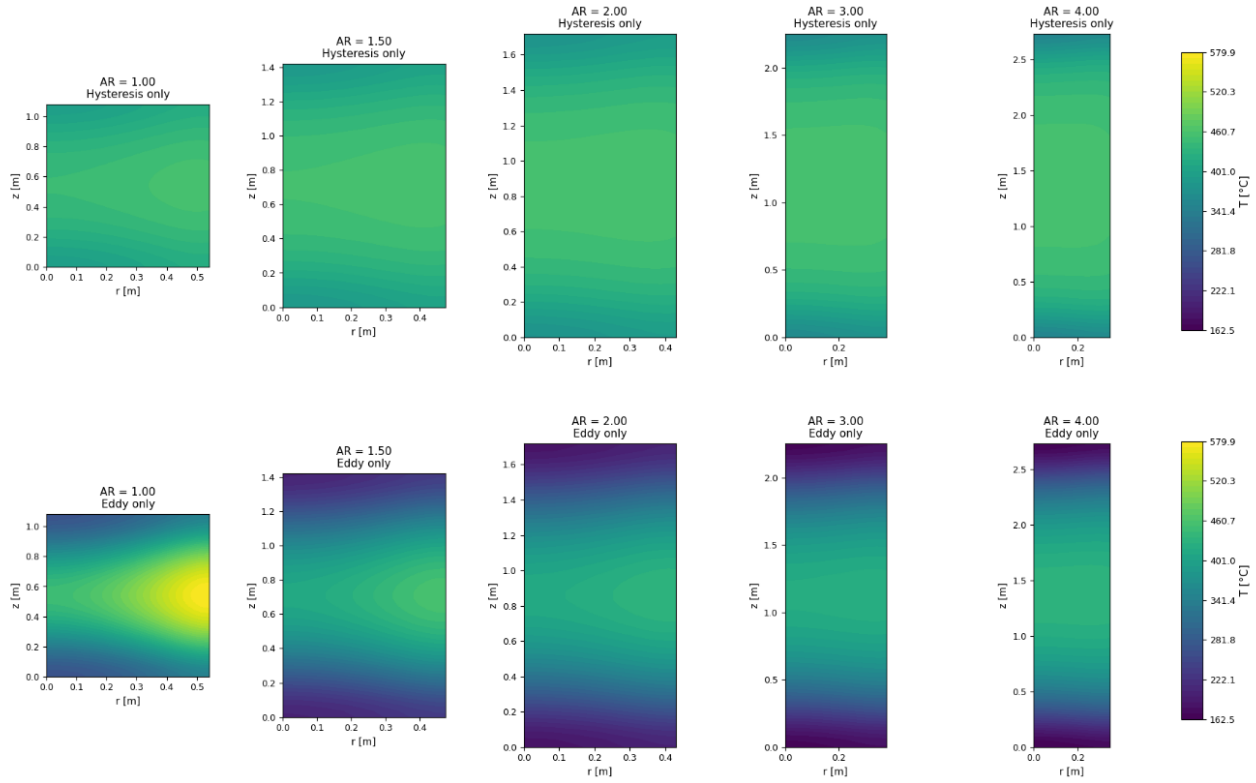


Figure 3.10– Final two-dimensional temperature distributions obtained for the investigated packed-bed aspect ratios. The upper row refers to the hysteresis-only simulations, while the lower row corresponds to the eddy-current-only cases. The geometrical proportions of the packed beds are preserved.

The temperature maps in Figure 3.10 provide a spatial representation of the trends previously identified from the global indicators. In the hysteresis-only simulations, the temperature distributions remain comparatively uniform over the investigated geometries. Although the position and extent of the warmer regions vary with aspect ratio, the thermal field does not exhibit the strong localised behaviour observed in the eddy-current cases.

A markedly stronger dependence on geometry is visible in the eddy-current-only temperature maps. The AR=1 configuration exhibits the most pronounced localisation of the high-temperature region, whereas the other investigated geometries distribute the generated heat more broadly throughout the packed-bed volume. These differences occur even though the volume-averaged magnetic-field intensity has been corrected to the same target value, confirming that the local electromagnetic-field distribution plays a fundamental role in determining the thermal response. The temperature distribution is additionally influenced by thermal conduction and by the external boundary losses described in Section 2.6. Therefore, the final temperature field represents the combined response to spatially varying electromagnetic heat generation and thermal transport rather than a direct reproduction of the magnetic-field distribution alone.

To further identify the origin of these thermal patterns, the corresponding final induction heat-generation distributions are presented in Figure 3.11.

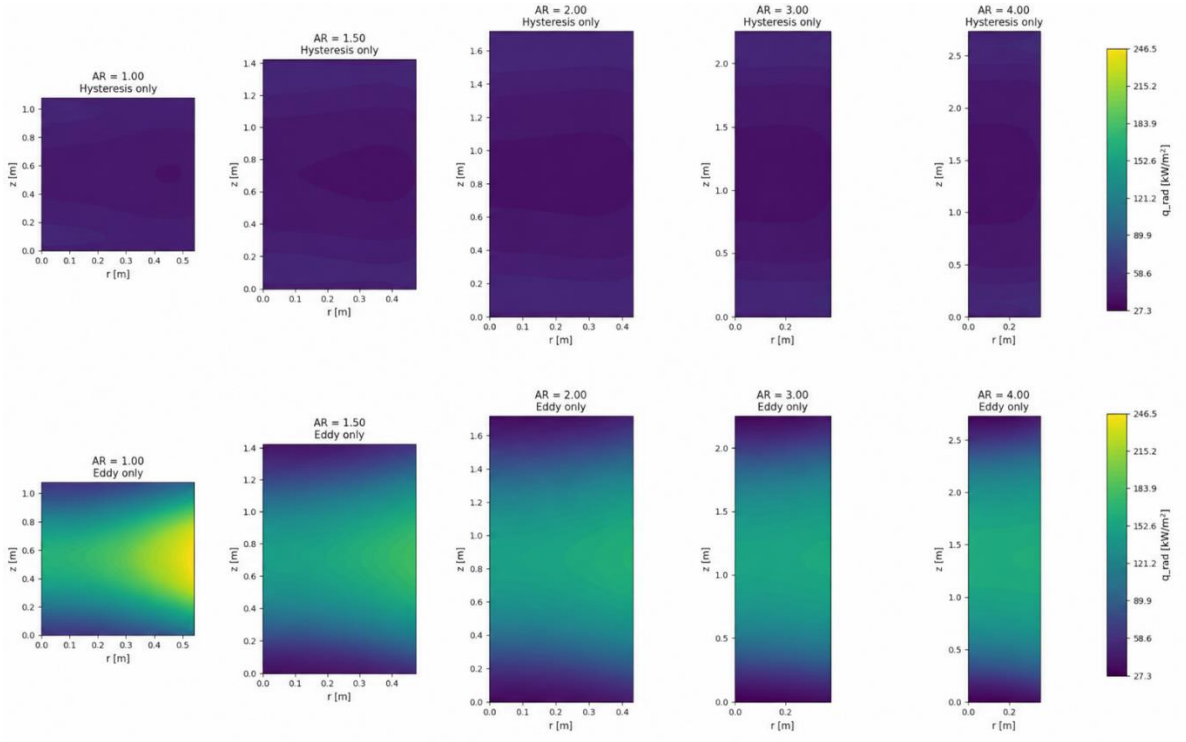


Figure 3.11– Final two-dimensional induction heat-generation distributions obtained for the investigated packed-bed aspect ratios. The upper row refers to the hysteresis contribution, while the lower row corresponds to the eddy-current contribution.

The final heat-generation distributions in Figure 3.11 clarify the different sensitivities observed in the thermal response. In the hysteresis-only simulations, regions that reach higher temperatures progressively experience a reduction in the local hysteresis contribution. This behaviour is associated with the temperature dependence of the hysteresis-loop area and represents the spatial manifestation of the negative thermo-electromagnetic feedback identified in Section 3.2.

The eddy-current cases exhibit the opposite behaviour. Regions characterised by a favourable combination of magnetic-field intensity and increased electrical conductivity can experience progressively stronger local heat generation. Since the implemented conductivity model increases with temperature over the investigated range, the local eddy-current source can reinforce already warmer regions. This positive feedback contributes to the stronger localisation observed in the corresponding temperature maps and explains the greater sensitivity of the eddy-current contribution to packed-bed geometry.

Overall, the aspect-ratio analysis demonstrates that the geometry of the packed bed affects the IH-PBTES response even when the investigated configurations are compared at equivalent volume-averaged magnetic excitation. The hysteresis contribution remains comparatively robust with respect to changes in aspect ratio, particularly in terms of mean heat-generation rate and mean thermal response, while variations in geometry still affect temperature uniformity. The eddy-

current contribution is considerably more sensitive to the local electromagnetic-field distribution and can lead to pronounced spatial temperature concentrations for less favourable configurations.

The results also show that no single indicator is sufficient to evaluate the influence of aspect ratio. Current requirements, heat-generation intensity, temperature uniformity, maximum temperature and overall charging efficiency must be considered together. A definitive identification of an optimal packed-bed geometry would therefore require a broader multi-objective design assessment and is beyond the scope of the present parametric analysis.

The following section moves from the charging stage to the discharge process. The final two-dimensional temperature fields obtained for the reference hysteresis-only and eddy-current-only charging cases discussed in Section 3.2 are used as the initial thermal states for the discharge analysis. These correspond to the hysteresis-only case at 80 Hz and approximately 2203 A and the eddy-current-only case at 50 kHz and 100 A, respectively. The subsequent analysis investigates the recovery of the stored sensible energy through the air-flow discharge model.

3.4 Discharging Analysis

The discharge analysis was performed using the final two-dimensional temperature distributions obtained from the reference charging cases discussed in Section 3.2. The reference packed-bed geometry, corresponding to $AR = H_{PB}/D_{PB} = 2.0$, $D_{PB} = 0.86$ m and $H_{PB} = 1.72$ m, was retained. Two initial thermal states were considered: the final field obtained after three hours of hysteresis-only charging at 80 Hz and approximately 2203 A, and the final field obtained after three hours of eddy-current-only charging at 50 kHz and 100 A. No electromagnetic heat source is active during discharge; the distinction between the two discharge cases therefore refers exclusively to the different thermal states produced during the preceding charging simulations.

It should be emphasised that these two initial states were obtained after the same charging duration, rather than under an equal charging-energy constraint. The different electrical operating points and the opposite transient evolution of the two induction sources therefore lead to different amounts and spatial distributions of sensible energy stored in the packed bed. In particular, the hysteresis-only case reaches a mean temperature of approximately 418 °C and a maximum temperature of approximately 446 °C, whereas the eddy-current-only case reaches a lower mean temperature of approximately 331 °C despite a comparable maximum temperature of approximately 435 °C. The latter consequently exhibits a more localised high-temperature region and a lower overall thermal level. The following discharge comparison should therefore be interpreted as an assessment of the consequences of these two reference charging states, rather than as an equal-energy comparison of the two heating mechanisms.

A preliminary mass-flow-rate sweep was performed in order to quantify this behaviour. Ambient air enters the packed bed at 20 °C and the total air mass-flow rate is divided equally between the two physical ends of the storage system, as described in Section 2.7. Total mass-flow rates between 0.20 and 4.00 kg/s were investigated over a two-hour discharge period. An outlet-air temperature of 300 °C was adopted as a reference level for useful high-temperature heat delivery. The principal simulation conditions are summarised in Table 3.3.

Parameter	**Value / investigated cases**
Initial solid-temperature field	Hysteresis-only and eddy-current-only final charging maps
Hysteresis-initialised T_{mean}	≈ 418 °C
Hysteresis-initialised T_{max}	≈ 446 °C
Eddy-initialised T_{mean}	≈ 331 °C
Eddy-initialised T_{max}	≈ 435 °C
Air inlet temperature	20 °C
Total air mass-flow rates	0.20, 0.50, 1.00, 1.50, 2.00, 3.00, 4.00 kg/s
Discharge duration	2 h
Reference outlet temperature	300 °C

Table 3.3– Initial thermal conditions and operating parameters adopted for the preliminary discharge mass-flow-rate analysis.

The first performance indicator considered is the outlet-air temperature, whose evolution for the investigated mass-flow rates is shown in Figure 3.12. A clear dependence on the imposed air flow is observed: increasing the mass-flow rate causes the outlet temperature to decrease more rapidly during discharge.

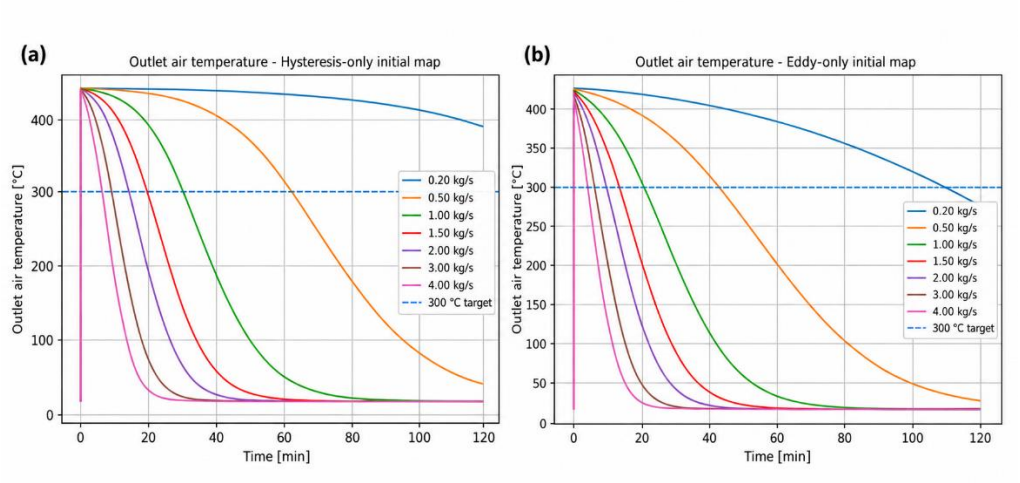


Figure 3.12– Outlet-air temperature evolution for different total air mass-flow rates using (a) the hysteresis-only and (b) the eddy-current-only final charging distributions as initial thermal states.

The trend observed in Figure 3.12 can be explained through the interaction between air residence time, local solid–fluid heat exchange and depletion of the stored sensible energy. As the mass-flow rate increases, the superficial mass flux through the packed bed also increases. According to the cell-by-cell NTU formulation introduced in Section 2.7, a higher mass flux reduces the local transfer-unit ratio associated with each axial cell, so that the temperature increase experienced by the flowing air within a given portion of the bed becomes smaller. At the same time, a larger amount of thermal energy is extracted from the solid per unit time, causing the storage material to cool more rapidly.

The consequence is a strong trade-off between air-flow rate and temperature sustainability. In the hysteresis-initialised case, a total mass-flow rate of 0.20 kg/s maintains the outlet temperature above the 300 °C reference level throughout the complete two-hour simulation. At 0.50 kg/s, the outlet temperature remains above 300 °C for approximately one hour but subsequently decreases rapidly. At 1.00 kg/s, the outlet temperature is already approximately 301 °C after 30 min and decreases to only 52 °C after 60 min.

The eddy-initialised packed bed exhibits a shorter useful high-temperature discharge. Even at the lowest investigated mass-flow rate of 0.20 kg/s, the outlet temperature decreases from approximately 413 °C after 30 min to 384 °C after 60 min and 278 °C after 120 min, falling below the adopted 300 °C reference before the end of the two-hour period. At 0.50 kg/s, the reduction is substantially faster, with the outlet temperature reaching approximately 204 °C after 60 min.

This difference should not be interpreted as an intrinsic difference in the discharge heat-transfer mechanism between hysteresis and eddy-current heating, since neither electromagnetic contribution is active during discharge. It results primarily from the different thermal states produced during charging. The hysteresis-initialised bed begins the discharge with a substantially higher mean temperature and a more spatially uniform distribution, allowing high-temperature air to be supplied for a longer period. The eddy-initialised case instead contains a comparable local maximum temperature but a much lower average thermal state, and therefore a smaller fraction of the packed-bed volume is available at sufficiently high temperature to sustain the outlet-air level.

The effect of mass-flow rate on outlet temperature must, however, be considered together with the corresponding thermal power delivered by the air stream.

The recovered thermal power predicted for the different mass-flow rates is shown in Figure 3.13. In contrast with the outlet-temperature behaviour, increasing the mass-flow rate produces a higher thermal-power output during the initial portion of the discharge.

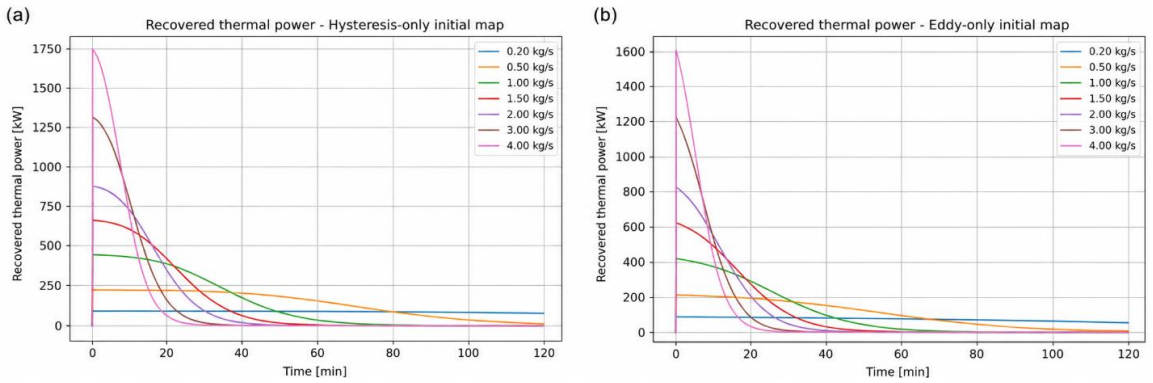


Figure 3.13– Recovered thermal-power evolution for different total air mass-flow rates using (a) the hysteresis-only and (b) the eddy-current-only final charging distributions as initial thermal states.

As shown in Figure 3.13, high mass-flow rates produce a larger initial recovered power because a greater air mass is heated and transported through the storage system per unit time. However, the higher extraction rate also removes sensible energy from the packed bed more rapidly. Consequently, the high-flow cases exhibit a pronounced decay in thermal power as the storage medium cools, eventually approaching the inlet-air condition and providing little additional useful heat.

Lower mass-flow rates display the opposite behaviour. The instantaneous recovered power is more moderate, but the packed bed cools more slowly and the thermal output can be sustained for a considerably longer period. The discharge process therefore cannot be characterised only by the magnitude of the peak or average recovered power: the temperature level at which this power is supplied is equally important for high-temperature process-heat applications.

The main quantitative results from the mass-flow sweep are summarised in Table 3.4.

Initial state	$\dot{m}_{total}$ **[kg/s]**	T_{out},30min **[°C]**	T_{out},60min **[°C]**	T_{out},120min **[°C]**	$P_{mean,120min}$ **[kW]**	$E_{rec,120min}$ **[kWh]**
Hysteresis	0.20	443	437	391	85	170
Hysteresis	0.5	427	316	43	133	267
Hysteresis	1.0	301	52	20	135	270
Eddy	0.2	413	384	278	73	145
Eddy	0.5	359	204	31	100	201

Table 3.4– Selected quantitative results from the preliminary discharge mass-flow-rate sweep, including outlet-air temperature, mean recovered thermal power and cumulative recovered energy over the two-hour simulation period.

Table 3.4 illustrates the distinction between total energy recovery and useful temperature duration. For the hysteresis-initialised case, increasing the mass-flow rate from 0.20 to 0.50 kg/s increases the recovered energy over two hours from approximately 170 to 267 kWh and the

corresponding mean thermal power from 85 to 133 kW. However, this increase is accompanied by a substantial reduction in outlet-air temperature: after 120 min, the 0.50 kg/s case supplies air at only approximately 43 °C, compared with 391 °C for the 0.20 kg/s case.

The same behaviour becomes even more evident at 1.00 kg/s. The two-hour recovered energy reaches approximately 270 kWh, only slightly above that obtained at 0.50 kg/s, while the outlet temperature falls to approximately 52 °C after one hour and approaches the inlet condition after two hours. Therefore, although a larger fraction of the stored sensible energy is extracted within the fixed two-hour window, most of the later thermal output is delivered at a temperature that is no longer representative of the high-temperature application considered in this analysis.

The eddy-initialised results show the same qualitative trade-off but start from a less favourable thermal condition. At 0.20 kg/s, approximately 145 kWh are recovered over two hours with a mean power of 73 kW, but the outlet temperature has already decreased below the 300 °C reference level by the end of the simulation. Increasing the flow to 0.50 kg/s raises the two-hour recovered energy to approximately 201 kWh, while reducing the outlet temperature to approximately 204 °C after only one hour and 31 °C after two hours.

These results demonstrate that cumulative recovered energy alone is not sufficient to assess discharge performance. A larger energy recovery over a prescribed time interval can be obtained by extracting the stored energy more rapidly, but this may simultaneously reduce the duration for which the system provides heat at a useful temperature. The performance of the packed bed must therefore be evaluated by considering temperature quality and thermal-power delivery simultaneously.

To combine these two performance requirements, Figure 3.14 compares the outlet-air temperature after 60 min of discharge with the mean recovered thermal power over the first hour. The 300 °C reference temperature is included to distinguish operating conditions that can still provide high-temperature air after one hour from those in which the packed bed has already cooled below the adopted useful-temperature level.

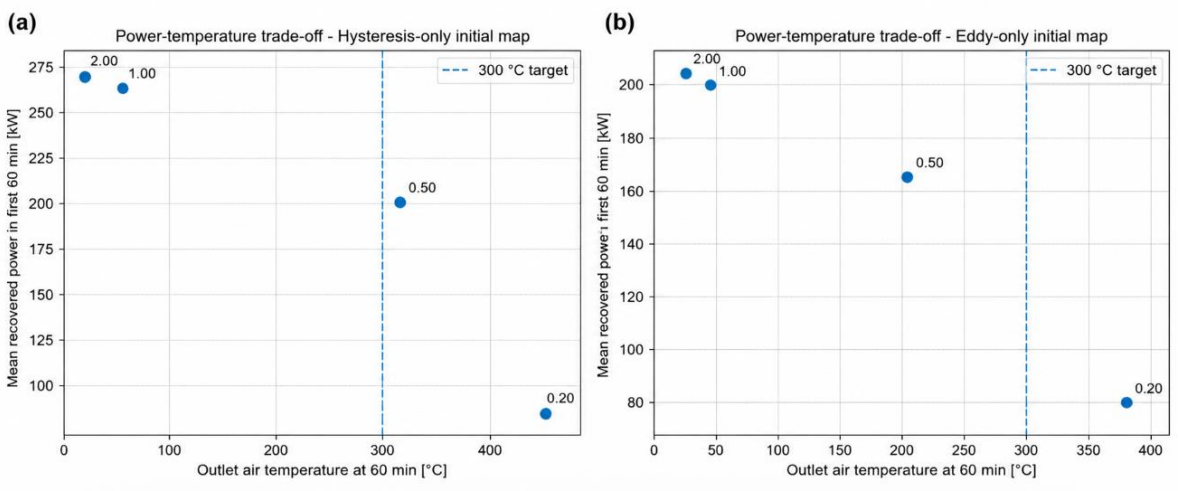


Figure 3.14– Trade-off between outlet-air temperature after 60 min of discharge and mean recovered thermal power during the first hour for the investigated total mass-flow rates. The 300 °C reference level identifies the operating conditions that maintain high-temperature thermal delivery after one hour.

Figure 3.14 summarises this trade-off: 0.20 kg/s provides the greatest temperature sustainability, whereas 0.50 kg/s offers a higher thermal-power output at the expense of a shorter high-temperature discharge.

On the basis of this preliminary analysis, a total air mass-flow rate of

$$\dot{m}_{total} = 0.20\ kg/s$$

was selected for the repeated charge–discharge simulations presented in the following section. This operating condition was chosen because it provides the most stable high-temperature outlet among the investigated flow rates and therefore allows the cyclic analysis to focus on the amount of useful heat recovered before the outlet temperature falls below the prescribed 300 °C threshold.

It should be emphasised that the selected value does not represent a general optimum discharge flow rate for IH-PBTES systems. The preferred operating condition depends on the required thermal-power level, delivery temperature, discharge duration and packed-bed thermal state. The present mass-flow sweep instead provides a consistent basis for selecting a representative operating condition for the subsequent cyclic analysis.

The results of the standalone discharge simulations consequently establish the connection between the thermal field produced during charging and the useful energy subsequently delivered by the storage system. The following section extends this analysis to repeated operation, in which the residual two-dimensional temperature distribution remaining after each useful discharge is retained and used directly as the initial condition of the subsequent charging phase.

3.5 Charge-Discharge Cycles

Following the standalone analyses, the charging and discharging models were coupled according to the cyclic procedure described in Section 2.8. Each cycle is initialised from the residual two-dimensional temperature field produced by the preceding discharge, while the isolated hysteresis and eddy-current source modes are retained solely for diagnostic comparison.

The discharge conditions were kept identical for all cyclic simulations. Air entered the packed bed at 20 °C with a total mass-flow rate of 0.20 kg/s, selected on the basis of the preliminary discharge analysis presented in Section 3.4. Each discharge phase was continued until the outlet-air temperature decreased below the prescribed useful-temperature threshold of 300 °C, after having first reached or exceeded this value. A maximum packed-bed temperature of 650 °C was also imposed during charging as a numerical safety limit.

Two charging strategies were investigated. In the first strategy, the target electrical energy supplied to the coil was fixed at 300 kWh for each cycle. In the second strategy, charging was instead continued until a target volume-averaged packed-bed temperature of 400 °C was reached. The principal operating conditions are summarised in Table 3.5.

Parameter	**Value**
Number of consecutive cycles	3
Initial temperature, Cycle 1	20 °C
Total discharge air mass-flow rate	0.20 kg/s
Air inlet temperature	20 °C
Useful outlet-temperature threshold	300 °C
Charging safety temperature	650 °C
Same-energy target	300 kWh
Same-mean-temperature target	400 °C
Electrical input boundary	Induced energy + coil losses
Converter losses	Excluded

Table 3.5– Main operating conditions adopted for the repeated charge–discharge cycle simulations.

Unless otherwise specified, the efficiency values reported in the present cyclic analysis refer to the round-trip efficiency η_{RT} defined in Eq. (2.107), rather than to the charging efficiency η_{ch} used in Sections 3.2 and 3.3. Accordingly, the converter losses included in the definition of η_{ch} are excluded from the charging-energy denominator adopted for the cyclic calculations.

The first cyclic strategy was based on a prescribed electrical charging-energy target of 300 kWh. The electrical input is evaluated at the coil boundary and therefore includes both the energy

transferred to the packed bed by induction and the resistive losses occurring in the coil, while converter losses are not included.

The hysteresis-only case successfully reaches the 300 kWh target in all three cycles. The first cycle starts from the completely cold state and therefore differs significantly from the subsequent cycles, which benefit from the residual sensible energy remaining in the packed bed after the preceding discharge. During Cycle 1, 160.5 kWh are recovered as useful thermal energy, corresponding to a round-trip efficiency of approximately 53.5%. In Cycles 2 and 3, the recovered energy increases to approximately 223.1 and 216.2 kWh, respectively, resulting in round-trip efficiencies of approximately 74.4% and 72.1%.

The main quantitative results for the same-energy simulations are summarised in Table 3.6.

Case	**Cycle**	E_{input} [kWh]	$E_{coil,loss}$ [kWh]	$T_{mean,end,ch}$ [°C]	$T_{max,end,ch}$ [°C]	E_{rec} [kWh]
Hysteresis	1	300.0	59.0	359.6	395.1	160.5
Hysteresis	2	300.0	73.5	426.3	≈480	223.1
Hysteresis	3	300.0	71.6	419.0	≈475	216.2
Eddy	1	300.0	5.4	418.3	550.5	217.9
Eddy	2	189.7	2.9	360.6	650.0	175.4
Eddy	3	191.6	2.9	363.4	650.0	177.3

Table 3.6– Main charging and energy-recovery results for the three consecutive cycles performed using the same electrical-energy-input strategy.

The energy distribution over the three hysteresis-only cycles is shown in Figure 3.15. The first cycle exhibits the largest fraction of unrecovered energy, equal to approximately 26.8% of the electrical input. Once the system has completed the first charge–discharge sequence, the residual thermal state strongly modifies the subsequent energy balance. In Cycle 2, approximately 74.4% of the electrical input is recovered as useful heat, while only approximately 1.1% remains in the unrecovered-energy category. Cycle 3 shows a very similar energy partition, with approximately 72.1% useful recovered energy and 4.1% unrecovered energy.

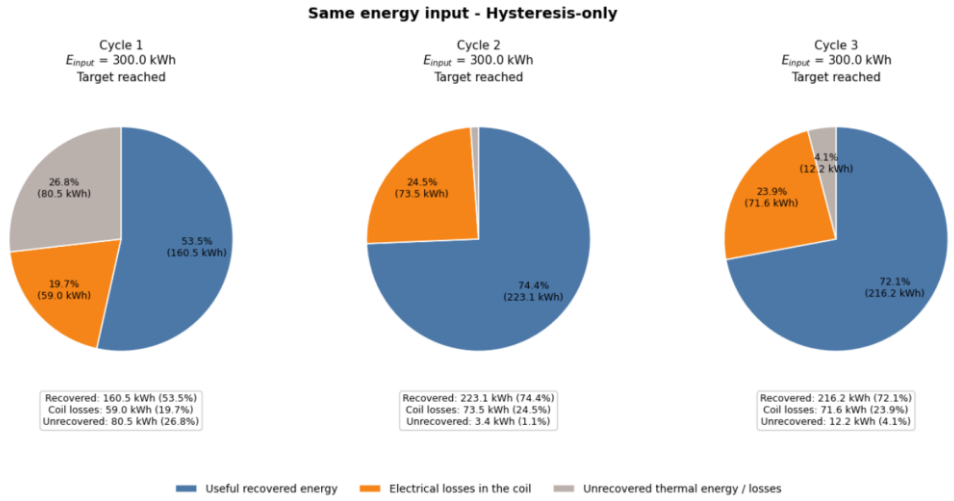


Figure 3.15– Electrical-energy balance over three consecutive hysteresis-only cycles performed with a target electrical input of 300 kWh per charging phase. Useful recovered energy, coil electrical losses and unrecovered thermal energy are reported for each cycle.

The term “unrecovered thermal energy / losses” shown in Figure 3.15 should not be interpreted as a direct measurement of heat losses to the surroundings alone. According to the cycle-level energy balance defined in Section 2.8, it is a balance remainder obtained after subtracting the useful recovered energy and the coil electrical losses from the supplied electrical energy. It therefore accounts for the environmental thermal losses occurring during the cycle together with the net change in sensible energy stored in the packed bed between the beginning and the end of that cycle. The discharge simulation itself is terminated as soon as the outlet-air temperature falls below the adopted 300 °C threshold; energy delivery below this temperature is therefore not simulated as a separate contribution. The much smaller unrecovered fractions obtained in Cycles 2 and 3 indicate that, after the initial cold-start cycle, the residual thermal state approaches a more repeatable cyclic condition. Consequently, the net change in sensible energy stored in the packed bed becomes comparatively small, and the balance remainder is increasingly dominated by thermal losses rather than by accumulation of residual sensible energy.

A different behaviour is observed for the eddy-current-only case. Cycle 1 reaches the prescribed electrical-energy target of 300 kWh and recovers approximately 217.9 kWh, corresponding to a round-trip efficiency of approximately 72.6%. In Cycles 2 and 3, however, charging is terminated before reaching the 300 kWh target because the local maximum packed-bed temperature reaches the prescribed safety limit of 650 °C. The actual electrical inputs are consequently reduced to approximately 189.7 and 191.6 kWh.

The corresponding energy balances are shown in Figure 3.16.

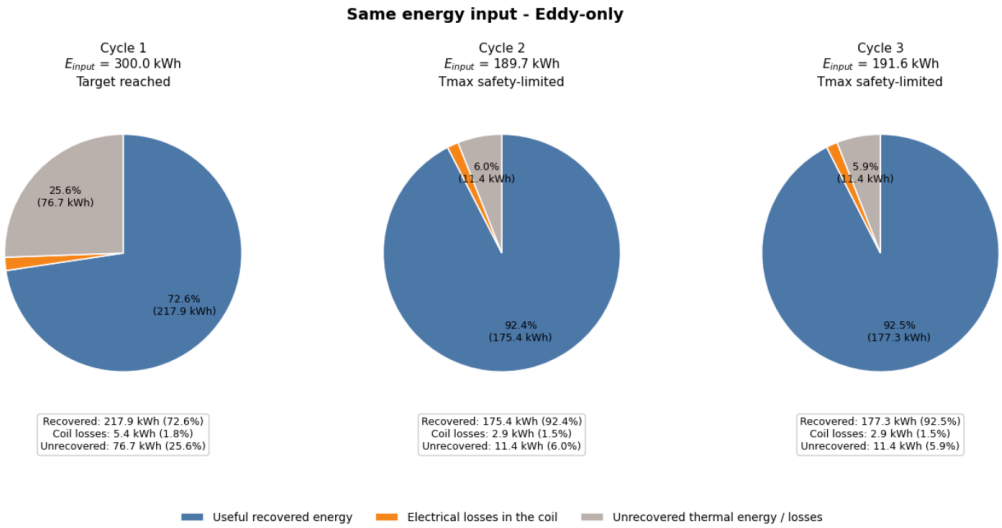


Figure 3.16– Electrical-energy balance over three consecutive eddy-current-only cycles under the same-energy-input charging strategy. Cycles 2 and 3 are terminated by the 650 °C maximum-temperature safety limit before the nominal 300 kWh charging target is reached.

The apparent round-trip efficiencies of approximately 92.4% and 92.5% obtained in eddy-current Cycles 2 and 3 must therefore be interpreted with particular caution. These values do not indicate that the eddy-current case is intrinsically more efficient than the corresponding hysteresis-only cycles under equivalent charging conditions. The denominator in the efficiency definition is the actual electrical energy supplied during charging, which is substantially lower in the safety-limited cycles. Consequently, the high percentage reflects a different charging termination condition rather than superior performance at the same energy input.

At the same time, the eddy-current cycles confirm the thermal-localisation tendency identified in the standalone charging analysis. Residual heat from the preceding cycle increases the initial packed-bed temperature, and the positive temperature dependence of the eddy-current source promotes additional local heating. As a consequence, the 650 °C limit is reached increasingly before the nominal energy target can be supplied.

A second cyclic strategy was investigated by replacing the fixed electrical-energy target with a prescribed volume-averaged packed-bed temperature of 400 °C. This approach allows the electrical energy required to establish a nominally equivalent average thermal state to be compared between consecutive cycles.

The principal evolution of the cyclic performance indicators is reported in Figure 3.17. For the hysteresis-only case, the electrical energy required to reach the 400 °C mean-temperature target decreases substantially after the first cycle, from approximately 348.7 kWh in Cycle 1 to 272.2 and 271.8 kWh in Cycles 2 and 3. This reduction results from the residual sensible energy retained after discharge, which provides a warmer initial condition for the subsequent charging phases.

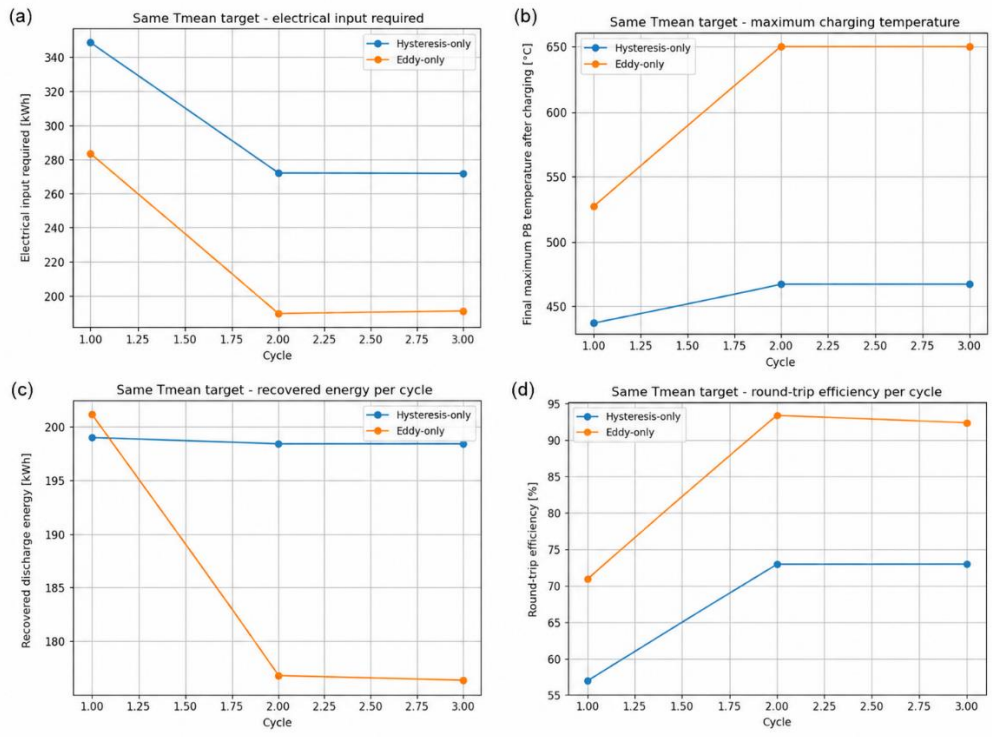


Figure 3.17– Evolution of the principal cyclic performance indicators under the same mean packed-bed temperature target: (a) electrical charging energy, (b) maximum packed-bed temperature at the end of charging, (c) useful recovered energy and (d) round-trip efficiency.

For the hysteresis-only case, Figure 3.17 shows a clear stabilisation between Cycles 2 and 3. Both cycles require approximately 272 kWh of electrical input and a charging duration of approximately 2.33 h to reach the prescribed 400 °C mean temperature. The useful recovered energy remains almost unchanged at approximately 198.4 kWh, while the round-trip efficiency stabilises close to 73%. The maximum packed-bed temperature also converges to approximately 465 °C.

Cycle 1 differs because it begins from the uniformly cold state and consequently requires approximately 348.7 kWh to reach the same mean temperature. Despite achieving an equivalent volume-averaged final temperature, its round-trip efficiency is lower, approximately 57.1%, because a larger amount of electrical energy is required to establish the thermal inventory of the initially cold packed bed.

The quantitative results are summarised in Table 3.7.

Case	Cycle	E_{input} [kWh]	Charging time [h]	$T_{mean,end,ch}$ [°C]	$T_{max,end,ch}$ [°C]	E_{rec} [kWh]
Hysteresis	1	348.66	2.716	400.00	430.94	198.92
Hysteresis	2	272.19	2.333	400.00	464.63	198.39
Hysteresis	3	271.85	2.331	400.00	464.53	198.38
Eddy	1	283.69	3.455	400.00	526.17	200.99

Eddy	2	189.88	1.921	362.83	650.00	177.37
Eddy	3	191.46	1.945	363.01	650.00	176.94

Table 3.7– Main charging and energy-recovery results for the three consecutive cycles performed using a 400 °C mean packed-bed temperature target.

The hysteresis-only energy balances associated with this strategy are shown in Figure 3.18. The useful recovered-energy fraction increases from approximately 57.1% in Cycle 1 to 72.9% and 73.0% in Cycles 2 and 3, respectively. The nearly identical energy partitions obtained in the final two cycles provide further evidence of the approach towards a quasi-cyclic operating condition.

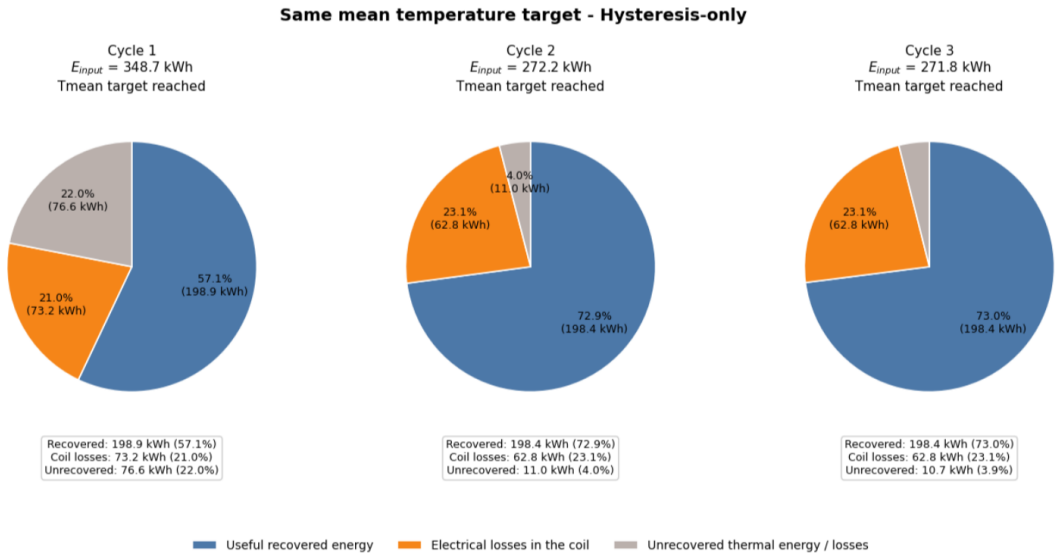


Figure 3.18– Electrical-energy balance over three consecutive hysteresis-only cycles performed using a mean packed-bed charging-temperature target of 400 °C.

The eddy-current-only case behaves differently. During Cycle 1, the system successfully reaches the 400 °C mean-temperature target after approximately 3.46 h of charging, requiring approximately 283.7 kWh of electrical energy. The corresponding maximum temperature is already considerably higher than the mean value, reaching approximately 526 °C, which reflects the stronger spatial localisation associated with the eddy-current source.

In Cycles 2 and 3, the prescribed mean-temperature target can no longer be reached. Charging is terminated when the local maximum temperature reaches the 650 °C safety limit, while the volume-averaged temperature is still only approximately 363 °C. Consequently, Cycles 2 and 3 receive approximately 190 kWh of electrical input and recover approximately 177 kWh of useful thermal energy.

The energy balances are reported in Figure 3.19.

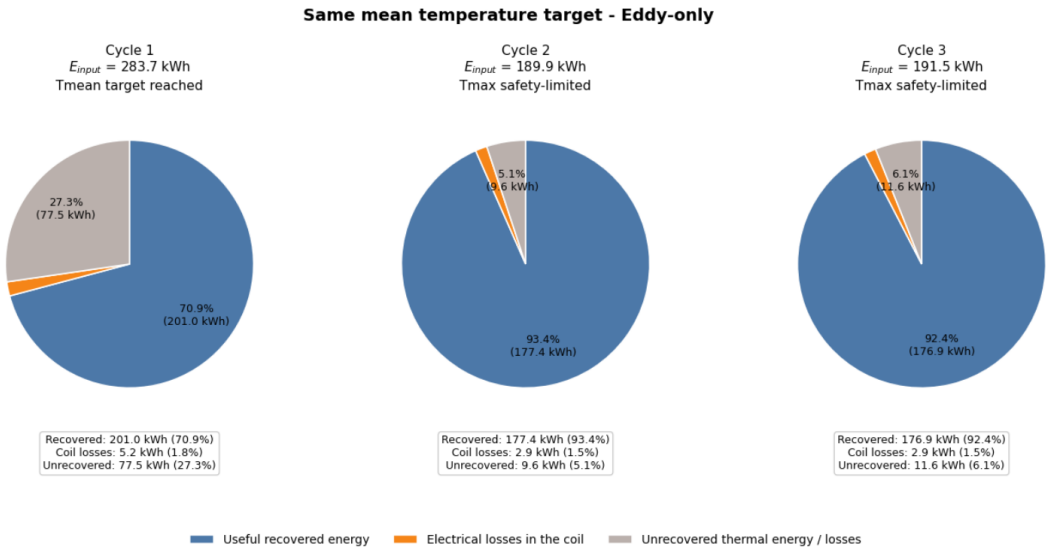


Figure 3.19 – Electrical-energy balance over three consecutive eddy-current-only cycles under the 400 °C mean-temperature charging strategy. Cycles 2 and 3 are terminated by the 650 °C local maximum-temperature limit before reaching the prescribed mean-temperature target.

As in the same-energy analysis, the round-trip efficiencies above 92% obtained in Cycles 2 and 3 should not be interpreted as evidence of superior overall cyclic performance. The main reason for the high values is the very small contribution of coil Joule losses in the eddy-current operating condition. In Cycles 2 and 3, the coil losses are only approximately 2.9 kWh, corresponding to about 1.5% of the electrical charging input, whereas the corresponding hysteresis-only cycles exhibit coil losses of approximately 62.8 kWh. The earlier safety-limited termination, and consequently the lower actual charging energy, contributes only secondarily to the resulting efficiency values. More importantly, Cycles 2 and 3 do not reach the intended thermal target: charging is terminated when the local maximum temperature reaches 650 °C while the mean packed-bed temperature is only approximately 363 °C, about 37 °C below the prescribed 400 °C value. The same-mean-temperature strategy therefore emphasises the principal limitation identified for the isolated eddy-current contribution. A high local temperature can develop even when the average packed-bed temperature remains substantially lower.

The global energy indicators describe the cyclic performance of the system but do not reveal how the spatial thermal state evolves between successive cycles. Since the residual two-dimensional temperature distribution is explicitly propagated from one cycle to the next, the spatial evolution is an essential component of the cyclic analysis. The final charging-temperature distributions obtained under the same-mean-temperature strategy are therefore compared in Figure 3.20.

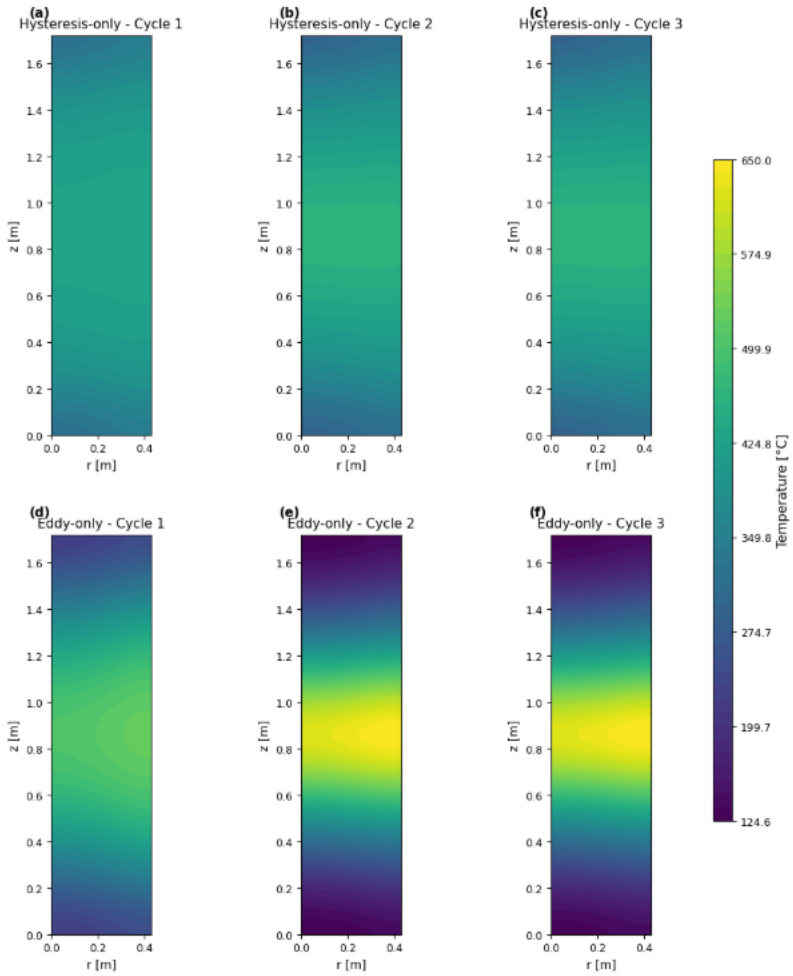


Figure 3.20– Final two-dimensional packed-bed temperature distributions at the end of charging over three consecutive cycles using the same mean-temperature strategy: (a–c) hysteresis-only Cycles 1–3 and (d–f) eddy-current-only Cycles 1–3.

The hysteresis-only maps in Figure 3.20 show that the thermal field evolves from the first initially cold cycle towards a repeatable spatial distribution. Although Cycle 1 reaches the same 400 °C mean-temperature target as the following cycles, its temperature field differs because it originates from a uniform 20 °C initial state. In Cycles 2 and 3, the residual thermal distribution inherited from the preceding discharge modifies the subsequent charging process, and the final temperature maps become nearly indistinguishable. This spatial convergence is consistent with the stabilisation of electrical input, recovered energy and round-trip efficiency observed in Figure 3.17.

The eddy-current maps exhibit a markedly different evolution. Cycle 1 reaches the 400 °C mean-temperature target but already develops a pronounced central high-temperature region. In Cycles 2 and 3, the combination of the inherited residual temperature field and the positive thermo-electromagnetic feedback of the eddy-current source intensifies this localisation. The local temperature reaches the 650 °C safety limit before the volume-averaged temperature reaches the target value, resulting in the safety-limited charging behaviour identified previously.

The residual temperature fields remaining after useful discharge are shown in Figure 3.21.

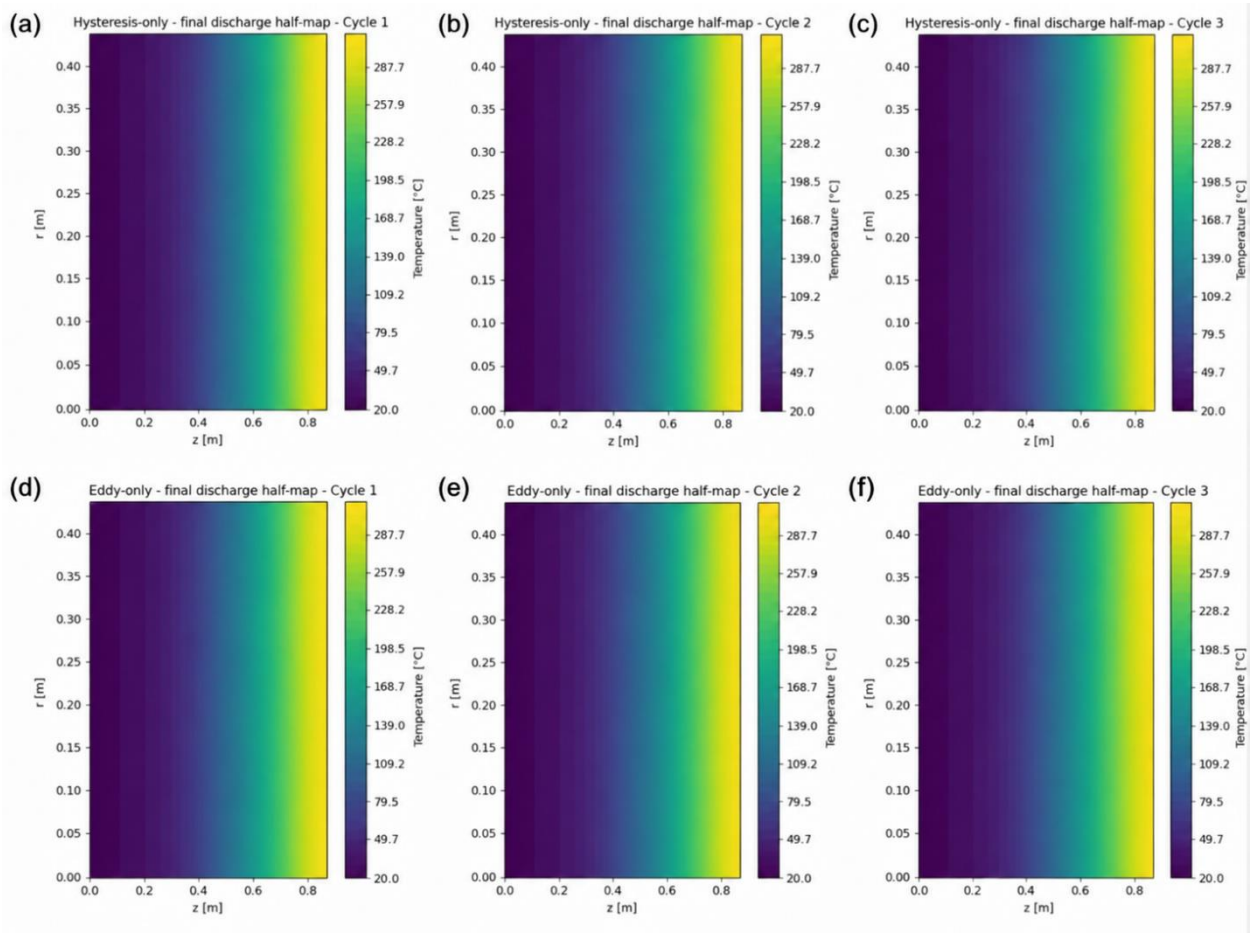


Figure 3.21– Residual two-dimensional temperature distributions at the end of useful discharge over three consecutive cycles: (a–c) hysteresis-only Cycles 1–3 and (d–f) eddy-current-only Cycles 1–3. The maps represent the simulated discharge half-domain, extending along the axial coordinate zfrom the physical air inlet at $z = 0$to the central outlet plane at $z = H_{PB}/2$.

Figure 3.21 confirms that termination of the discharge at the 300 °C outlet-temperature threshold does not correspond to complete thermal depletion of the packed bed. A considerable amount of sensible energy remains stored in the solid when the useful discharge criterion is reached. The residual temperature field is characterised predominantly by an axial gradient, with temperature increasing from the physical air inlet towards the central outlet plane. At a given axial position, the temperature varies only weakly along the radial direction r, as indicated by the nearly uniform colour distribution across the packed-bed radius. The residual thermal non-uniformity is therefore mainly axial rather than radial. This remaining spatial temperature distribution provides the non-uniform initial condition for the following charging phase.

Despite the substantially different charging-temperature fields, the residual distributions obtained after discharge become considerably more similar. This behaviour results from the common discharge operating conditions and from the identical outlet-temperature cutoff applied to all cycles. Nevertheless, the packed bed is not reset to the ambient condition, and the remaining thermal inventory is sufficiently large to reduce the charging energy required in the subsequent cycle.

The similarity of the residual maps between Cycles 2 and 3 provides additional evidence of the approach towards a quasi-cyclic state. In particular, the hysteresis-only residual thermal condition changes only marginally between the final two cycles, consistently with the nearly identical charging and energy-performance indicators.

The evolution of the outlet-air temperature during the three cyclic discharges is shown in Figure 3.22.

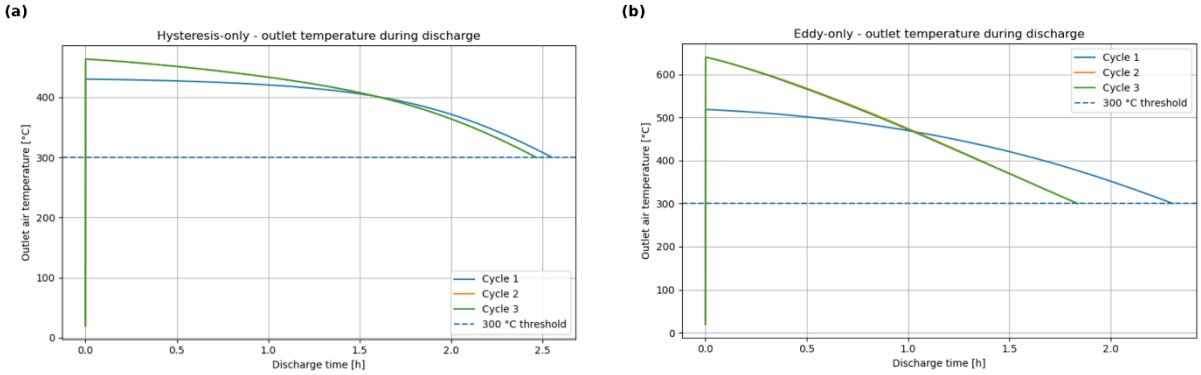


Figure 3.22– Outlet-air temperature evolution during the discharge phase of three consecutive cycles for (a) the hysteresis-only and (b) the eddy-current-only cases under the same mean-temperature charging strategy. The dashed line represents the 300 °C useful-discharge threshold.

For the hysteresis-only case, Figure 3.22(a) shows that Cycles 2 and 3 produce almost overlapping outlet-temperature curves, while Cycle 1 exhibits a slightly different discharge history. This behaviour is consistent with the stabilisation of the final charging and residual temperature fields and provides a dynamic indication that the system is approaching repeatable cyclic operation.

A similar convergence between Cycles 2 and 3 is observed in the eddy-current case, as shown in Figure 3.22(b). However, the reason for this apparent repeatability differs from the hysteresis-only case. The final two eddy-current charging phases are both constrained by the same 650 °C local safety limit rather than by successful achievement of the prescribed 400 °C mean-temperature target. The similarity between their discharge curves therefore represents repeatability of a safety-limited operating condition rather than successful convergence to the intended charging strategy.

Overall, the cyclic simulations demonstrate the importance of retaining the residual spatial temperature field between consecutive charge and discharge phases. The first cycle, which starts from a uniform ambient state, is not representative of the subsequent repeated operation of the storage system. Once residual thermal energy is propagated between cycles, the hysteresis-only simulations rapidly approach a stable response in terms of charging energy, recovered energy, temperature distribution and round-trip efficiency.

The isolated eddy-current simulations also exhibit close agreement between Cycles 2 and 3, but strong local temperature amplification prevents the intended charging targets from being maintained during repeated operation. In both investigated charging strategies, the local 650 °C temperature limit becomes active from the second cycle onward. This result reinforces the importance of resolving local temperatures rather than relying exclusively on volume-averaged thermal indicators when evaluating repeated IH-PBTES operation.

Three cycles are sufficient to identify a clear tendency towards repeatable behaviour but are not sufficient to establish a mathematically periodic steady state. The results should therefore be interpreted as evidence of an approach to quasi-cyclic operation, rather than proof of complete cyclic convergence.

4. Discussion

4.1 Comparison of Charging Mechanisms

The isolated hysteresis and eddy-current simulations were used to identify the characteristic thermo-electromagnetic behaviour associated with the two induction-heating contributions. As discussed in Section 2.2, these cases are diagnostic rather than alternative operating strategies, since both mechanisms would occur simultaneously in a real IH-PBTES system. The main differences observed in the simulations are summarised in Table 4.1.

Aspect	Hysteresis-only case	Eddy-current-only case
Temperature dependence of heat generation	Decreases as temperature increases	Increases locally with temperature within the implemented conductivity range
Thermo-electromagnetic feedback	Negative	Positive
Thermal behaviour	Partially self-regulating	Tendency towards amplification of initially hotter regions
Spatial temperature uniformity	More controlled	Greater localisation
Hot-spot tendency	Lower	Higher
Coil current under investigated conditions	Higher	Lower
Coil resistive losses	Higher	Lower
Electrical charging performance	Less favourable	More favourable
Main advantage	Better thermal controllability	Lower coil losses and stronger electrical performance
Main limitation	High current and associated coil losses	Local overheating and larger temperature gradients

Table 4.1– Qualitative comparison of the isolated hysteresis and eddy-current heating contributions investigated in this work.

Within the operating conditions and material-property formulation adopted in this work, the hysteresis contribution progressively decreases as the packed-bed temperature increases. This produces a negative thermo-electromagnetic feedback that partially limits the amplification of local temperature differences. Conversely, the eddy-current contribution exhibits a positive feedback: the increase in the adopted electrical conductivity of magnetite with temperature strengthens heat generation in warmer regions, promoting greater spatial localisation. The

importance of temperature-dependent electromagnetic properties in induction-heating simulations has also been highlighted in previous coupled electromagnetic–thermal studies [57], [59].

The comparison therefore reveals a trade-off between electrical charging performance and thermal controllability. The eddy-current-only case operates with a substantially lower coil current and correspondingly lower resistive coil losses, but it develops stronger temperature gradients and a greater tendency towards local overheating. The hysteresis-only case requires a higher coil current under the investigated conditions but produces a more controlled spatial temperature distribution. Similar non-uniform thermal behaviour has been observed experimentally in other inductively heated packed structures [60].

Consequently, IH-PBTES charging performance should not be evaluated on electromagnetic efficiency alone. Electrical losses, heating intensity, temperature uniformity, maximum local temperature and operational stability must be considered simultaneously. In a practical system, hysteresis and eddy-current losses would coexist at the same operating point; the actual thermal response would therefore result from their interaction rather than from either isolated mechanism considered independently.

4.2 Implications for IH-PBTES Design and Operation

The numerical results obtained in this work show that the design of an IH-PBTES cannot be approached as the independent optimisation of an induction-heating system and a conventional packed-bed thermal store. The direct generation of heat within the storage material couples electromagnetic, geometrical and operational variables. Frequency, current amplitude and coil configuration determine the magnitude and spatial distribution of the induced heat source, whereas packed-bed geometry, material properties, heat losses and discharge conditions determine how the generated energy is distributed, retained and ultimately recovered. Consequently, the design objective should not be the maximisation of a single performance indicator, but rather the identification of an operating region that provides adequate electromagnetic coupling while preserving thermal uniformity, useful energy recovery and safe cyclic operation. The main trade-offs identified in this work are summarised in Table 4.2.

Design / operating variable	Main effect	Main trade-off	Design implication
Coil configuration, current and frequency	Control heating intensity and spatial heat-source distribution	Higher induced power may increase temperature non-uniformity	Electrical performance and thermal uniformity should be optimised together
Packed-bed aspect ratio	Modifies field distribution, temperature gradients and charging behaviour	No single geometry improves all performance indicators	Geometry should be treated as a multi-objective design variable
Air mass-flow rate	Controls heat-extraction rate during discharge	Higher thermal power is obtained at the expense of outlet temperature and useful discharge duration	Flow rate should depend on process temperature and power demand
Charging target	Defines the desired state of charge	Global targets may conceal local overheating	Mean-temperature or energy targets should be combined with local constraints
Maximum-temperature limit	Prevents excessive local temperatures	Charging may terminate before the global target is reached	Local temperature monitoring is necessary
Discharge cutoff temperature	Defines the useful heat-delivery window	Higher cutoff temperature improves heat quality but reduces recoverable energy	The threshold should be application-dependent
Residual thermal state	Alters the following charging phase	Cold-start behaviour differs from repeated operation	Cyclic thermal history must be included in performance assessment
Cycle duration and stopping criteria	Affect utilisation and long-term repeatability	Fixed operating criteria may be sub-optimal under variable conditions	Adaptive charging and discharge control should be considered

Table 4.2– Summary of the main design and operational trade-offs identified for the IH-PBTES system.

A first implication concerns the electromagnetic design of the charging system. The results presented in Chapter 3 show that the spatial distribution of the induced heat source is at least as important as its integral magnitude. Increasing the electromagnetic power deposited in the packed bed does not necessarily improve storage performance if the additional heat generation is concentrated within a limited region. Coil design and excitation conditions should therefore be selected by considering temperature uniformity together with heating rate and electrical efficiency. Nian et al. [61] showed that coil position, coil-turn pitch, heating distance and operating frequency can substantially affect both heating rate and temperature uniformity, with coil position playing a particularly important role in determining the spatial thermal response.

Experimental results reported by Wei et al. [62] further support this coupled interpretation. Their study showed that geometrical modifications can alter the paths followed by induced eddy currents and consequently affect both heating efficiency and the spatial distribution of heat generation. Importantly, improvements in temperature uniformity may be accompanied by a

reduction in electromagnetic efficiency, although appropriate structural design can partially reconcile the two objectives. Although the configurations investigated in [62] differ from the present packed-bed system, the broader implication is directly relevant to IH-PBTES: electromagnetic efficiency and thermal uniformity should be treated as coupled design objectives. Future optimisation should therefore include not only excitation frequency and current, but also the relative geometry and arrangement of the coil and packed bed.

The aspect-ratio analysis performed in this work leads to a similar conclusion from the storage-design perspective. No single geometrical configuration was found to improve all investigated performance indicators simultaneously, since changes in aspect ratio modify electromagnetic requirements, heat-source localisation, temperature non-uniformity and charging performance in different ways. Aspect ratio should therefore be treated as part of a broader multi-objective design problem rather than selected according to a single electromagnetic or thermal criterion.

This interpretation is consistent with previous optimisation studies on packed-bed thermal storage. Marti et al. [63] simultaneously optimised exergy efficiency and material cost using packed-bed height, radii, insulation thickness and particle diameter as design variables, obtaining a Pareto set rather than a unique optimum. Their analysis showed that a configuration close to the maximum achievable efficiency could be obtained at substantially lower material cost, illustrating the importance of accepting controlled compromises between competing objectives.

The influence of aspect ratio must nevertheless be interpreted in relation to the specific storage concept and operating conditions. Krüger et al. [64], analysing a large stratified sensible-heat storage system, found that increasing the aspect ratio improved thermal stratification and increased the usable fraction of the storage volume, while simultaneously increasing environmental heat losses and reducing exergetic performance. The physical system considered in [64] differs substantially from the induction-heated magnetite packed bed investigated here, and the reported trends should therefore not be transferred quantitatively to the present configuration. Nevertheless, the study reinforces the broader conclusion that geometrical changes generally introduce competing effects rather than a universally favourable trend.

The same multi-objective perspective becomes even more important when moving towards industrial implementation. Le Roux et al. [65] optimised a high-temperature thermocline storage system by simultaneously considering exergy efficiency, environmental impact and life-cycle cost. Their results showed that the geometry favoured by one objective was not necessarily that favoured by another, and that practical design requires a compromise between competing criteria. An analogous principle applies to IH-PBTES, with the additional need to include electromagnetic

variables. A future optimisation framework could therefore consider charging efficiency, recoverable thermal energy, temperature non-uniformity, maximum local temperature and electrical losses, while practical constraints such as storage capacity, material cost and installation geometry would define the feasible design space.

The discharge results introduce an additional operational trade-off. Increasing the air mass-flow rate increases instantaneous thermal-power extraction and accelerates energy recovery, but simultaneously reduces the outlet-air temperature and shortens the duration of useful high-temperature heat delivery. Discharge performance should therefore not be evaluated solely in terms of recovered energy or thermal power, since the temperature level and duration of heat delivery are equally important for industrial process-heat applications. The total mass-flow rate of 0.20 kg/s adopted for the cyclic simulations should consequently be interpreted as a representative condition selected to favour high-temperature delivery rather than as a universal optimum. In practical operation, the air mass-flow rate could instead be treated as an active control variable and adjusted according to process-temperature requirements, thermal-power demand and the instantaneous thermal state of the packed bed.

Repeated operation introduces a further design dimension because the residual thermal state after discharge influences the subsequent charging phase. The cyclic simulations show that cold-start behaviour is not necessarily representative of repeated operation and that charging and discharge stopping criteria should therefore be regarded as operational design variables rather than merely numerical termination conditions. Ortega-Fernández et al. [66] reached a similar conclusion for conventional packed-bed TES by comparing complete charge/discharge operation, fixed-duration operation and strategies based on prescribed outlet-temperature variation. Their results showed that the selected thermal-management strategy strongly affects both cycle efficiency and utilisation of the storage material.

This consideration is particularly relevant for IH-PBTES because the residual thermal field affects not only the amount of sensible energy already stored, but also the subsequent temperature-dependent electromagnetic heat generation. The present simulations indicate the value of combining global state-of-charge indicators with local constraints: mean packed-bed temperature or electrical energy input can define the desired charging state, whereas a maximum-temperature criterion can protect the system against excessive local overheating. During discharge, an outlet-temperature threshold provides a direct measure of the useful quality of the recovered heat. A practical control architecture could therefore combine average-temperature or energy-based state-of-charge indicators with local temperature monitoring and outlet-temperature control, particularly

under variable renewable-electricity availability, for which charging periods are unlikely to remain identical from one cycle to the next.

The importance of accounting for variable cyclic operation is further supported by McTigue et al. [67], who investigated packed-bed thermal storage under perturbations in charge duration. Their results showed that deviations from the nominal cycle can influence subsequent performance and that several additional cycles may be required before the previous periodic behaviour is recovered. They also found that outlet-temperature-based control can reduce the effect of such perturbations. These findings provide useful context for the three-cycle analysis performed in this thesis. The similarity observed between the second and third hysteresis-only cycles indicates an approach towards repeatable operation, but does not demonstrate that a true periodic steady state has been reached. An IH-PBTES intended to operate under fluctuating electricity supply should therefore ultimately be assessed over longer and non-uniform sequences of charge-discharge cycles.

Taken together, these results indicate that future IH-PBTES optimisation should be formulated as a coupled and multi-objective problem. At the electromagnetic level, current, frequency and coil configuration determine the magnitude and spatial distribution of induction heating. At the storage level, packed-bed geometry, particle properties and insulation influence temperature redistribution and heat retention. At the operational level, charging targets, maximum-temperature constraints, discharge flow rate and useful outlet-temperature thresholds determine how effectively the stored energy can be exploited over repeated cycles. Optimising only one of these levels may simply shift losses or limitations to another part of the system.

Accordingly, the most appropriate design strategy is not necessarily the one that maximises instantaneous induction efficiency or minimises charging time. A more representative optimisation criterion should simultaneously consider electrical conversion performance, thermal uniformity, recoverable energy and cyclic operability. The numerical framework developed in this thesis provides a basis for this type of coupled analysis because it resolves the spatial temperature distribution and allows the consequences of electromagnetic, geometrical and operational changes to be evaluated beyond a single average packed-bed temperature. Extending the framework towards systematic multi-objective optimisation therefore represents a natural step towards identifying technically viable IH-PBTES configurations for industrial process-heat applications.

4.3 Model Limitations and Future Developments

Although the numerical framework developed in this work extends the reference IH-PBTES model towards a spatially resolved description of charging, discharging and repeated

operation, the results must be interpreted in relation to the assumptions introduced at the electromagnetic, thermal and system levels. These assumptions were adopted to retain a computational cost compatible with transient, parametric and cyclic simulations while progressively increasing the physical detail of the reference model. They do not prevent the framework from identifying the comparative trends discussed in the previous sections, but they affect the level of quantitative accuracy that can be expected from local temperature, heat-generation and system-performance predictions. The present limitations therefore also define the main directions for future model development.

A first group of limitations concerns the electromagnetic representation of the induction-heating process. The finite induction coil is represented as a sequence of circular turns and its magnetic field is resolved spatially in the radial and axial directions. However, the resulting field is evaluated as an equivalent free-space field through $H = B/\mu_0$, without solving the modification of the electromagnetic field caused by the presence of the magnetite packed bed itself. The model therefore captures the geometrical non-uniformity and end effects associated with the finite coil, but does not reproduce material-induced field distortion, electromagnetic shielding or other interactions arising from the actual arrangement of magnetic particles. Furthermore, the axisymmetric formulation excludes azimuthal variations associated with random particle packing, coil leads and other three-dimensional geometrical asymmetries. A higher-fidelity Maxwell-based electromagnetic model, coupled with the thermal solver, would therefore be particularly valuable for detailed prediction of local heat deposition and future optimisation of the coil–packed-bed configuration [34], [59].

The main limitation of the hysteresis-heating model adopted in this work is associated with the LangArc formulation at low magnetic-field amplitudes. In this regime, the model becomes poorly constrained and may predict non-physical trends when the local peak magnetic field becomes too small. Consequently, the hysteresis operating conditions considered in this work were selected by imposing a practical minimum-field requirement of approximately $H_{\mathrm{peak,min}} \geq 20\mathrm{kA/m}$ throughout the computational domain. This value is a modelling constraint associated with the present hysteresis formulation and must not be interpreted as a physical minimum operating field for an IH-PBTES system. Moreover, the hysteresis-only simulations were performed at 80 Hz, whereas the adopted hysteresis parameterisation was not experimentally validated at this frequency. Within the present implementation, frequency primarily converts the energy dissipated per hysteresis cycle into heating power, while the loop description itself is determined from the adopted field- and temperature-dependent parameters [41]. Consequently, the trends obtained from the hysteresis-only simulations remain useful for analysing spatial behaviour

and thermo-magnetic feedback, but the absolute hysteresis power predicted at 80 Hz would benefit from dedicated experimental validation or a hysteresis parameterisation established over the frequency range relevant to IH-PBTES operation.

The eddy-current contribution is subject to a different approximation. The equivalent global formulation inherited from the reference model is retained rather than replacing it with a particle-resolved electromagnetic solution. The baseline eddy-current power is spatially redistributed according to the local magnetic-field intensity and subsequently corrected using the temperature dependence of electrical conductivity and effective magnetic permeability. This procedure introduces spatial and thermal information while preserving the energetic structure of the reference formulation, but it does not resolve the microscopic current-density distribution inside individual magnetite pebbles, local particle-scale skin-effect fields, electromagnetic shielding between neighbouring particles or detailed current paths within the granular medium. Particle-resolved magneto-thermal modelling, such as that applied to inductively heated particles in previous studies [59], could provide additional information on these mechanisms, although at a substantially greater computational cost.

The separation of hysteresis and eddy-current heating adopted in the main analyses must also be considered when interpreting the results. The numerical framework is able to construct a total source according to $q_{\mathrm{src}} = q_{\mathrm{hys}} + q_{\mathrm{eddy}}$; however, the hysteresis-only and eddy-current-only cases investigated in this thesis were evaluated at different operating points because the current levels required by the two isolated simulations were not compatible within the adopted modelling framework. In particular, the low-field limitation of the LangArc hysteresis model required a sufficiently high coil current to maintain the local magnetic-field amplitude within the reliable range of the formulation. Consequently, the hysteresis-only case was operated at a substantially higher current than the eddy-current-only case. The two simulations should therefore be interpreted as separate diagnostic cases used to investigate the characteristic behaviour of each heating contribution, rather than as a direct comparison at identical electrical operating conditions.

Their individual results therefore cannot be superimposed a posteriori to predict the behaviour of a real induction-heated packed bed. In practice, both mechanisms would act simultaneously under the same current, frequency, magnetic-field distribution and evolving temperature field. A natural continuation of the present work would therefore be to investigate the combined source at common operating points and determine how the negative temperature feedback associated with hysteresis interacts with the positive temperature dependence observed for the implemented eddy-current contribution.

A second important source of uncertainty concerns the temperature-dependent properties of magnetite. The present framework improves upon a constant-property representation by locally updating specific heat capacity, thermal conductivity, electrical conductivity and effective relative magnetic permeability. Nevertheless, the adopted correlations are derived from experimental datasets covering finite temperature intervals and are clipped outside their respective ranges. In particular, the predicted eddy-current localisation is influenced by the temperature-dependent conductivity over its implemented experimental range, while conductivity is held constant above 800 K due to the adopted clipping procedure. Similarly, the specific heat capacity and raw-magnetite thermal conductivity are retained at their boundary values outside approximately 50–500 °C and 50–550 °C, respectively. The calculated behaviour at temperatures beyond these experimental ranges should consequently be interpreted with greater caution.

The effective magnetic permeability introduces an additional uncertainty. The data adopted from Dunlop [46] are not used as absolute permeability measurements for the centimetric magnetite pebbles considered in the storage system. Instead, the temperature evolution of the initial susceptibility measured for a much smaller magnetite fraction is used only as a relative thermal scaling of the reference permeability adopted in the original IH-PBTES framework. The resulting $\mu_r(T)$ should therefore be interpreted as an effective temperature correction rather than a directly measured electromagnetic property of the actual packed-bed particles. This approximation becomes particularly relevant at high temperature, since the magnetic behaviour of magnetite changes substantially in the vicinity of its Curie region, approximately 570–585 °C [46], [47]. The present combination of interpolated and clipped material properties does not provide a complete representation of the rapid electromagnetic changes occurring through this transition. Dedicated high-temperature measurements of electrical conductivity, permeability and hysteresis behaviour for magnetite particles representative of the size and composition considered here would therefore significantly improve the predictive capability of the model.

An important limitation of the present thermal model is associated with the macroscopic representation of the packed bed. The granular storage medium is treated as an equivalent axisymmetric continuum with uniform porosity, and the individual magnetite pebbles, their contact network and the detailed geometry of the void space are not resolved. During charging, the thermal capacity of the interstitial gas is neglected and the temperature-dependent thermal conductivity of raw magnetite, $k(T)$, is directly used as the conduction coefficient of the continuum domain. Consequently, solid-to-solid contact resistance, heat conduction through the gas phase and inter-particle radiative heat transfer are not explicitly represented.

This point is particularly relevant because the effective thermal conductivity of a packed bed is not equivalent to the intrinsic conductivity of the solid filler. Díaz-Heras et al. [68] reviewed the correlations available for packed-bed effective thermal conductivity and showed that the equivalent heat-transfer behaviour results from the interaction of several mechanisms and depends on the properties of the solid and fluid phases, particle and bed characteristics and operating conditions. Their review distinguishes stagnant, axial and radial effective conductivities and discusses formulations in which radiative heat transfer becomes increasingly relevant at elevated temperature [68]. The use of raw-magnetite $k(T)$ in the present continuum model therefore represents a simplification of the actual internal heat-transfer process and may influence the quantitative prediction of temperature gradients and local hot spots. A future refinement should introduce an effective thermal-conductivity formulation specifically appropriate to a magnetite–air packed bed over the relevant temperature range, ideally supported by experimental measurements. Separate radial and axial effective conductivities could also be considered if significant anisotropy of the macroscopic heat-transfer process were identified.

The treatment of temperature-dependent conductivity in the thermal equation also introduces a numerical approximation. As described in Section 2.5, the implemented solver evaluates the conductive contribution in the form $k(T)\nabla^2 T$. The more general conservative expression is instead $\nabla \cdot [k(T)\nabla T]$, which additionally accounts for heat-flux variations associated with spatial gradients of thermal conductivity. The present formulation therefore retains the local temperature dependence of k but omits the additional $\nabla k \cdot \nabla T$ contribution that arises when conductivity varies spatially. This approximation is expected to become most relevant where strong temperature gradients coexist with significant property variations. Reformulating the thermal solver in conservative form would consequently provide a straightforward improvement while preserving the existing two-dimensional framework.

A further numerical limitation concerns spatial and temporal resolution. A systematic grid- and time-step-independence study was not carried out in the present work. This is particularly relevant for local quantities such as the maximum packed-bed temperature and the temperature non-uniformity, which may be more sensitive to numerical resolution than volume-averaged quantities. Future work should therefore quantify the convergence of $T_{\max}$ and ΔT through progressive mesh refinement and time-step reduction.

External heat losses are likewise represented through a simplified equivalent-boundary formulation. The lateral and end surfaces use thermal resistances that combine conduction through the insulation with a prescribed external convective coefficient, while the corresponding equivalent heat-transfer coefficients are calculated from a reference temperature and retained

during each transient simulation. The insulation is not represented as an independent transient thermal domain, its thermal inertia is therefore neglected, and the refractory vessel is not modelled as a separate thermal mass. In addition, the external convective coefficient is prescribed rather than calculated from a temperature-dependent natural-convection correlation, while radiative heat exchange between the external storage surface and the surroundings is not included as an independent boundary mechanism. More detailed packed-bed storage models may distinguish these heat-transfer paths explicitly [54]. The present formulation is sufficient to introduce spatially varying boundary losses into the two-dimensional domain, but a more complete enclosure model would be required to improve the absolute prediction of environmental heat losses, particularly at the highest operating temperatures and for longer storage periods.

The discharge formulation introduces a further set of assumptions. The solid phase preserves its transient two-dimensional description, whereas the air is treated through a quasi-steady cell-by-cell NTU procedure rather than through a complete transient fluid-energy equation. The physical configuration assumes that the total air flow divides equally between the two ends of the storage unit and moves towards the central outlet. The two end-to-centre portions of the charging temperature map are transformed to a common orientation and averaged before the half-bed discharge calculation is performed. Within the simulated domain, the superficial mass flux is assumed uniform across the cross section and the individual radial annuli are treated as independent parallel flow paths. Radial fluid mixing, radial fluid conduction, explicit thermal dispersion, flow maldistribution and preferential channeling are therefore not represented. Although temperature-dependent air properties and the Gunn heat-transfer correlation are retained [55], [56], the resulting formulation should be regarded as an efficient model of thermal extraction from the two-dimensional solid field rather than as a complete simulation of porous-fluid flow.

Pressure drop is also not coupled to the discharge calculation. Consequently, the electrical consumption required for air circulation through the packed bed is not deducted from the useful recovered energy. This limitation is particularly important when comparing discharge strategies because an increase in mass-flow rate may increase thermal-power extraction while simultaneously increasing fan or compressor requirements. The recovered energies reported in the present work are therefore thermal quantities. Similarly, the cyclic electrical-energy balance is defined at the coil–load boundary and excludes the frequency-converter losses considered in the charging-stage efficiency analysis. The reported cycle-level round-trip efficiency consequently represents a performance indicator within the specific boundaries adopted in this thesis and should not be interpreted as a complete plant-level electrical-to-useful-heat efficiency. A future system-level model should incorporate pressure-drop correlations, air-circulation auxiliary consumption

and converter losses in order to extend the present thermal analysis to the complete electrical energy balance.

The cyclic simulations are additionally dependent on the adopted operating criteria. The maximum packed-bed temperature of 650 °C was introduced as a preliminary numerical safety threshold and does not represent a validated material, vessel or system operating limit. Its activation directly influences the actual electrical energy supplied to the safety-limited eddy-current cycles and therefore also affects their calculated round-trip efficiencies. Similarly, the 300 °C discharge threshold represents a selected definition of useful high-temperature heat for the present analysis rather than a universal process requirement. The amount of energy classified as useful or unrecovered would change for industrial processes requiring a different delivery temperature. Sensitivity analyses considering alternative charging-temperature constraints and discharge-temperature requirements would therefore be necessary before application-specific operating recommendations could be established. The number of simulated cycles represents another limitation. Three consecutive cycles were sufficient to demonstrate that the cold-start condition is not representative of subsequent operation and to identify a clear tendency towards similar behaviour between the second and third cycles. They are not, however, sufficient to establish a mathematically periodic steady state. Longer sequences should therefore be simulated until appropriate convergence criteria for the residual temperature field and relevant energy indicators are satisfied. This extension would also make it possible to investigate more realistic operation under variable renewable-electricity availability, irregular charging durations and changing thermal demand. Furthermore, the present simulations assume that the physical and electromagnetic characteristics of the storage medium remain unchanged between cycles. Material ageing, thermal and mechanical degradation, irreversible evolution of the magnetite properties and rearrangement of the pebble packing are not included and would become increasingly relevant in a long-term durability assessment.

Finally, the validation performed in this thesis is limited to a numerical consistency assessment of the two-dimensional thermal implementation. Under equivalent uniform-source conditions, the volume-averaged temperature predicted by the new solver differs by less than 1 °C from the reference lumped model after three hours of charging. This result confirms that introducing the spatial thermal discretisation does not significantly alter the global response when the assumptions of the reference formulation are reproduced. However, it does not constitute experimental validation of the complete IH-PBTES framework. In particular, the two-dimensional magnetic-field distribution, spatial heat-generation maps, local temperature gradients, air-outlet evolution during discharge and repeated-cycle predictions have not yet been validated against

experimental measurements. Experimental measurements of coil electrical behaviour and induced power, internal packed-bed temperatures at different radial and axial positions, discharge outlet temperature and recovered thermal energy would therefore represent a fundamental next step towards quantifying model uncertainty and establishing its predictive accuracy.

Overall, the numerical framework developed in this thesis should be regarded as an intermediate step between the original lumped technical-viability model and a fully predictive IH-PBTES design tool. Its principal contribution is the introduction of spatially resolved electromagnetic excitation, temperature-dependent local heat generation, two-dimensional thermal evolution, heat recovery and thermal-state propagation across repeated cycles while retaining a computational cost compatible with parametric studies. The most relevant future developments are therefore the evaluation of combined hysteresis and eddy-current heating at common operating points, higher-fidelity electromagnetic field modelling, experimentally validated high-temperature magnetite properties, effective packed-bed thermal transport, a conservative variable-conductivity thermal formulation, improved enclosure heat-loss modelling, transient porous-flow discharge including hydraulic and auxiliary-energy effects, longer cyclic simulations and experimental validation. Together with the multi-objective design considerations discussed in Section 4.2, these developments would progressively enable the framework to move from comparative performance analysis towards quantitative optimisation and design of IH-PBTES systems for industrial process-heat applications.

5. Conclusions

The present thesis investigated the thermo-electromagnetic behaviour of an induction-heated packed-bed thermal energy storage (IH-PBTES) system through the development of a spatially resolved numerical framework extending the reference lumped IH-PBTES model. While lumped formulations provide an effective tool for preliminary technical assessments, they do not provide information on the spatial distribution of the electromagnetic field, local heat-generation patterns, temperature gradients or the evolution of the thermal state within the packed bed. To overcome these limitations, the developed framework introduces a two-dimensional axisymmetric description of the storage medium, including the spatial distribution of the induction field, temperature-dependent magnetite properties, transient thermal evolution, discharge modelling and repeated charge–discharge simulations.

The first objective of the work was therefore the extension of the reference model towards a more detailed representation of the coupled electromagnetic–thermal behaviour of the packed bed while preserving a computational cost compatible with parametric and cyclic analyses. The resulting framework enables the investigation of local heat-generation mechanisms, temperature non-uniformities and the interaction between the initial thermal state and subsequent operating cycles, providing information that cannot be obtained from a purely lumped description.

The developed thermal formulation was first assessed against the reference lumped IH-PBTES model under equivalent uniform-source charging conditions. The two-dimensional implementation reproduced the global thermal response of the reference model, with a difference between the predicted volume-averaged temperatures below 1 °C after three hours of charging. This result demonstrates that the introduction of the spatial thermal discretisation preserves the overall behaviour of the original formulation when its assumptions are recovered. However, this comparison represents a numerical consistency validation of the thermal solver rather than an experimental validation of the complete IH-PBTES framework, and further experimental measurements are required to assess the predictive capability of the electromagnetic and thermal models.

The analysis of the two isolated induction heat-generation mechanisms highlighted the importance of considering both electromagnetic efficiency and spatial thermal behaviour when evaluating IH-PBTES charging strategies. Within the operating conditions and material-property formulation considered in this work, the hysteresis-dominated case exhibited a more controlled thermal response due to the progressive reduction of the heat-generation contribution with increasing temperature. This behaviour introduced a partially self-regulating thermo-magnetic response, limiting the amplification of local temperature differences. Conversely, the eddy-current

contribution showed a stronger temperature-dependent localisation tendency, as the implemented conductivity variation enhanced the heat-generation correction in warmer regions over the investigated temperature range. The comparison therefore demonstrated that a higher electromagnetic conversion performance does not necessarily correspond to the most favourable thermal behaviour for storage applications. In an IH-PBTES system, charging quality must be assessed considering simultaneously induction efficiency, temperature uniformity, maximum local temperature and the requirements of the subsequent heat-recovery phase.

The investigation of packed-bed aspect ratio further demonstrated that the spatial distribution of the induction field plays a fundamental role in determining the thermal response of the storage medium. Maintaining a comparable average magnetic excitation does not guarantee an equivalent local heat-generation distribution, since the interaction between geometry and electromagnetic field localisation modifies the resulting temperature gradients. The eddy-current dominated cases showed a stronger sensitivity to the packed-bed configuration, whereas the hysteresis-dominated cases exhibited a comparatively more distributed response. These results indicate that packed-bed geometry, coil configuration and operating conditions should be considered as coupled design variables rather than optimised independently. Therefore, the design of IH-PBTES systems should not be based exclusively on maximising induced power or electrical efficiency, but should also account for thermal uniformity and local temperature constraints.

The discharge analysis introduced an additional operational perspective by showing the trade-off between heat extraction rate and temperature quality of the recovered energy. Increasing the air mass-flow rate increased the instantaneous thermal power extraction and accelerated energy recovery, but simultaneously reduced the outlet-temperature level and shortened the duration of useful high-temperature heat delivery. Consequently, discharge performance cannot be evaluated only in terms of recovered energy, since the temperature level and availability of the delivered heat are equally important for industrial applications. The mass-flow rate adopted for the cyclic simulations was therefore selected as a representative condition favouring high-temperature heat delivery rather than as a universal optimum. In practical IH-PBTES applications, the air flow rate should be considered as an operational control variable depending on the required process temperature, thermal-power demand and instantaneous state of charge of the storage medium.

The repeated charge–discharge simulations demonstrated the importance of considering the residual thermal state inherited from previous cycles. The first cycle, corresponding to a cold-start condition, was shown to differ from subsequent cycles because the temperature distribution remaining after discharge modifies the following charging process. For the hysteresis-dominated case, the second and third cycles exhibited very similar behaviour, indicating a tendency towards

repeatable operation after the initial transient. The eddy-current dominated case also showed repeatable behaviour in subsequent cycles; however, this was strongly affected by the imposed maximum-temperature constraint, which limited the charging process before reaching the same energy input conditions. Therefore, the higher cycle efficiencies obtained in these cases should not be interpreted as a direct indication of superior thermal-storage performance. Instead, they reflect the different interaction between thermal localisation, safety constraints and the selected energy balance definition. Overall, the simulated cycles identify a tendency towards repeatable behaviour, but the limited number of cycles does not demonstrate the achievement of a true periodic steady state.

The developed framework should therefore be interpreted as an intermediate step between the original lumped technical-viability model and a fully predictive design tool for industrial IH-PBTES systems. The main limitations identified in this work include the equivalent electromagnetic representation of eddy-current heating, the absence of particle-resolved electromagnetic interactions, uncertainties associated with high-temperature magnetite properties, the use of raw-magnetite thermal conductivity instead of a dedicated packed-bed effective conductivity formulation, simplified external heat-loss modelling, the quasi-steady representation of the air phase during discharge and the absence of long-term degradation effects. Future developments should therefore focus on experimental validation of the electromagnetic and thermal predictions, combined hysteresis–eddy current analyses under common operating conditions, improved high-temperature material-property characterisation, more detailed packed-bed heat-transfer formulations, transient porous-flow discharge modelling including hydraulic losses and auxiliary consumption, and longer-term cyclic simulations.

Overall, this thesis demonstrates that the design and operation of IH-PBTES systems require a simultaneous consideration of electromagnetic conversion, spatial thermal behaviour and heat-recovery requirements. The developed two-dimensional framework provides a more detailed understanding of the interactions between induction heating mechanisms, packed-bed geometry, discharge operation and thermal history, representing a step towards the optimisation and future implementation of induction-heated packed-bed thermal energy storage systems for high-temperature industrial heat applications.

6. Appendix A – Software Implementation and Code Structure

A.1 Software Environment and Computational Workflow

The numerical framework developed and analysed in this thesis was implemented in Python. The computational work was organised using two complementary development environments. The numerical modules were primarily developed and tested as standalone Python scripts (.py) using the Spyder integrated development environment (IDE), whereas JupyterLab was used as an interactive notebook environment for the execution of simulation cases, post-processing of the numerical results and generation of the figures presented in this work. This separation provided a convenient workflow in which the physical and numerical models were maintained as reusable Python modules, while the notebook was used as the main interface for their application and analysis.

The implementation relies on a set of standard scientific-computing libraries. NumPy is used extensively for the definition and manipulation of numerical arrays, computational grids, temperature fields and other spatially distributed quantities. SciPy provides the numerical and special-function capabilities required by different parts of the electromagnetic formulation, including numerical integration and the elliptic functions employed in the calculation of the magnetic field generated by the circular coil turns. Matplotlib is used for the graphical representation of simulation outputs, including transient temperature and power histories, spatial field distributions and the comparative plots reported in the Results chapter. pandas is also included among the dependencies of the reference implementation for the handling of tabulated data. Finally, CoolProp is employed to evaluate the temperature-dependent thermophysical properties of air required by the discharge model. The latter properties are subsequently tabulated and interpolated during the simulations in order to reduce the computational cost associated with repeated property evaluations.

From a software perspective, the numerical model was developed following a modular structure. The physical formulations are contained in a set of Python modules that progressively extend the original lumped IH-PBTES implementation towards the two-dimensional framework described in Chapter 2. Separate modules are then used to introduce the discharge calculation and the repeated charge–discharge procedures. This organization allows the individual components of the model to be developed and tested separately while retaining a common underlying representation of the storage system.

The JupyterLab notebook constitutes the final analysis layer of this workflow. The required Python classes and additional model modules are imported into the notebook, where the material

properties, geometrical parameters, computational mesh and operating conditions are defined for each investigated case. The corresponding numerical routines are then executed and their outputs are processed to obtain the global performance indicators, transient histories and two-dimensional distributions discussed in Chapter 3. The notebook was therefore used primarily as an interface between the numerical model and the analysis of its results, rather than as the location of the core physical implementation. The detailed organization of the Python modules and their respective roles within the complete computational framework is presented in the following section.

A.2 Code Organization and Main Modules

The computational framework was organized into a set of interconnected Python modules rather than into a single monolithic script. This structure reflects the progressive development followed during the thesis: the original lumped IH-PBTES implementation was retained as the reference foundation, while additional modules were introduced to describe the two-dimensional electromagnetic and thermal behaviour, the discharge process and repeated charge–discharge operation. The complete working directory used for the numerical analysis contains six Python modules (.py), one Jupyter notebook (.ipynb) and two tabulated data files (.tsv).

The central relationship between the modules is based on the IHTES class contained in class_IHTES.py. The two-dimensional implementations inherit the main geometrical, electromagnetic and system-level quantities from this reference class and introduce the additional spatial calculations required in the present work. The discharge and cyclic routines are maintained in separate modules and are subsequently associated with the final two-dimensional model when required. This organisation made it possible to retain the reference formulation while progressively introducing the additional numerical capabilities developed during the thesis.

Table A.1 summarises the files composing the computational framework and their principal function.

File	Type	Main role
class_IHTES.py	Python module	Reference lumped IH-PBTES implementation. It contains the basic packed-bed and coil geometry, hysteresis and eddy-current formulations, coil and converter losses, thermal losses, charging power balances and the original lumped charging routine.
class_IHTES_2D.py	Python module	Intermediate two-dimensional extension of the reference model. It introduces the axisymmetric $r-z$computational domain, finite-coil magnetic-field calculation, spatial weighting and initial two-

		dimensional thermal routines used during model development and validation.
class_IHTES_2D_Tdep.py	Python module	Main two-dimensional charging model adopted for the final analyses. It includes the spatial magnetic field, local induction heat-generation terms, temperature-dependent magnetite properties and the transient two-dimensional thermal solver with local boundary heat losses.
discharging_model.py	Python module	Implements thermal discharge using air as the heat-transfer fluid. It includes temperature-dependent air properties, the Gunn heat-transfer correlation, the cell-by-cell NTU formulation, enthalpy-based energy recovery and treatment of the symmetric half-bed discharge domain.
cycles_same_energy_input.py	Python module	Implements repeated charge–discharge simulations in which each charging phase is controlled by a prescribed cumulative electrical-energy input. It also propagates the residual temperature field from one cycle to the following one.
cycles_same_Tmean_target.py	Python module	Implements the second cyclic comparison strategy, in which charging is continued until a prescribed volume-averaged packed-bed temperature is reached, subject to the imposed local maximum-temperature constraint.
langarc_magn97.tsv	Tabulated data	Contains the LangArc hysteresis-model parameters used for magnetite and imported by the numerical workflow.
langarc_hematiteMD.tsv	Tabulated data	Contains the corresponding tabulated LangArc hysteresis-model dataset for hematite, retained among the material input files of the computational framework.
IHTES_analysis_2D.ipynb	Jupyter notebook	Main interactive analysis notebook. It imports and initialises the model classes, defines material, geometrical and operating parameters, executes the numerical cases and performs post-processing and graphical representation of the simulation results.

Table A.1 – Main files composing the numerical framework and their role in the computational workflow.

The first Python module, class_IHTES.py, represents the software implementation associated with the reference IH-PBTES formulation introduced in Section 2.1. Its IHTES class defines the principal properties of the storage material, packed-bed and coil geometry, together with the underlying hysteresis and eddy-current heating models. It also evaluates electrical losses in the coil, converter efficiency, heat losses to the environment and the principal power and efficiency indicators. The original transient charging routine advances a single representative

packed-bed temperature in time and therefore provides the lumped implementation from which the spatial developments of this thesis originate.

The first stage of the spatial extension is contained in class_IHTES_2D.py. The IHTES2D class inherits the quantities and methods of IHTES and introduces a two-dimensional axisymmetric grid defined by radial and axial coordinates. The finite induction coil is represented through individual circular turns distributed along its axial length, and the magnetic-field components produced by each turn are evaluated and superimposed over the computational domain. The module additionally introduces axisymmetric volume weighting and two-dimensional charging routines. In particular, both a uniform-source formulation and a spatially non-uniform formulation based on the calculated magnetic-field distribution are retained. These routines were useful during the progressive development and numerical consistency assessment of the spatial model.

The more complete implementation is contained in class_IHTES_2D_Tdep.py, through the IHTES2D_Tdep class. This module retains the two-dimensional electromagnetic description while adding the local temperature dependence required for the final charging simulations. The thermophysical and electromagnetic properties of magnetite are evaluated as functions of temperature, and the hysteresis and eddy-current source distributions can consequently evolve together with the local thermal field. The final charging routine therefore operates on the complete temperature map $T(r, z, t)$, recalculating the local induction source and the relevant material properties during the transient solution. This module constitutes the principal charging engine used for the analyses presented in Chapters 2 and 3.

The discharge process is implemented separately in discharging_model.py. Rather than defining an independent storage-system class, this module provides the additional functions required to extend IHTES2D_Tdep to the discharge phase. The final charging temperature field is converted into the half-bed representation adopted for the symmetric end-to-centre airflow configuration, after which air is propagated through the discretised packed bed using the local Gunn correlation and NTU formulation described in Section 2.7. Temperature-dependent air properties are generated using CoolProp and subsequently interpolated during the calculation. The routine retains both local fields and global quantities such as outlet-air temperature, recovered thermal power and cumulative recovered energy.

Repeated operation is handled by the two dedicated cycle modules. Cycles_same_energy_input.py implements the strategy based on a prescribed cumulative electrical input, whereas cycles_same_Tmean_target.py implements charging towards a prescribed volume-averaged packed-bed temperature. Both modules use the same underlying

charging and discharging models and differ principally in the charging stopping condition. At the end of each discharge, the residual half-bed temperature distribution is mirrored to reconstruct the complete two-dimensional packed-bed field, which is then used as the initial condition of the subsequent charging phase. The cycle modules therefore provide the higher-level routines required to connect the individual charging and discharge simulations while preserving the spatial thermal history of the system.

The numerical modules are finally coordinated through IHTES_analysis_2D.ipynb. The notebook contains the definition of material and geometrical inputs, imports the required model implementations, creates the corresponding model instances and specifies the operating conditions for the investigated cases. It was also used during the progressive development of the model to compare the reference and two-dimensional formulations, investigate different operating conditions and generate the graphical outputs subsequently selected for the thesis. The notebook therefore represents the analysis and post-processing layer of the computational framework, while the principal physical and numerical formulations remain contained within the dedicated Python modules.

Overall, this modular organisation separates the reference model, the successive two-dimensional developments, the discharge formulation and the cyclic operating procedures while allowing them to share a common set of system definitions. The following section reports selected excerpts of the source code corresponding to the most relevant numerical developments, whereas the complete implementation is made available through the repository indicated at the end of this Appendix.

A.3 Selected Key Code Implementations

The complete computational framework contains a considerably larger number of functions than can be conveniently reported within the thesis. This section therefore presents a selection of the source-code excerpts that most directly represent the numerical developments introduced in the present work. The selected listings focus on the calculation of the two-dimensional magnetic field, the formulation of the local temperature-dependent induction sources, the transient two-dimensional charging solver, the cell-by-cell discharge calculation and the propagation of the residual thermal state between consecutive cycles.

The excerpts reported below are reproduced directly from the corresponding Python source files. Variable names, comments and internal implementation choices have intentionally been retained in their original form. Auxiliary functions associated mainly with plotting, output storage,

diagnostic calculations and repeated initialisation are omitted from the Appendix, while the complete source code is provided through the repository indicated in Section A.4.

A.3.1 Two-dimensional magnetic-field evaluation

A fundamental extension with respect to the reference lumped implementation is the replacement of the uniform solenoidal magnetic field by a spatially resolved field over the axisymmetric $r - z$ domain. The magnetic contribution of each circular coil turn is evaluated separately. On the symmetry axis, the analytical axial-field expression is used, whereas away from the axis the radial and axial components are evaluated through complete elliptic integrals. The contributions of all turns are subsequently superimposed to obtain the complete magnetic-field map.

The implementation of the single-turn calculation and subsequent field superposition is reported in Listing A.1.

```
    def single_turn_field(self, r, z, a, z_turn, I):
"""
Campo magnetico di una singola spira circolare di raggio a,
posta alla quota z_turn, in coordinate cilindriche (r,z).

Restituisce:
Br, Bz
"""
r = np.asarray(r, dtype=float)
z = np.asarray(z, dtype=float)

z_rel = z - z_turn

Br = np.zeros_like(r, dtype=float)
Bz = np.zeros_like(r, dtype=float)

# punti sull'asse r = 0
axis_mask = np.isclose(r, 0.0)

if np.any(axis_mask):
    Bz[axis_mask] = mu_0 * I * a**2 / (2.0 * (a**2 + z_rel[axis_mask]**2)**1.5)
    Br[axis_mask] = 0.0

# punti fuori asse
off_mask = ~axis_mask
if np.any(off_mask):
    rr = r[off_mask]
    zz = z_rel[off_mask]

    alpha2 = (a + rr)**2 + zz**2
    beta2  = (a - rr)**2 + zz**2

    k2 = 4.0 * a * rr / alpha2
    k2 = np.clip(k2, 0.0, 1.0 - 1e-12)

    K = ellipk(k2)
    E = ellipe(k2)

    alpha = np.sqrt(alpha2)

    common = mu_0 * I / (2.0 * np.pi * alpha)

    Br_val = common * (zz / rr) * (
        -K + E * (a**2 + rr**2 + zz**2) / beta2
    )

    Bz_val = common * (
        K + E * (a**2 - rr**2 - zz**2) / beta2
    )
```

```
            Br[off_mask] = Br_val
            Bz[off_mask] = Bz val

        return Br, Bz

    def field_map(self, I):
        """
        Somma il contributo di tutte le spire.
        Restituisce:
        Br tot, Bz tot, B tot, H tot
        """
        Br_tot = np.zeros_like(self.R)
        Bz_tot = np.zeros_like(self.Z)

        for zt in self.z_turns:
            Br_i, Bz_i = self.single_turn_field(self.R, self.Z, self.a_coil, zt, I)
            Br tot += Br i
            Bz_tot += Bz_i

        B tot = np.sqrt(Br tot**2 + Bz tot**2)

        # prima approssimazione: H = B / mu0
        H_tot = B_tot / mu_0

        return Br_tot, Bz_tot, B_tot, H_tot
```

Listing A.1 – Evaluation and superposition of the magnetic field generated by the finite induction coil (class_IHTES_2D_Tdep.py).

The resulting arrays contain the radial and axial magnetic-flux-density components and the corresponding field magnitude at every node of the computational mesh. This field map is subsequently used by the heat-generation routines instead of assigning a single representative field value to the complete packed bed. As discussed in Chapter 2, the calculation represents the field generated by the coil in free space and does not constitute a fully coupled electromagnetic solution including field distortion produced by the packed material.

A.3.2 Local temperature-dependent induction sources

The spatial field distribution is coupled with the local temperature field when evaluating electromagnetic heat generation. For the eddy-current contribution, the previously established spatial source distribution is retained as the reference state and corrected according to the relative variation of electrical conductivity and effective magnetic permeability with temperature. This implementation was adopted in order to introduce temperature dependence without replacing the absolute reference eddy-current power formulation used during model development.

```
        def qeddy_map_Tlocal(self, freq, I, T_map):
    """
Densità di potenza eddy locale [W/m3] con dipendenza termica relativa
di sigma(T) e mu r(T).

IMPORTANTE:
qeddy_map(freq, I) è la mappa eddy del modello già validato.

Per non rompere la validazione, non sostituiamo il valore assoluto
della conducibilità del modello con quello del paper.

Usiamo solo i rapporti relativi:

    sigma_scale = sigma(T) / sigma(T_ref)
    mu_scale    = [mu_r(T) / mu_r(T_ref)]^2
```

```
    così a T_ref la nuova q_eddy coincide con quella validata.
    """
        T map = np.asarray(T map, dtype=float)

    # mappa eddy del modello validato
        q eddy ref = self.qeddy map(freq, I)

    # temperatura di riferimento: temperatura iniziale del charging
        T_ref = 293.15

    # variazione relativa della conducibilità elettrica
        sigma_scale = self.sigma_magnetite_T(T_map) / self.sigma_magnetite_T(T_ref)

    # variazione relativa della permeabilità magnetica efficace
        mu_scale = (self.mu_r_magnetite_T(T_map) / self.mu_r_magnetite_T(T_ref))**2

    # nuova q_eddy: stessa q_eddy validata, ma corretta solo per la variazione con T
        q eddy T = q eddy ref * sigma scale * mu scale

        return q_eddy_T
```

Listing A.2 – Temperature-dependent correction of the local eddy-current heat-generation map (class_IHTES_2D_Tdep.py).

The hysteresis contribution is evaluated directly at cell level using the local magnetic-field amplitude and local solid temperature. The model can then select the total source or isolate either contribution through the source_mode argument. This capability is particularly useful for the diagnostic hysteresis-only and eddy-current-only comparisons discussed in Chapter 3. The corresponding routines are shown in Listing A.3.

```
           def qhys_map_Tlocal(self, freq, I, T_map):
        """
        Densità di potenza isteretica locale [W/m3] usando:
        - H locale da field_map(I)
        - T locale della cella T_map[i,j]

        Questa versione chiama Phys_sp con scalari, evitando problemi
        quando Phys_sp riceve array 2D.
        """
        _, _, _, H_rms = self.field_map(I)
        H_peak = np.sqrt(2.0) * H_rms

        T_map = np.asarray(T_map, dtype=float)
        q_hys = np.zeros_like(T_map, dtype=float)

        for i in range(self.Nr):
            for j in range(self.Nz):
                q_hys[i, j] = (
                    self.Phys_sp(H_peak[i, j], T_map[i, j], freq)
                    * self.rho_s
                    * (1.0 - self.e)
                )

        return q hys

    def qind_map_Tlocal(self, freq, I, T_map):
        """
        Densità di potenza totale indotta [W/m3] con proprietà locali.

        q_hys:
            dipende da H(r,z) e T(r,z), tramite LangArc/Phys_sp.

        q_eddy:
            dipende da H(r,z), sigma(T) e mu_r(T).
        """
        q_hys = self.qhys_map_Tlocal(freq, I, T_map)
        q_eddy = self.qeddy_map_Tlocal(freq, I, T_map)

        return q hys + q eddy
    def qsource_map_Tlocal(self, freq, I, T_map, source_mode="total"):
        """
    Seleziona la sorgente termica da usare nel charging.

    source_mode:
        "total"     -> q_hys + q_eddy
```

```
        "hys_only"  -> solo q_hys
        "eddy_only" -> solo q_eddy
    """
        if source_mode == "total":
            return self.qind_map_Tlocal(freq, I, T_map)

        elif source_mode == "hys_only":
            return self.qhys_map_Tlocal(freq, I, T_map)

        elif source_mode == "eddy_only":
            return self.qeddy map Tlocal(freq, I, T map)

        else:
            raise ValueError(
            "source_mode must be 'total', 'hys_only', or 'eddy_only'"
        )
```

Listing A.3 – Local hysteresis source and selection of the induction heat-generation mode (class_IHTES_2D_Tdep.py).

The thermophysical and electromagnetic property functions used by these routines are defined in the same module. Temperature-dependent magnetite heat capacity, thermal conductivity, electrical resistivity/conductivity and effective magnetic permeability are obtained by interpolation of the datasets introduced in Chapter 2. These auxiliary property functions are not reproduced here in full in order to keep the Appendix focused on the principal coupling mechanisms.

A.3.3 Two-dimensional transient charging solver

The central thermal calculation is performed by charging_2D_nonuniform_Tdep(). At each time step, the local electromagnetic source is first recalculated from the current temperature field. The solver then advances each cell explicitly using the local volumetric heat capacity and thermal conductivity.

Listing A.4 reports the main time-marching portion of the implemented routine. It also shows the treatment of the axial and radial boundaries through ghost nodes, the symmetry condition at r = 0, and the cylindrical-coordinate contribution to the radial Laplacian.

```
            for n in range(n_steps):
        q_src = self.qsource_map_Tlocal(freq, I, T, source_mode=source_mode)
        Tnew = T.copy()

        for i in range(self.Nr):
            r i = self.r[i]

            for j in range(self.Nz):
                rhoCp_ij = self.rhoCp_eff_T(T[i, j])
                k_ij = self.k_magnetite_raw(T[i, j])

                # ====================================================
                # Bordo assiale bottom/top con perdite verso ambiente
                # ====================================================
                if j == 0:
                    # bottom surface, z = 0
                    # ghost node esterno sotto il packed bed
                    T jp1 = T[i, 1]
                    T_jm1 = T_jp1 - 2.0 * self.dz * (h_eq_tb / k_ij) * (T[i, j] - T_amb)

                elif j == self.Nz - 1:
                    # top surface, z = H
                    # ghost node esterno sopra il packed bed
                    T_jm1 = T[i, self.Nz - 2]
                    T_jp1 = T_jm1 - 2.0 * self.dz * (h_eq_tb / k_ij) * (T[i, j] - T_amb)

                else:
                    # celle interne lungo z
                    T_jm1 = T[i, j - 1]
                    T_jp1 = T[i, j + 1]

                d2z = (T_jp1 - 2.0 * T[i, j] + T_jm1) / self.dz**2

                if i == 0:
                    radial = 4.0 * (T[1, j] - T[0, j]) / self.dr**2
                elif i == self.Nr - 1:
                    T_ghost = T[i - 1, j] - 2.0 * self.dr * (h_eq / k_ij) * (T[i, j] - T_amb)
                    d2r = (T_ghost - 2.0 * T[i, j] + T[i - 1, j]) / self.dr**2
                    d1r = (T_ghost - T[i - 1, j]) / (2.0 * self.dr)
                    radial = d2r + d1r / r i
                else:
                    d2r = (T[i + 1, j] - 2.0 * T[i, j] + T[i - 1, j]) / self.dr**2
                    d1r = (T[i + 1, j] - T[i - 1, j]) / (2.0 * self.dr)
                    radial = d2r + d1r / r_i

                laplacian = radial + d2z
                Tnew[i, j] = T[i, j] + (dt / rhoCp_ij) * (k_ij * laplacian + q_src[i, j])

        T = Tnew

        T_mean[n + 1] = self.volume_average(T)
        T_max[n + 1] = np.max(T)
        q_mean[n + 1] = self.volume_average(q_src)
        q_max[n + 1] = np.max(q_src)

        if ((n + 1) % save_every == 0) or (n == n_steps - 1):
            snapshots.append(T.copy())
            snapshot times.append((n + 1) * dt)
```

Listing A.4 – Main time-marching loop of the temperature-dependent two-dimensional charging solver (class_IHTES_2D_Tdep.py).

The source term is therefore not prescribed once at the beginning of the simulation, but is recalculated during the transient according to the evolving local state. At the same time, rhoCp_eff_T() and k_magnetite_raw() provide the temperature-dependent coefficients used in the explicit thermal update. The output includes the complete final temperature map together with the mean and maximum temperature histories, source histories and intermediate snapshots used for subsequent analysis and visualisation.

A.3.4 Cell-by-cell discharge implementation

The discharge model retains the transient two-dimensional description of the solid while propagating the air sequentially from the physical end of the half-bed towards the central outlet plane. For each computational cell, the local solid temperature and an iteratively updated air temperature are used to evaluate the volumetric solid–fluid heat-transfer coefficient through the Gunn correlation. Three internal iterations are performed because the air properties entering the correlation depend on temperature.

The core implementation is reported in Listing A.5. The local NTU is used to determine the air outlet temperature from each cell, after which the heat transferred to the fluid is evaluated from its enthalpy increase. The same amount of energy is removed from the local solid thermal capacity.

```
            for i in range(self.Nr):

        T_air_in_cell = float(T_air_in)
        h_air_in_cell = float(h_in)

        for j in range(Nz_half):

            Ts_ij = float(Ts_star[i, j])
            T_air_out_guess = T_air_in_cell

            # Iterate because properties depend on air temperature
            for   in range(3):

                T_air_mean = 0.5 * (T_air_in_cell + T_air_out_guess)

                Ts_tmp = np.array([[Ts_ij]])
                Tf_tmp = np.array([[T_air_mean]])

                 , h_v_tmp,  ,  ,   = self._gunn_hv(
                    Ts_tmp,
                    Tf_tmp,
                    m_dot_half=m_dot_half,
                    d_p=d_p,
                )

                h_v_ij = float(h_v_tmp[0, 0])
                cp_flow = float(cp_air(T_air_mean))

                NTU_cell = h_v_ij * dz_half / (G * cp_flow)

                T_air_out_guess = Ts_ij - (Ts_ij - T_air_in_cell) * np.exp(-NTU_cell)

            T_air_out_cell = float(T_air_out_guess)
            h_air_out_cell = float(h_air(T_air_out_cell))

            # Heat transferred to air per packed-bed volume [W/m3]
            q_to_air = G * (h_air_out_cell - h_air_in_cell) / dz_half

            # Solid update due to heat removed by air
            cp_s_ij = float(self.cp_magnetite_raw(Ts_ij))
            Cs_vol = (1.0 - eps) * self.rho_s * cp_s_ij
            Ts_new[i, j] = Ts_ij - dt * q_to_air / Cs_vol

            # Store average air state inside the cell
            hf_cell[i, j] = 0.5 * (h_air_in_cell + h_air_out_cell)
            Tf_cell[i, j] = float(T_from_h_air(hf_cell[i, j]))

            # Store edge state
            hf_edges[i, j + 1] = h_air_out_cell
            Tf_edges[i, j + 1] = T_air_out_cell

            qsf[i, j] = q_to_air

            # March to next cell
            T_air_in_cell = T_air_out_cell
            h_air_in_cell = h_air_out_cell
```

```
        Ts = Ts_new
        Tf = Tf_cell
        hf = hf_cell

        # ----------------------------------------------------
        # 3) Integral outputs
        # ----------------------------------------------------
        T_s_mean[n + 1] = np.sum(Ts * W_half) / np.sum(W_half)
        T_s_max[n + 1] = np.max(Ts)
        T_s_min[n + 1] = np.min(Ts)

        h_out[n + 1] = self._area_average_outlet(hf_edges[:, -1])
        T_out[n + 1] = T_from_h_air(h_out[n + 1])

        P_rec[n + 1] = m_dot_total * (h_out[n + 1] - h_in)
        E_rec[n + 1] = E_rec[n] + P_rec[n + 1] * dt
```

Listing A.5 – Cell-by-cell air propagation and local solid–fluid energy exchange during discharge (discharging_model.py).

The overall outlet state is therefore obtained from the area-weighted outlet enthalpy, rather than from a direct arithmetic average of the radial outlet temperatures. The recovered thermal power is subsequently evaluated using the total imposed air mass-flow rate and the difference between outlet and inlet specific enthalpy. This implementation maintains energetic consistency between the energy gained by the flowing air and the energy locally removed from the solid phase.

A.3.5 Propagation of the thermal state between cycles

The final numerical development selected for the Appendix concerns repeated charge–discharge operation. Since only one half of the storage domain is simulated during discharge, the residual temperature field must first be reconstructed over the complete domain before it can be used as the initial state of the following charging phase.

The reconstruction function used by the cyclic modules is reported in Listing A.6.

```
    def rebuild_full_map_from_half(self, T_half):
"""
Rebuild the full packed-bed temperature map from the discharged half-domain.

During discharge, the simulated half-domain is:
    physical end -> center plane

The full packed bed for the following charging phase is reconstructed as:
    end -> center -> end

Therefore, the second half is obtained by mirroring the first one.
"""
T_half = np.asarray(T_half, dtype=float)

if T_half.shape[0] != self.Nr:
    raise ValueError(
        f"T_half must have Nr={self.Nr} rows, but got {T_half.shape[0]}"
    )

T_full = np.concatenate([T_half, T_half[:, ::-1]], axis=1)

if T_full.shape != (self.Nr, self.Nz):
    raise ValueError(
        f"Rebuilt full map has shape {T_full.shape}, "
        f"but expected {(self.Nr, self.Nz)}. "
        "This requires an even number of axial cells Nz."
    )

return T_full
```

Listing A.6 – Reconstruction of the complete packed-bed temperature field after discharge (cycles_same_energy_input.py).

At the end of every discharge, this function mirrors the half-domain around the central plane and reconstructs a temperature array having the same dimensions as the complete charging domain. The reconstructed field is assigned to the initial condition of the subsequent charging simulation. Consequently, the model does not return to a uniform temperature between cycles and the spatial thermal history of the packed bed is preserved.

The same principle is used in both cyclic comparison strategies developed in this work. cycles_same_energy_input.py determines the duration of the charging phase from the prescribed cumulative electrical-energy input, whereas cycles_same_Tmean_target.py terminates charging when the prescribed volume-averaged packed-bed temperature is reached, unless the maximum-temperature safety criterion is activated first. Since the remaining numerical structure is largely common to the two implementations, duplicate excerpts are not reported here.

The selected listings therefore illustrate the principal numerical steps through which the reference IH-PBTES formulation was extended in the present work: calculation of a spatial magnetic field, local thermo-electromagnetic heat generation, transient two-dimensional temperature evolution, extraction of stored heat through a flowing air stream and preservation of the residual thermal field across successive operating cycles. The full source files, including the auxiliary routines and the JupyterLab analysis notebook, are made available in the repository described in the following section.

A.4 Complete Code Repository

Only selected portions of the numerical implementation have been reported in Section A.3 in order to keep the Appendix focused on the main modelling developments introduced in this work. The complete source code used for the numerical analyses presented in this thesis is made available through a dedicated GitHub repository.

The repository includes the Python modules described in Section A.2, covering the reference IH-PBTES implementation, the two-dimensional electromagnetic and thermal extensions, the discharge model and the repeated charge–discharge routines. It also contains the JupyterLab notebook used to define the investigated cases, execute the simulations, perform the post-processing of the numerical results and generate the corresponding graphical outputs. The tabulated LangArc input files required by the hysteresis model are provided together with the numerical source files.

To facilitate the interpretation and reproducibility of the computational workflow, the repository also includes a README file describing the organisation of the project and the role of the individual modules, together with a requirements file reporting the principal Python dependencies required to run the numerical framework. The repository therefore provides the complete implementation associated with the modelling methodology and numerical results discussed throughout this thesis.

The complete source code is available at:

https://github.com/lorenzodenitto26/IH-PBTES-2D-model

References

[1] J. Leicher, A. Giese, and C. Wieland, "Electrification or Hydrogen? The Challenge of Decarbonizing Industrial (High-Temperature) Process Heat," *J*, vol. 7, no. 4, pp. 439–456, 2024. DOI: 10.3390/j7040026.

[2] L. Knorr, N. Buchenau, F. Schlosser, D. Divkovic, M. G. Prina, and H. Meschede, "Electrification and flexibility of process heat in energy system modelling: A review," *Renewable and Sustainable Energy Reviews*, vol. 216, 115698, 2025. DOI: 10.1016/j.rser.2025.115698.

[3] Y. Muñoz-Maldonado, E. Correa-Quintana, and A. Ospino-Castro, "Electrification of Industrial Processes as an Alternative to Replace Conventional Thermal Power Sources," *Energies*, vol. 16, 6894, 2023.

[4] S. Madeddu, F. Ueckerdt, M. Pehl, J. Peterseim, M. Lord, K. A. Kumar, C. Krüger and G. Luderer, "The CO_2 reduction potential for the European industry via direct electrification of heat supply (power-to-heat)," *Environmental Research Letters*, vol. 15, no. 12, 124004, 2020. DOI: 10.1088/1748-9326/abbd02.

[5] M. Beaudin, H. Zareipour, A. Schellenberglabe, and W. Rosehart, "Energy storage for mitigating the variability of renewable electricity sources: An updated review," *Energy for Sustainable Development*, vol. 14, no. 4, pp. 302–314, 2010. DOI: 10.1016/j.esd.2010.09.007.

[6] A. Bloess, W.-P. Schill, and A. Zerrahn, "Power-to-heat for renewable energy integration: A review of technologies, modeling approaches, and flexibility potentials," *Applied Energy*, vol. 212, pp. 1611–1626, 2018. DOI: 10.1016/j.apenergy.2017.12.073.

[7] G. Alva, Y. Lin, and G. Fang, "An overview of thermal energy storage systems," *Energy*, vol. 144, pp. 341–378, 2018. DOI: 10.1016/j.energy.2017.12.037.

[8] A. Gil, M. Medrano, I. Martorell, A. Lázaro, P. Dolado, B. Zalba and L. F. Cabeza, "State of the art on high temperature thermal energy storage for power generation. Part 1—Concepts, materials and modellization," *Renewable and Sustainable Energy Reviews*, vol. 14, no. 1, pp. 31–55, 2010. DOI: 10.1016/j.rser.2009.07.035.

[9] U. Pelay, L. Luo, Y. Fan, D. Stitou, and M. Rood, "Thermal energy storage systems for concentrated solar power plants," *Renewable and Sustainable Energy Reviews*, vol. 79, pp. 82–100, 2017. DOI: 10.1016/j.rser.2017.03.139.

[10] S. Pascual, P. Lisbona, and L. M. Romeo, "Thermal Energy Storage in Concentrating Solar Power Plants: A Review of European and North American R&D Projects," *Energies*, vol. 15, no. 22, 8570, 2022. DOI: 10.3390/en15228570.

[11] M. M. Farid, A. M. Khudhair, S. A. K. Razack, and S. Al-Hallaj, "A review on phase change energy storage: materials and applications," *Energy Conversion and Management*, vol. 45, no. 9–10, pp. 1597–1615, 2004. DOI: 10.1016/j.enconman.2003.09.015.

[12] A. Sharma, V. V. Tyagi, C. R. Chen, and D. Buddhi, "Review on thermal energy storage with phase change materials and applications," *Renewable and Sustainable Energy Reviews*, vol. 13, no. 2, pp. 318–345, 2009. DOI: 10.1016/j.rser.2007.10.005.

[13] K. E. N'Tsoukpoe, H. Liu, N. Le Pierrès, and L. Luo, "A review on long-term sorption solar energy storage," *Renewable and Sustainable Energy Reviews*, vol. 13, no. 9, pp. 2385–2396, 2009. DOI: 10.1016/j.rser.2009.05.008.

[14] A. Solé, I. Martorell, and L. F. Cabeza, "State of the art on gas–solid thermochemical energy storage systems and reactors for building applications," *Renewable and Sustainable Energy Reviews*, vol. 47, pp. 386–398, 2015. DOI: 10.1016/j.rser.2015.03.077.

[15] S. Kuravi, J. Trahan, D. Y. Goswami, M. M. Rahman, and E. K. Stefanakos, "Thermal energy storage technologies and systems for concentrating solar power plants," *Progress in Energy and Combustion Science*, vol. 39, no. 4, pp. 285–319, 2013. DOI: 10.1016/j.pecs.2013.02.001.

[16] M. Medrano, A. Gil, I. Martorell, X. Potau and L. F. Cabeza, "State of the art on high-temperature thermal energy storage for power generation. Part 2—Case studies," *Renewable and Sustainable Energy Reviews*, vol. 14, no. 1, pp. 56–72, 2010.

[17] G. Zanganeh, A. Pedretti, S. Zavattoni, M. Barbato and A. Steinfeld, "Packed-bed thermal storage for concentrated solar power – Pilot-scale demonstration and industrial-scale design," *Solar Energy*, vol. 86, no. 10, pp. 3084–3098, 2012. DOI: 10.1016/j.solener.2012.07.019.

[18] I. Calderón-Vásquez, E. Cortés, J. García, V. Segovia, A. Caroca, C. Sarmiento, R. Barraza and J. M. Cardemil, "Review on modeling approaches for packed-bed thermal storage systems," *Renewable and Sustainable Energy Reviews*, vol. 143, 110902, 2021. DOI: 10.1016/j.rser.2021.110902.

[19] T. Esence, A. Bruch, S. Molina, B. Stutz, and J.-F. Fourmigué, "A review on experience feedback and numerical modeling of packed-bed thermal energy storage systems," *Solar Energy*, vol. 153, pp. 628–654, 2017. DOI: 10.1016/j.solener.2017.03.032.

[20] G. Zanganeh, A. Pedretti, A. Haselbacher and A. Steinfeld, "Design of packed bed thermal energy storage systems for high-temperature industrial process heat," *Applied Energy*, vol. 137, pp. 812–822, 2015. DOI: 10.1016/j.apenergy.2014.07.110.

[21] M. Hänchen, S. Brückner, and A. Steinfeld, "High-temperature thermal storage using a packed bed of rocks – Heat transfer analysis and experimental validation," *Applied Thermal Engineering*, vol. 31, no. 10, pp. 1798–1806, 2011. DOI: 10.1016/j.applthermaleng.2010.10.034.

[22] J. A. Almendros-Ibáñez, M. Fernández-Torrijos, M. Díaz-Heras, J. F. Belmonte, and C. Sobrino, "A review of solar thermal energy storage in beds of particles: Packed and fluidized beds," *Solar Energy*, vol. 192, pp. 193–237, 2019. DOI: 10.1016/j.solener.2018.05.047.

[23] Y. Zhang, Y. Guo, J. Zhu, W. Yuan, and F. Zhao, "New Advances in Materials, Applications, and Design Optimization of Thermocline Heat Storage: Comprehensive Review," *Energies*, vol. 17, no. 10, 2403, 2024. DOI: 10.3390/en17102403.

[24] R. Anderson, L. Bates, E. Johnson, and J. F. Morris, "Packed bed thermal energy storage: A simplified experimentally validated model," *Journal of Energy Storage*, vol. 4, pp. 14–23, 2015. DOI: 10.1016/j.est.2015.08.007.

[25] E. Abddaim, S. Sakami, and L. Boukhattem, "Numerical analysis of the impact of various parameters on the axial temperature distribution in a packed bed for thermocline energy storage," *Thermal Science and Engineering Progress*, vol. 68, 104355, 2025. DOI: 10.1016/j.tsep.2025.104355.

[26] M. Cascetta, F. Serra, G. Cau, and P. Puddu, "Comparison between experimental and numerical results of a packed-bed thermal energy storage system in continuous operation," *Energy Procedia*, vol. 148, pp. 234–241, 2018. DOI: 10.1016/j.egypro.2018.08.073.

[27] A. Gautam and R. P. Saini, "A review on technical, applications and economic aspect of packed bed solar thermal energy storage system," *Journal of Energy Storage*, vol. 27, 101046, 2020. DOI: 10.1016/j.est.2019.101046.

[28] S. Hrifech, H. Agalit, A. Jarni, E. M. Mouguina, Y. Grosu, A. Faik, E. G. Bennouna, and A. Mimet, "Characterization of natural rocks as filler materials for medium-temperature packed bed thermal energy storage system," *Journal of Energy Storage*, vol. 32, 101822, 2020. DOI: 10.1016/j.est.2020.101822.

[29] I. Calderón-Vásquez, V. Segovia, J. M. Cardemil, and R. Barraza, "Assessing the use of copper slags as thermal energy storage material for packed-bed systems," *Energy*, vol. 227, 120370, 2021. DOI: 10.1016/j.energy.2021.120370.

[30] B. Cardenas, S. D. Garvey, Z. Baniamerian, and R. Mehdipour, "Magnetite as a Heat Storage Medium in Packed Beds," *Journal of Physics: Conference Series*, vol. 3185, no. 1, 012017, 2026. DOI: 10.1088/1742-6596/3185/1/012017.

[31] Y. Filali Baba, H. Ajdad, A. Al Mers, Y. Grosu and A. Faik, "Multilevel comparison between magnetite and quartzite as thermocline energy storage materials," *Applied Thermal Engineering*, vol. 149, pp. 1142–1153, 2019. DOI: 10.1016/j.applthermaleng.2018.12.002.

[32] S. Belik, O. Khater, and S. Zunft, "Induction Heating of a Fluidized Pebble Bed: Numerical and Experimental Analysis," *Applied Sciences*, vol. 13, no. 4, 2311, 2023. DOI: 10.3390/app13042311.

[33] A. Mariani and G. Malucelli, "Insights into Induction Heating Processes for Polymeric Materials: An Overview of the Mechanisms and Current Applications," *Energies*, vol. 16, no. 11, 4535, 2023. DOI: 10.3390/en16114535.

[34] O. Lucia, P. Maussion, E. J. Dede, and J. M. Burdío, "Induction heating technology and its applications: Past developments, current technology, and future challenges," *IEEE Transactions on Industrial Electronics*, vol. 61, no. 5, pp. 2509–2520, 2014, doi: 10.1109/TIE.2013.2281162.

[35] V. Rudnev, D. Loveless, and R. L. Cook, *Handbook of Induction Heating*, 2nd ed. Boca Raton, FL: CRC Press, Taylor & Francis Group, 2017.

[36] S. Lupi, *Fundamentals of Electroheat: Electrical Technologies for Process Heating*. Springer International Publishing, 2017, doi: 10.1007/978-3-319-46015-4.

[37] P. Duquenne, A. Deltour, and G. Lacoste, "Application of inductive heating to granular media: Modelling of electrical phenomena," *The Canadian Journal of Chemical Engineering*, vol. 72, no. 6, pp. 975–981, 1994, doi: 10.1002/cjce.5450720606.

[38] X. Zhu, M. Xing, J. Ye, X. Liu, and Z. Ren, "Design and optimization of a novel solenoid with high magnetic uniformity," *Scientific Reports*, vol. 14, 24650, 2024. DOI: 10.1038/s41598-024-76501-y.

[39] J. Kimme, A. Fröhlich, M. Kroll, and V. Kräusel, "Novel Process Approach for Additive Manufacturing Using Inductive Wire Melting by Forced Droplet Detachment," *BHM Berg- und Hüttenmännische Monatshefte*, vol. 168, pp. 226–232, 2023. DOI: 10.1007/s00501-023-01344-5.

[40] M. Niu, T. Akiyama, R. Takahashi, and J.-i. Yagi, "Experimental and Parametric Analyses of Heat Transfer within Two-layered Packed Beds of Iron and Graphite in a High-frequency Induction Furnace," *Tetsu-to-Hagane*, vol. 82, no. 2, pp. 105–110, 1996. DOI: 10.2355/tetsutohagane1955.82.2_105.

[41] J. P. P. Noble, S. J. Bending, A. R. Muxworthy, and A. K. Hill, "A simplified model for minor and major loop magnetic hysteresis and its application for inference of temperature in induction heated particle beds," *Journal of Physics D: Applied Physics*, vol. 56, no. 49, 2023, doi: 10.1088/1361-6463/acf13f.

[42] A. Bordet, W. Leitner, and B. Chaudret, "Magnetically Induced Catalysis: Definition, Advances, and Potential," *Angewandte Chemie International Edition*, vol. 64, no. 24, e202424151, 2025. DOI: 10.1002/anie.202424151.

[43] M. Patil, R. K. Choubey, and P. K. Jain, "Influence of coil shapes on temperature distribution in induction heating process," *Materials Today: Proceedings*, vol. 72, pp. 3029–3035, 2023. DOI: 10.1016/j.matpr.2022.08.376.

[44] M. Fisk, M. Ristinmaa, A. Hultkrantz, and L.-E. Lindgren, "Coupled electromagnetic-thermal solution strategy for induction heating of ferromagnetic materials," *Applied Mathematical Modelling*, vol. 111, pp. 818–835, 2022. DOI: 10.1016/j.apm.2022.07.009.

[45] Y. Yu, L. Tauxe, and B. M. Moskowitz, "Temperature dependence of magnetic hysteresis," *Geochemistry, Geophysics, Geosystems*, vol. 5, no. 6, Q06H11, 2004. DOI: 10.1029/2003GC000685.

[46] D. J. Dunlop, "High-temperature susceptibility of magnetite: a new pseudo-single-domain effect," *Geophysical Journal International*, vol. 199, pp. 707–716, 2014, doi: 10.1093/gji/ggu247.

[47] D. J. Dunlop, "Magnetic hysteresis of magnetite at high temperature: grain size variation," *Geophysical Journal International*, vol. 226, pp. 816–827, 2021, doi: 10.1093/gji/ggab138.

[48] Q. Liu, A. P. Roberts, J. C. Larrasoaña, S. K. Banerjee, Y. Guyodo, L. Tauxe, and F. Oldfield, "Environmental magnetism: Principles and applications," *Reviews of Geophysics*, vol. 50, no. 4, RG4002, 2012. DOI: 10.1029/2012RG000393.

[49] H. Elnaggar, S. Graas, S. Lafuerza, B. Detlefs, W. Tabiś, M. A. Gala, A. Ismail, A. van der Eerden, M. Sikora, J. M. Honig, P. Glatzel, and F. de Groot, "Temperature-Driven Self-Doping in Magnetite," *Physical Review Letters*, vol. 127, no. 18, 186402, 2021. DOI: 10.1103/PhysRevLett.127.186402.

[50] N. M. Botrous El Badramany, E. F. Mina, H. D. Merchant, S. Arafa, and R. P. Poplawsky, "Electrical Resistivity of Magnetite and Nickel Ferrous Ferrite Above 300°K," *Journal of the American Ceramic Society*, vol. 62, no. 3–4, pp. 113–116, 1979.

[51] P. Vishnuram, G. Ramachandiran, T. S. Babu, and B. Nastasi, "Induction Heating in Domestic Cooking and Industrial Melting Applications: A Systematic Review on Modelling, Converter Topologies and Control Schemes," *Energies*, vol. 14, no. 20, 6634, 2021. DOI: 10.3390/en14206634.

[52] A. Famiglietti and R. Abbas, "A novel induction-heated packed bed integrating power-to-heat conversion and thermal energy storage for industrial process heat: a technical viability analysis," preprint, 2026. DOI: 10.2139/ssrn.6259851.

[53] Y. Grosu, A. Faik, I. Ortega-Fernández, and B. D'Aguanno, "Natural Magnetite for thermal energy storage: Excellent thermophysical properties, reversible latent heat transition and controlled thermal conductivity," Solar Energy Materials & Solar Cells, vol. 161, pp. 170–176, 2017, doi: 10.1016/j.solmat.2016.12.006.

[54] I. Calderón-Vásquez and J. M. Cardemil, "A comparison of packed-bed flow topologies for high-temperature thermal energy storage under constrained conditions," Applied Thermal Engineering, vol. 238, 121934, 2024, doi: 10.1016/j.applthermaleng.2023.121934.

[55] I. H. Bell, J. Wronski, S. Quoilin, and V. Lemort, "Pure and Pseudo-pure Fluid Thermophysical Property Evaluation and the Open-Source Thermophysical Property Library CoolProp," *Industrial & Engineering Chemistry Research*, vol. 53, no. 6, pp. 2498–2508, 2014, doi: 10.1021/ie4033999.

[56] D. J. Gunn, "Transfer of heat or mass to particles in fixed and fluidised beds," *International Journal of Heat and Mass Transfer*, vol. 21, no. 4, pp. 467–476, 1978, doi: 10.1016/0017-9310(78)90080-7.

[57] B. Drobenko, O. Hachkevych, T. Kournyts'kyi, "A mathematical simulation of high temperatur induction heating of electroconductive solids," *International Journal of Heat and Mass Transfer*, vol. 50, pp. 616–624, 2007. DOI: 10.1016/j.ijheatmasstransfer.2006.07.013.

[58] H. Kawaguchi, M. Enokizono, T. Todaka, "Thermal and magnetic field analysis of induction heating problems," *Journal of Materials Processing Technology*, vol. 161, pp. 193–198, 2005. DOI: 10.1016/j.jmatprotec.2004.07.075.

[59] J. Wang, J. Xu, L. Zhang, J. Ye, S. Wang, Investigation on the inductive heating characteristics of metal particles by the magneto-thermal coupling method," *Powder Technology*, vol. 468, 121660, 2026. DOI: 10.1016/j.powtec.2025.121660.

[60] D. Kleschew, U. Tuttlies, U. Nieken, "Experimental Analysis of Inductive Heating of Catalytic Beds," *Chemie Ingenieur Technik*, vol. 96, no. 6, pp. 769–773, 2024. DOI: 10.1002/cite.202300168.

[61] S. C. Nian, S. W. Tsai, M. S. Huang, R. C. Huang, and C. H. Chen, "Key parameters and optimal design of a single-layered induction coil for external rapid mold surface heating," *International Communications in Heat and Mass Transfer*, vol. 57, pp. 109–117, 2014. DOI: 10.1016/j.icheatmasstransfer.2014.07.019.

[62] L. Wei, J. Mies, I. Roghair, J. Boon, and M. van Sint Annaland, "Optimization of efficiency and temperature uniformity in induction heating with 3D workpieces," *Chemical Engineering Journal*, vol. 540, 177652, 2026. DOI: 10.1016/j.cej.2026.177652.

[63] J. Marti, L. Geissbühler, V. Becattini, A. Haselbacher, and A. Steinfeld, "Constrained multi-objective optimization of thermocline packed-bed thermal-energy storage," *Applied Energy*, vol. 216, pp. 694–708, 2018. DOI: 10.1016/j.apenergy.2017.12.072.

[64] B. Krüger, F. Dammel, and P. Stephan, "Investigating the aspect ratio's influence on the exergetic performance and thermocline dynamics of a large water-based thermal energy storage system," *Journal of Energy Storage*, vol. 91, 112058, 2024. DOI: 10.1016/j.est.2024.112058.

[65] D. Le Roux, R. Olivès, and P. Neveu, "Geometry optimisation of an industrial thermocline Thermal Energy Storage combining exergy, Life Cycle Assessment and Life Cycle Cost Analysis," *Journal of Energy Storage*, vol. 55, 105776, 2022. DOI: 10.1016/j.est.2022.105776.

[66] I. Ortega-Fernández, I. Uriz, A. Ortuondo, A. B. Hernández, A. Faik, I. Loroño, and J. Rodríguez-Aseguinolaza, "Operation strategies guideline for packed bed thermal energy storage systems," *International Journal of Energy Research*, vol. 43, pp. 6211–6221, 2019. DOI: 10.1002/er.4291.

[67] J. D. McTigue, C. N. Markides, and A. J. White, "Performance response of packed-bed thermal storage to cycle duration perturbations," *Journal of Energy Storage*, vol. 19, pp. 379–392, 2018. DOI: 10.1016/j.est.2018.08.016.

[68] M. Díaz-Heras, J. F. Belmonte, and J. A. Almendros-Ibáñez, "Effective thermal conductivities in packed beds: Review of correlations and its influence on system performance," *Applied Thermal Engineering*, vol. 171, 115048, 2020.
DOI:10.1016/j.applthermaleng.2020.115048